

**THE EFFECTS OF MAGMATIC EVOLUTION, CRYSTALLINITY, AND
MICROTEXTURE ON THE VISIBLE/NEAR-INFRARED AND
THERMAL-INFRARED SPECTRA OF VOLCANIC ROCKS**

by

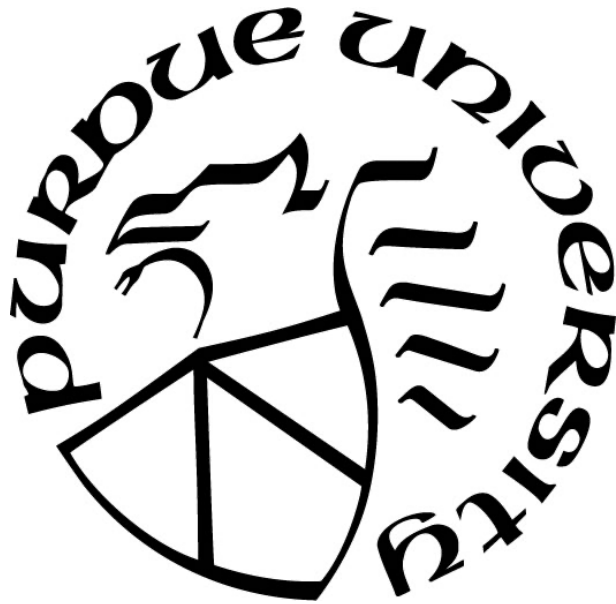
Noel Alexander Scudder

A Thesis

Submitted to the Faculty of Purdue University

In Partial Fulfillment of the Requirements for the degree of

Master of Science



Department of Earth, Atmospheric, and Planetary Sciences

West Lafayette, Indiana

August 2023

THE PURDUE UNIVERSITY GRADUATE SCHOOL
STATEMENT OF COMMITTEE APPROVAL

Dr. Andrew M. Freed, Chair

Department of Earth, Atmospheric, and Planetary Sciences

Dr. Briony H. N. Horgan

Department of Earth, Atmospheric, and Planetary Sciences

Dr. Cliff T. Johnston

Department of Agronomy
Department of Earth, Atmospheric, and Planetary Sciences

Dr. Darrell G. Schulze

Department of Agronomy

Approved by:

Dr. Daniel Cziczo

For Gavin and Vega

ACKNOWLEDGMENTS

This work was supported by NASA Headquarters under the NASA Earth and Space Science Fellowship Program - Grant 80NSSC18K1261 and SSW Grant NNX16AG38G. Fieldwork was supported in part by the Indiana Space Grant. Thanks to Marie Henderson, Sheridan Ackiss, Rebecca Smith, and all others who assisted with fieldwork. Thanks to Darrell Schulze and Cliff Johnston for XRD machine access and geochemistry advice, and Phil Christensen for TIR spectrometer access. Thanks to Anne Peslier for her invaluable help with microprobe measurements, and Chris Haberle for useful early discussions. Thanks especially to my endlessly helpful and patient advisor, Dr. Briony Horgan.

TABLE OF CONTENTS

LIST OF TABLES	7
LIST OF FIGURES	8
ABSTRACT	11
CHAPTER 1. INTRODUCTION.....	12
CHAPTER 2. THE EFFECTS OF MAGMATIC EVOLUTION, CRYSTALLINITY, AND MICROTEXTURE ON THE VISIBLE/NEAR-INFRARED AND THERMAL-INFRARED SPECTRA OF VOLCANIC ROCKS	14
2.1 Background	14
2.1.1 Magmatic Evolution and Bulk Mineralogy	14
2.1.2 Crystallinity.....	19
2.2 Field Site	21
2.2.1 Applicability to Planetary Spectroscopy.....	23
2.2.2 Sample Suite	24
2.3 Methods.....	25
2.3.1 Thermal-Infrared Emission Spectroscopy	25
2.3.2 Visible/Near-Infrared Spectroscopy	29
2.3.3 Quantitative X-Ray Diffraction	29
2.3.4 Chemistry and Textural Analysis.....	31
2.4 Baseline Mineralogy, Chemistry, and Texture	32
2.4.1 XRF Bulk Chemistry	32
2.4.2 XRD Mineralogy and Crystal Chemistry	32
2.4.3 EMPA Chemistry and Texture.....	34
2.5 Petrologic Properties Derived from TIR Spectral Models.....	41
2.5.1 TIR Spectral Properties.....	41
2.5.2 TIR Mineral Abundances.....	41
2.5.3 TIR Mineral Compositions	44
2.5.4 TIR Bulk Chemistry.....	48
2.6 VNIR Spectral Properties and Analysis.....	51
2.6.1 Mineralogy Interpreted from VNIR Spectra.....	52

2.6.2	Comparison of VNIR with Quantitative Mineralogy	56
2.6.3	Comparison of VNIR with Mineral Chemistry	63
2.7	Discussion	64
2.7.1	Interpretability of Petrologic Information from TIR Spectra	64
2.7.2	Interpretability of Petrologic Information from VNIR Spectra	68
2.7.3	Effects of Rock Microtexture on VNIR Spectra	70
2.7.4	Examples of the Advantages of Combined VNIR and TIR Spectroscopy	73
2.7.5	Implications for Planetary Spectroscopy	74
2.8	Conclusions	76
APPENDIX		80
REFERENCES		81
PUBLICATION		99

LIST OF TABLES

Table 2.1. Mapped Units used in this study.	23
Tables S1-S12. Accessible through the publicly available Mendeley Data repository: https://doi.org/10.17632/2vkdbfjptn (Scudder et al., 2020).	80

LIST OF FIGURES

Figure 2.1. Field site overview. (a) Annotated satellite imagery (Quickbird, Google Earth). (b) Geologic map of the Three Sisters field site adapted from Hildreth et al. (2012), labeled with unit names most relevant to this study. See Supplemental Table S1 for sample locations. (c) East-facing view of North Sister and peripheral volcanic constructs. (d) Example flow outcrop of unit mns, located at point d in (a). (e) Example rock samples used in this study.22

Figure 2.2. TIR and VNIR sample spectra. (a) Example thermal infrared emission spectrum and deconvolution model of sample dbh-1 (a dark, glassy dacite) with derived wt.% abundances listed by mineral group. Residual is shown in red in the same scale, with deviations from a perfect fit highlighted using a zero reference line. (b) Emission spectra (gray) and modeled fits (black) for a variety of geologic units in this study. In general, the models are very good matches to the measured spectra (rms <0.003). (c) All visible/near infrared sample spectra, grouped into Spectral Groups 1-8. Groups 1-6 are unaltered, Group 7 is oxidized, and Group 8 is altered. Colored bold spectra are representative of their respective group. Laboratory spectra shown in black for reference: Fe-plagioclase: Keck/NASA ReLab spectrum LR-CMP-183. Glass: University of Winnipeg PSF spectrum TEK004 (Horgan et al., 2014). Olivine: USGS spectrum KI3054 Fo66 (Kokaly et al., 2017). Augite, pigeonite, and enstatite: ReLab DL-CMP-073, -011, and -065 (Klima et al., 2007).27

Figure 2.3. TIR deconvolved wt.% mineral abundances by group compared to abundances calculated from XRD refinements. Inset shows an enlargement of the lower-left corner of the larger plot. Amorphous abundances are shown in Figure 2.8a.33

Figure 2.4. Effects of microtexture on spectral properties. (a-c) Electron backscatter images of basaltic andesite samples with similar crystalline mineralogies (a) mms-2, (b) mms-Cb, and (c) mns-Vv, exhibiting a range of microtextures. Ol=Olivine, Pyx=Pyroxene, Plag=Plagioclase, Ox=Oxide, Gl=Glass. Pyroxene often occurs as discrete microphenocrysts like in (a), but in some samples is limited to intimately mixed microphases as in (b) and (c). Similarly, oxide minerals typically occur as discrete microphenocrysts or as blebs in the interstitial glass, but are sub-micron scale in (b) and (c). (d) Thermal emission spectra of the samples. mms-Cb has more muted, rounder features due to higher glass and lower feldspar content. (e) Visible/near-infrared spectra showing suppressed 1- μ m features in mms-Cb and mns-Vv alongside the appearance of a small 0.6 μ m absorption (inset) likely due to oxides.35

Figure 2.5. Comparison of EMPA measured and XRD/TIR derived feldspar compositions. (a) Solid solution composition of feldspar phases in all 10 rocks measured by EMPA. TIR library endmembers are included for comparison with (b). (b) Composition of feldspar phases for all 36 rocks with TIR and XRD derivations. The XRD-derived compositions (red triangles) only consider K-free albite-anorthite solid solution and plot along the bottom axis. The weighted average of all TIR-derived feldspar in each rock (orange diamonds) is broken out into average K-feldspar composition (teal diamonds) and average plagioclase composition (yellow diamonds) for each rock. (c) Mol% anorthite (An#) derived from TIR and XRD methods. Symbols indicate rock type in unaltered rocks, or alteration and oxidation in altered or oxidized rocks.37

Figure 2.6. Pyroxene ternary diagram showing EMPA-measured (circles) and TIR-derived (diamonds) pyroxenes for EMPA-measured samples. TIR results are displayed as the abundance-weighted average of all modeled pyroxene chemistries for each rock. TIR results are acceptable if they plot within the shaded area describing the compositional mixing range allowable by EMPA.

.....39

Figure 2.7. Fe-Ti oxide ternary showing EMPA-derived chemistries (circles) compared to TIR endmembers (squares) and TIR modeled average oxide mineral chemistry (diamonds).....40

Figure 2.8. TIR model results for amorphous material. (a) TIR-derived amorphous abundance plotted against XRD-derived amorphous abundance. Symbols indicate rock type in unaltered rocks, or alteration and oxidation in altered or oxidized rocks. (b) Trend in the error in wt.% SiO₂ of TIR-derived amorphous material, calculated as the difference between the TIR-derived wt.% SiO₂ of the amorphous component and the EMPA-estimated wt.% SiO₂ of glass for the same sample, as compared to total XRD wt.% amorphous.....44

Figure 2.9. Mol% forsterite (Fo#) of olivine derived from TIR models and XRD results, showing overestimation of Fe-rich olivine in some TIR models, most likely due to transparency effects. Point size corresponds to XRD-derived olivine abundance. Rocks where olivine was not detected by XRD but was falsely modeled by TIR plot along the y-axis.....46

Figure 2.10. Effects of oxidation on spectral properties. (a) XRD-derived mineralogy for samples awc-2 and awc-3. Their mineralogy is nearly identical, except for the identity of their oxide minerals. (b) TIR spectra of rocks awc-2 and awc-3. awc-2 is ilmenite-bearing, whereas awc-3 contains fine-grained hematite. (c) VNIR spectra of rocks awc-2 and awc-3. The spectrum of awc-2 is dominated by pyroxene, whereas awc-3 is spectrally dominated by hematite. TIR ilmenite and hematite: ASU SpecLib (Christensen et al., 2000). VNIR Ilmenite: ILM102-lt45um-071201b, University of Winnipeg PSF. Hematite, pigeonite: USGS GDS76, HS199.1B (Kokaly et al., 2017). The lab hematite includes a significant spectrally neutral component to achieve the same spectral contrast.47

Figure 2.11. Accuracy of TIR-derived bulk petrology. (a) TIR-derived major wt.% oxides compared to XRF chemistry. (b) Total alkali vs. silica diagram (LeBas et al., 1986) of all TIR models (symbol positions) compared to expected unit petrology (symbol colors) from Hildreth et al. (2012). Symbol colors that match their background are accurate models. Units intermediate between fields have mixed colors. Symbol shapes correspond to unaltered (circles), oxidized (triangles), or hydrothermally altered (squares) samples. Models notably underestimate wt.% SiO₂ in the four altered samples. (c) The subset of TIR models with corresponding XRF measurements compared to those XRF measurements. TIR models results are colored as in (b), and XRF measurements are in black.....49

Figure 2.12. VNIR spectral parameters. (a) 1 μ m band center vs. 1 μ m asymmetry for all spectra from groups defined in Figure 2c, excluding two Group 6 spectra with no clear 1 μ m absorption. Plotted classification fields are characteristic parameter spaces for materials or 2-component mixtures modified from Horgan et al. (2014). (b) 1 μ m vs. 2 μ m band centers for all spectra that have clear 2 μ m bands of over 2% depth. Orange (N) and yellow fields are for natural samples from Horgan et al. (2014), and blue fields (S) are for synthetic pyroxenes from Klima et al. (2011a). Adding olivine in mixture will draw points to the right on this plot, while adding glass will draw

points towards the glass field. Group 7 hematite band centers were skewed to longer wavelengths by the continuum removal process.53

Figure 2.13. Relationship between pyroxene content and 1 and 2 μm absorptions. (a) 1 μm band depth and (b) 2 μm band depth versus XRD pyroxene abundance for Groups 1-5. Little useful correlation occurs between band depth and pyroxene abundance. Even less correlation is observed if band depth or band area are plotted against XRD pyroxene + olivine abundance. (c) 1 μm band center versus XRD-derived CPX/(Total Pyx) ratio for unaltered spectra (Groups 1-6). Band centers between 0.95-0.98 μm can be indicative of a wide range of OPX-CPX mixtures, from majority OPX to 100% CPX. Mixing with olivine and/or glass further complicate interpretation by drawing points to the right.57

Figure 2.14. Spectral similarity between a basaltic andesite and dacite with highly dissimilar bulk and mafic mineralogy. VNIR spectra of a basaltic andesite (mms-2) and dacite (dbh-1) compared with laboratory mineral spectra and bulk mineralogy. Despite distinct mineralogy, the main observable difference is 1 μm band center corresponding to CPX in mms-2 and OPX in dbh-1. mms-2 also has a weak 2 μm band not shown. OPX, CPX, Olivine: USGS NMNH128288, NMNH120049, NMNH137044 (Kokaly et al., 2017). Fe-Glass, Fe-Plagioclase: See Figure 2.2.58

Figure 2.15. Trends of XRD abundances of pyroxene (blue diamonds), olivine (red squares), amorphous (orange triangles), and plagioclase (green circles) compared to 1 μm band asymmetry and band center.61

Figures S1-S11. Accessible through the publicly available Mendeley Data repository: <https://doi.org/10.17632/2vkdbfjptn> (Scudder et al., 2020).80

ABSTRACT

The natural chemical and physical variations that occur within volcanic rocks (petrology) provide critical insights into mantle and crust conditions on terrestrial bodies. Visible/near-infrared (VNIR; 0.3-2.5 μm) and thermal infrared (TIR; 5-50 μm) spectroscopy are the main tools available to remotely characterize these materials from satellites in orbit. However, the accuracy of petrologic information that can be gained from spectra when rocks exhibit complex variations in mineralogy, crystallinity, microtexture, and oxidation state occurring together in natural settings is not well constrained. Here, we compare the spectra of a suite of volcanic planetary analog rocks from the Three Sisters, OR to their mineralogy, chemistry, and microtexture from X-ray diffraction, X-ray fluorescence, and electron microprobe analysis. Our results indicate that TIR spectroscopy is an effective petrologic tool in such rocks for modeling bulk mineralogy, crystallinity, and mineral chemistry. Given a library with appropriate glass endmembers, TIR modeling can derive glass abundance with similar accuracy as other major mineral groups and provide first-order estimates of glass wt.% SiO_2 in glass-rich samples, but cannot effectively detect variations in microtexture and minor oxide minerals. In contrast, VNIR spectra often yield non-unique mineralogic interpretations due to overlapping absorption bands from olivine, glass, and Fe-bearing plagioclase. In addition, we find that sub-micron oxides hosted in transparent matrix material that are common in fine-grained extrusive rocks can lower albedo and partially to fully suppress mafic absorption bands, leading to very different VNIR spectra in rocks with the same mineralogy and chemistry. Mineralogical interpretations from VNIR spectra should not be treated as rigorous petrologic indicators, but can supplement TIR-based petrology by providing unique constraints on oxide minerals, microtexture, and alteration processes.

CHAPTER 1. INTRODUCTION

Volcanism is a common process on the terrestrial planets, moons, and small bodies across the Solar System. In addition to providing information on interior heating and thermal evolution, volcanic deposits derived from internal magma sources carry clues about local to planet-scale petrogenetic processes and physical and chemical conditions. Because of the highly localized nature of landed missions, much of our information on global, regional, and local surface properties on Mars, the Moon, and Venus comes from orbital investigations. Visible/near-infrared (VNIR; 0.3-2.5 μm) and thermal-infrared (TIR; 5-50 μm) spectra are among the most common compositional datasets available for other planets (e.g., Bandfield et al., 2000; Christensen et al., 2003; Bibring et al., 2005; Rogers and Christensen, 2007; Murchie et al., 2007). TIR emission spectroscopy has been shown to be an effective tool for constraining the petrology of crystalline igneous rocks (Feely and Christensen, 1999; Hamilton and Christensen, 2000; Wyatt et al., 2001), and VNIR reflectance spectroscopy can identify a variety of igneous and secondary minerals (e.g., Adams, 1968). However, the ability of either technique to accurately determine the chemistry and petrology of extrusive volcanic deposits in particular is less well understood, as the spectral properties of these deposits often vary significantly due to crystallinity, oxidation, syn-eruptive aqueous alteration, and texture. Spectral evidence for these properties can provide major insights into eruption mechanics and emplacement conditions; however, these same processes may result in systematic errors or non-uniqueness that must be identified in order to better interpret orbital data.

The goal of this study is to better characterize how naturally occurring variations in magmatic evolution, crystallinity, oxidation state, and microtexture combine to affect VNIR and TIR spectra, and to assess how well we can detect and interpret each of these characteristics in terrestrial and planetary volcanism. Previous analog studies have often provided in-depth analyses of individual rocks, lava flows, or single lithologic units (e.g., Byrnes et al., 2004). Studies addressing spectral variability in complex, compositionally broad volcanic systems (e.g., Haberle, 2018) are less common. Given that orbital investigations must occur at the scale of these large volcanic systems, a rigorous understanding of their variation in Earth analog sites is key for understanding igneous variability from orbit on other planets.

In this study, we analyzed a diverse suite of rocks from a Mars-analog field site (Rutledge et al., 2018) at the Three Sisters Volcanic Complex, OR, which includes volcanic units covering a wide range of chemistry, microtexture, crystallinity, and oxidation states (Hildreth et al., 2012). This sample suite is distinctive among spectroscopic studies in that all samples are derived from the same volcanic province, such that physical, chemical, and spectral changes are linked to processes occurring within the same local volcanic system. This study also uniquely leverages combined VNIR and TIR spectral analysis supported by detailed sample characterization: mineralogy via X-ray diffraction (XRD), crystal and glass chemistry via electron microprobe analysis (EMPA), bulk chemistry from X-ray fluorescence (XRF), and microtexture from EMPA. This combination of baseline methods allows greater insight into the interpretability of VNIR and TIR spectra, both separately and together, of igneous material on rocky planetary bodies.

CHAPTER 2. THE EFFECTS OF MAGMATIC EVOLUTION, CRYSTALLINITY, AND MICROTEXTURE ON THE VISIBLE/NEAR-INFRARED AND THERMAL-INFRARED SPECTRA OF VOLCANIC ROCKS

This chapter is published in the peer-reviewed journal *Icarus*, cited as:

Scudder, N. A., Horgan, B. H. N., Rampe, E. B., Smith, R. J., & Rutledge, A. M. (2021). The effects of magmatic evolution, crystallinity, and microtexture on the visible/near-infrared and thermal-infrared spectra of volcanic rocks. *Icarus*, 359, 114344.

(<https://doi.org/10.1016/j.icarus.2021.114344>)

2.1 Background

A wealth of previous studies have investigated the separate spectral expressions of igneous minerals, volcanic glass, and oxidation state, and identified these characteristics on planetary bodies both by landed missions and remote spectroscopy. In this section, we summarize these spectral effects in volcanic material and the variability in each that has been observed on Mars, the Moon, and Venus.

2.1.1 Magmatic Evolution and Bulk Mineralogy

The natural chemical and physical variations that occur within volcanic rocks (petrology) provide critical insights into mantle and crust conditions on terrestrial bodies. Magmas derived from partial melting of rock undergo a variety of processes that cause the bulk chemistry of the final emplaced product to differ from the primary melt chemistry. Variations in the degree of partial melting, incorporation of crustal rock during magma ascent, magma mixing, and fractional crystallization are all processes that give rise to different igneous rock types and contribute to measurable differences in bulk chemistry and mineralogy. In a given magma system, fractional crystallization is responsible for formation of minerals from a melt, which typically evolves the composition of the melt towards more silicic compositions.

Effects of Bulk Mineralogy on TIR and VNIR Spectra

TIR spectroscopy can be used to interpret igneous lithologies due to its sensitivity to major rock-forming minerals (Farmer, 1974). In particular, silica content can be detected based on the

position of the Si-O fundamental absorption complex near 1000 cm^{-1} , which shifts to higher wavenumber with increasing degree of silica polymerization in silica-rich minerals and bulk compositions (e.g., Michalski et al., 2003; Walter and Salisbury, 1989). These mineral assemblages and their quantitative abundances can be derived from modeling of TIR spectra under the assumption of linear mixing (Thomson and Salisbury, 1993). This assumption holds for rocks and particulate material with grain sizes $>60 \mu\text{m}$ and can be leveraged to determine the bulk mineralogy of a sample by deconvolving the spectrum with spectral libraries of pure mineral phases (Ramsey and Christensen, 1998).

TIR spectral unmixing of unaltered, glass-poor igneous rocks is largely accurate. Linear deconvolution of major mineral abundances in igneous and metamorphic rock spectra agree with optical analyses to within 5-15 volume percent (vol.%) with a typical detection limit of 5-10 vol.% (Feely and Christensen, 1999; Hamilton and Christensen, 2000; Wyatt et al., 2001). Additionally, weight percent (wt.%) bulk oxide chemistry calculated from these deconvolutions can be estimated to within 10% absolute error, and plots in or near the correct rock classifications on a total alkali ($\text{Na}_2\text{O}+\text{K}_2\text{O}$) versus silica diagram (Hamilton and Christensen, 2000; Le Bas et al., 1986; Wyatt et al., 2001). These studies also found moderate success in estimating major mineral solid solution chemistry, including average plagioclase and pyroxene chemistry to within $\sim 10\text{-}15 \text{ An}\#$ or $\text{Mg}\#$ of known values (Hamilton and Christensen, 2000), but were less successful in modeling pyroxene compositions (Wyatt et al., 2001), and noted either consistent under- or overestimation of olivine abundance. Alteration may significantly diminish the accuracy of TIR models. Rampe et al. (2013) calculated bulk composition from TIR unmixing models of weathered basalts and found that alkalis, SiO_2 , and FeO were not well-modeled for weathered surfaces. The accuracy in estimating these characteristics for rocks more diverse in glass content and oxidation state has not yet been tested systematically.

VNIR spectra of igneous minerals are typically dominated by absorptions due to iron or other transition metals, but absorptions due to Si-O bonding do not occur in this wavelength range. VNIR spectroscopy is therefore not directly sensitive to nominally Fe-free minerals that are key indicators of silicic volcanism, including quartz and alkali/plagioclase feldspar. Minor iron substitution into the crystal structure of plagioclase can induce a broad absorption centered near $1.25 \mu\text{m}$ that shifts with plagioclase solid solution composition and deepens with increasing iron content, but is easily obscured by other mafic minerals (Adams and Goullaud, 1978; Bell and Mao,

1973; Cheek et al., 2013; Cheek and Pieters, 2014; Crown and Pieters, 1987). Pyroxene typically displays two broad, symmetric absorptions centered at ~ 1 and $2\ \mu\text{m}$, which shift to longer wavelengths with higher iron or calcium content (Burns, 1993; Cloutis and Gaffey, 1991b; Klima et al., 2007; Klima et al., 2011a). Rapidly cooled pyroxene can also exhibit a shoulder near $1.2\ \mu\text{m}$ due to substituted iron in the M1 crystallographic site (Klima et al., 2007; 2008). Olivine has three absorptions near 0.85 , 1.05 , and $1.15\ \mu\text{m}$ that overlap to form a broad, asymmetric complex between 1 - $1.4\ \mu\text{m}$ that varies in shape and position with iron content and particle size (Burns, 1993; Dyar et al., 2009; Isaacson et al., 2014; King and Ridley, 1987; Sunshine and Pieters, 1998).

The spectral expression of intimately mixed material is highly nonlinear in the VNIR region due to multiple scattering of reflected photons (Hapke, 1981), so extrapolating quantitative mineralogy from VNIR spectra is challenging. Numerous experimental and modeling studies have shown that two-component mixing spectra of igneous minerals exhibit interpretable absorption band mixing trends (e.g., Cheek et al., 2013; Cheek and Pieters, 2014; Crown and Pieters, 1987; Horgan et al., 2014; Serventi et al., 2013; Singer, 1981), although spectral interpretability decreases with increasing number of absorbing minerals. VNIR linear unmixing models utilizing optical constants, absorption band deconvolution, and other approaches have been applied to planetary surface spectra (e.g., Kanner et al., 2007; Liu et al., 2016; Riu et al., 2019), but are limited in their accuracy both by the inability to uniquely model common spectrally bland phases (e.g., plagioclase, quartz) as well as inherent assumptions in the underlying radiative transfer models (Hapke, 1981; Shkuratov et al., 1999). In general, analysis of spectral ambiguity in complex multicomponent (e.g., olivine, pyroxene, Fe-bearing glass, Fe-bearing plagioclase, oxides) natural mixtures and its effect on confident mineralogical interpretations is relatively understudied.

The challenges of quantitative mineral interpretation from VNIR spectra combined with their inability to detect most felsic minerals means that VNIR is more commonly used for qualitative mineral identification. However, the presence of certain mineral signatures has been used to place constraints on bulk mineralogy potentially indicative of petrology. For example, spectrally dominant olivine may suggest mafic or ultramafic rocks (Mustard et al., 2005), whereas spectrally dominant Fe-bearing plagioclase implies low abundances of mafic minerals, potentially consistent with more silica-rich compositions (Carter and Poulet, 2013; Rogers and Nekvasil, 2015; Wray et al., 2013).

Magmatic Evolution on other Planetary Bodies

Mars has long been recognized as a predominantly basaltic planet, and large shield volcanoes and extensive flood basalts are clear geomorphic evidence that effusive volcanism has been important throughout much of its geologic history (e.g., Carr, 1973; Hauber et al., 2005; Neukum et al., 2004; Robbins et al., 2011). However, geochemistry and petrology from orbital missions has suggested that other igneous lithologies exist on the martian surface (e.g., Carter and Poulet, 2013; Christensen et al., 2005; Mustard et al., 2005; Wray et al., 2013) and diverse elemental chemistries have been verified via in-situ examination of igneous rocks by rovers (Sautter et al., 2016), including the detection of alkaline and felsic igneous rocks implying significant magmatic evolution (Cousin et al., 2017; Edwards et al., 2017; Filiberto et al., 2014; Greeley et al., 2005; Mangold et al., 2016; McSween et al., 1999; 2006; Udry et al., 2018). Bandfield et al. (2000) used orbital TIR spectra from the Thermal Emission Spectrometer (TES) to categorize the low albedo regions of Mars into two spectral types: a basalt (Surface Type 1) and a second type best matched by glassy basaltic andesite/andesite (Surface Type 2) now thought to be due to weathering rather than extensive volumes of evolved volcanic material (Horgan and Bell, 2012; Koeppen and Hamilton, 2005; Michalski et al., 2005; Rampe et al., 2012; Salvatore et al., 2014; Wyatt and McSween, 2002). However, global-scale igneous diversity has been clearly identified using orbital VNIR spectra from the Compact Reconnaissance Imaging Spectrometer for Mars (CRISM; e.g., Mustard et al., 2005) and the Observatoire pour la Minéralogie, l'Eau, les Glaces et l'Activité (OMEGA; e.g., Ody et al., 2012; Poulet et al., 2009). Based on these datasets, Noachian (3.7-4.1 Gya) highlands material is relatively enriched in olivine and low-calcium pyroxene (LCP) compared to Hesperian-age (3.0-3.7 Gya) or younger lavas, in which LCP is nearly absent and high-calcium pyroxene (HCP) is more abundant (Mangold et al., 2010; Mustard et al., 2005; Viviano et al., 2019).

Further investigations have revealed variable magmatic lithologies at smaller spatial scales on Mars. Christensen et al. (2005) observed a range of compositions from olivine basalt to dacite in Syrtis Major using the Thermal Emission Imaging System (THEMIS), indicating highly evolved magmas likely formed by fractional crystallization in martian magma chambers. Feldspar-rich materials were identified north of Hellas and Argyre Planitiae and in Xanthe Terra using CRISM spectra (Carter and Poulet, 2013; Wray et al., 2013). While these authors invoked felsic volcanic or anorthositic origins, Rogers and Nekvasil (2015) showed that large plagioclase phenocrysts in

mixture with as much as 50% HCP could reproduce the observed CRISM signatures, proposing fractional crystallization of basaltic magmas at depth as an alternative mechanism. Recently, CRISM detections of hydrated silica at Gale Crater (Fraeman et al., 2016; Seelos et al., 2014) were identified by the Mars Science Laboratory (MSL) as a silicic volcanoclastic layer (Morris et al., 2016) suggesting an evolved magma source and extending at least 17 km laterally (Czarnecki et al., 2020).

Volcanic units on the Moon are also not petrologically homogenous (e.g., Martinot et al., 2018). Within the mare basalts, chemical variability observed in titanium, aluminum, and potassium content requires heterogeneity in fractional crystallization, assimilation of wall-rock, and source magma composition (Neal and Taylor, 1992). In addition, fragments of evolved lunar felsite/granite with crystallization ages spanning ~500 Myr occur in Apollo soil samples (Nyquist and Shih, 1992), suggesting that magmatic evolution processes took place over an extended period on the Moon. Analysis of Diviner Lunar Radiometer mid-IR spectra have shown that areas of quartz, Si-rich glass, and/or alkali feldspars indicative of intrusive and extrusive high-silica magmatism are present on the lunar near side (Glotch et al., 2010).

Significant magmatic evolution is also hypothesized to have occurred on Venus (Gilmore et al., 2015, 2017), although direct compositional measurements from X-ray fluorescence are limited to the Vega and Venera program lander missions. While compositions similar to tholeiitic basalts were measured at most sites, potassium-enriched rocks proposed to be akin to alkaline basalts or possibly intermediate composition crustal material were also identified at two landing sites (Basilevsky et al., 1992; Kargel et al., 1993; Nikolaeva and Ariskin, 1999; Shellnutt, 2019; Surkov et al., 1983). Remote estimates of surface mineralogy are more difficult on Venus owing to its thick CO₂-rich atmosphere that is opaque at most TIR and VNIR wavelengths. However, near-infrared atmospheric windows between 0.75-1.18 μm coincide with the ~1 μm absorptions from iron present in mafic minerals and glasses, allowing for some remote sensing analyses. Data from the Venus Express and Galileo missions showed that the tessera and highlands surfaces had low thermal emissivity in some of these atmospheric windows compared to the basaltic plains, which has been interpreted to be indicative of evolved felsic rocks (Hashimoto et al., 2008; Mueller et al., 2008). Next-generation Venus instrumentation has been proposed to create global maps of Venus in these atmospheric windows to assess surface rock types, iron content, and redox state

(Helbert et al., 2019). Understanding the variability and ambiguity that exists in near-infrared spectra of natural igneous rocks is critical for future interpretations of Venus surface mineralogy.

2.1.2 Crystallinity

While intrusive igneous material can be fully crystalline, extrusive volcanic material typically contains a silicate glass component, formed under faster cooling rates that prevent complete crystallization of minerals. Fast cooling rates are influenced by factors such as eruption style and emplacement rate, so remotely identifying volcanic glass can provide clues about magmatic volatile content and environmental conditions. On Earth, lava flows can contain up to tens of wt.% glass, whereas explosive eruptions can form up to fully glass deposits (e.g., Wall et al., 2014).

Effects of Glass on TIR and VNIR Spectra

Due to its disordered structure, glass exhibits absorption features in VNIR and TIR spectra distinct from those of primary crystalline minerals (Adams et al. 1974; Cannon et al., 2017; Carli et al., 2016; Cloutis et al. 1990a; Crisp et al. 1990; Horgan et al. 2014; Minitti and Hamilton, 2010; Minitti et al., 2002). At TIR wavelengths, glass exhibits a broad Si-O emissivity minimum near 1000 cm⁻¹ that shifts to longer wavelengths with decreasing SiO₂ content (Byrnes et al., 2007; Lee et al., 2010; Minitti and Hamilton, 2010; Pisello et al., 2019; Walter and Salisbury, 1989). It is currently unclear whether other chemical differences play a role in altering TIR spectra. Devitrification can split the main Si-O emissivity feature into two features due to the formation of SiO₄ chain and sheet structures (Crisp et al., 1990; Farrand et al., 2016). Previous quantitative analyses of volcanic rocks in TIR have included few to no glass endmembers in unmixing models, in part due to the previous lack of available spectra of appropriate silicate glasses. In particular, Wyatt et al. (2001) noted consistent model underestimation of glass contents that they ascribed to unrepresentative glass endmembers. The spectral effects and detectability of glass in TIR spectra of natural volcanic deposits remain understudied.

Since those early unmixing studies, more glass and amorphous emissivity spectra have been published (e.g., Byrnes et al., 2007; Lee et al., 2010; Minitti and Hamilton, 2010; Rampe et al., 2012), and it is assumed that glass abundances can be accurately modeled in TIR remote sensing

data (e.g., Minitti and Hamilton, 2010); however, that assumption has not been rigorously tested. Furthermore, non-crystalline materials tend to have broad, non-unique spectral signatures in both TIR and VNIR that can make distinguishing between primary volcanic glass and secondary amorphous silicates ambiguous, illustrated by both glass and high-silica amorphous alteration materials matching the high-silica component of TES Surface Type 2 (e.g., Bandfield et al., 2000; Michalski et al., 2005; Rampe et al., 2012). With increased availability of glass TIR spectra, and therefore their usage in TIR spectral modeling of rocks, it is important to revisit TIR mixing studies to determine how well glass can be modeled alongside other minerals and secondary amorphous materials in volcanic rocks with different compositions.

In VNIR spectra, glass exhibits a broad absorption due to iron centered at wavelengths between 1.08-1.18 μm and sometimes a second broad absorption near 1.9 μm correlated with higher alkali content (Cannon et al., 2017; Horgan et al., 2014). At high abundances, the 1 μm band center and shape of glass is distinguishable from those of primary minerals such as olivine and pyroxene. However, because glass is translucent at VNIR wavelengths, Fe-bearing primary minerals tend to obscure the presence of glass in bimodal mixtures below about 50-70 wt.% glass (Horgan et al., 2014). In complex natural rocks, the extent to which moderate glass content may muddle spectral interpretations is unclear.

Glass on other Planetary Bodies

Volcanic and/or impact glasses are likely widespread on Mars and the Moon and may be present on Venus. On planetary bodies with atmospheric pressures low than Earth, exsolved gases must expand further to equilibrate with the atmosphere (or lack thereof), causing more magma fragmentation and gas release (Wilson and Head, 1994) and enhancing the likelihood of explosive volcanism. For example, on early Mars, magmatic volatiles and/or interaction with groundwater may have resulted in explosive volcanic activity, in contrast to later extrusive volcanism indicated by shield volcanoes and lava flows (Wilson and Head, 2007).

On Mars, previous studies have identified deposits potentially consistent with volcanic tephra based on morphology and thermophysical properties (e.g., Edgett, 1997; Hynek et al., 2003). Volcanic and/or impact glass has also been detected by multiple landed campaigns. Rover analysis at Gusev crater found silicate glass to be a possible component of the plains basalts and Columbia Hills rocks (Ruff et al., 2006), and some of the Columbia Hills rocks (e.g., Clovis,

Wishstone classes) are proposed to be of explosive volcanic origin based on texture (Squyres et al., 2006; Wilson and Head, 2007). At Gale crater, potential impact glass spherules were directly imaged by the Mars Science Laboratory rover (Minitti et al., 2013). Volcanic glass and/or impact melt is also a component in some basaltic martian meteorites (e.g., McCubbin et al., 2016; Mikouchi et al., 2004). Analysis of OMEGA and CRISM spectra in the northern lowlands has identified regionally extensive glass-rich sediments (Horgan and Bell, 2012; Soare et al., 2015), and glass has been modeled in CRISM spectra of central peaks of impact craters, in impact strewn fields, and in the Nili Fossae capping unit (Cannon and Mustard, 2015; Cannon et al., 2017). Additionally, spectra of Amazonian age (<3.0 Gyr) terrains in the Tharsis and Elysium volcanic provinces indicate possible glass mixed with olivine and spectrally dominant HCP (Viviano et al., 2019).

Pyroclastic glass and impact melt occur in surface soils on the Moon (e.g., Adams et al., 1974; Mustard et al., 2011; Tompkins and Pieters, 2010). Lunar impact breccias contain considerable glass, and some mare basalts exhibit interstitial, sometimes devitrified, glass (e.g., Apollo, 1973; Brown et al., 1975). Glass-rich lunar pyroclastic deposits have been identified based on their VNIR spectra and are spectrally distinguishable in the TIR (e.g., Bennett et al., 2016; Besse et al., 2014; Gaddis et al., 1985; Horgan et al., 2014; Jawin et al., 2015; Mustard et al., 2011; Weitz et al., 1998).

Although volcanic glass has not been directly identified on the surface of Venus, understanding whether or not glass exists, and in what quantities, is important because it provides insight into the cooling histories of venusian lava flows, which are still largely enigmatic in terms of their eruption style and properties (Mueller et al., 2017).

2.2 Field Site

The Three Sisters Volcanic Complex is a young, compositionally diverse volcanic cluster located in a convergent-margin volcanic belt in the Cascades Range in central Oregon, USA. The three main edifices (North, Middle, and South Sisters) are composite, glacially eroded stratovolcanoes with central edifices largely built in the past ~ 120 kyr. In this study, we use samples from North Sister and Middle Sister. The eruptive history and geochemical diversity of North Sister and Middle Sister were most recently described by Schmidt and Grunder (2009, 2011) and Calvert et al. (2018), and mapped by Hildreth et al. (2012). North Sister and Middle Sister

experienced major eruptive episodes between 120-50 ka and 50-15 ka, respectively. These eruptions formed basalt, andesite, dacite, and rhyolite, but were dominated by early mafic (<57 wt.% SiO₂) eruptions (Calvert et al., 2018). Although the glaciers have significantly retreated in the last 100 years, ice likely covered much of the Three Sisters semi-continuously for most of the past 200 kyr (Calvert et al., 2018). Steep-sided, glacially eroded valleys are present on all volcanoes, allowing access to fresh bedrock and internal portions of the edifices, and many eruptive units exhibit evidence of ice-magma interaction (Hildreth et al., 2012).

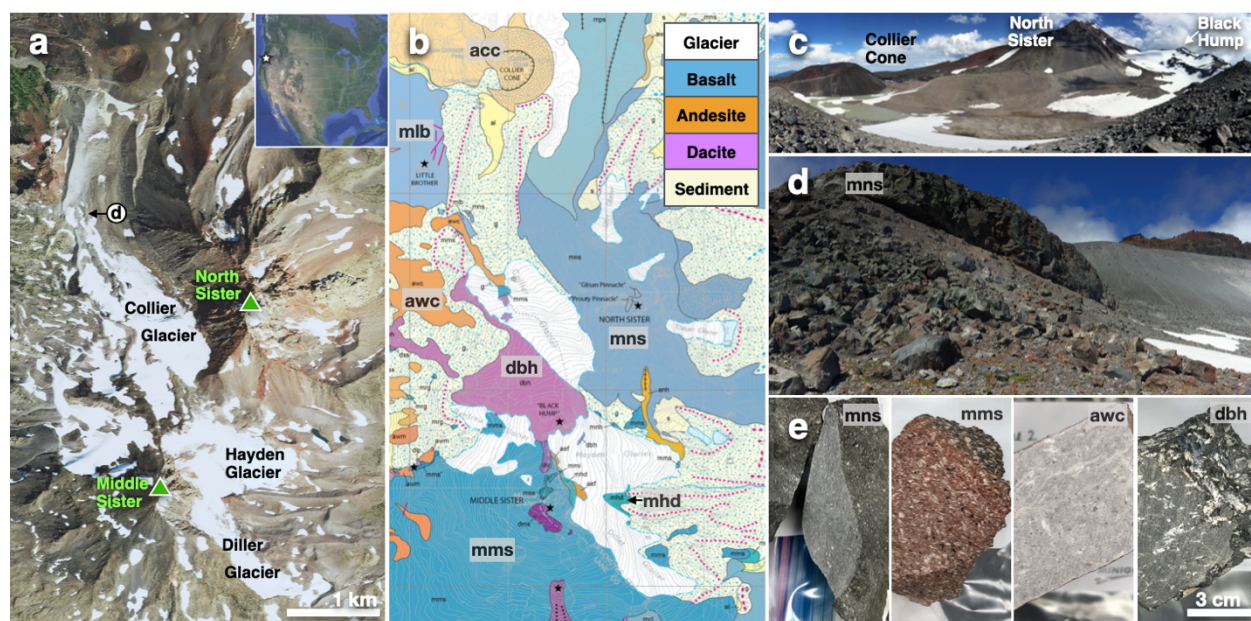


Figure 2.1. Field site overview. (a) Annotated satellite imagery (Quickbird, Google Earth). (b) Geologic map of the Three Sisters field site adapted from Hildreth et al. (2012), labeled with unit names most relevant to this study. See Supplemental Table S1 for sample locations. (c) East-facing view of North Sister and peripheral volcanic constructs. (d) Example flow outcrop of unit mns, located at point d in (a). (e) Example rock samples used in this study.

Table 2.1. Mapped Units used in this study.

Map Unit	Number of Samples	Physical Sample Description/Hand Mineralogy
<u>Basaltic Andesite</u>		
mns	14	Dark flows, sometimes vesicular with varying amounts of plag and olivine phenocrysts. Two samples are altered flow breccias.
mms	9	Dark, phenocryst-rich flows, sometimes vesicular, with plag and olivine phenocrysts.
mms'	1	Variant of mms. Dark, phenocryst-rich flow. Olivine-poor, cpx-rich.
mhd	2	Gray or red with plag and minor olivine phenocrysts.
mlb	1	Crystalline light-toned flow with plag and pyx phenocrysts, minor olivine.
mcl*	1	Gray, aphanitic, minor plag phenocrysts.
<u>Andesite</u>		
acc*	3	Cinder cone scoria/flow. Olivine and plag phenocrysts.
diller^	3	Similar to awc.
awc**	6	Crystalline light- to medium-gray flow. Plag and minor pyx phenocrysts.
<u>Dacite</u>		
dbh	1	Dark, with plag phenocrysts amid a glassy matrix.
<u>Rhyolite</u>		
roc	1	Altered tan, fine-grained pumice.

Units are from Hildreth et al. (2012). See Supplemental Figures S3-S11 for thin section photomicrographs.

^Unmapped andesite flows near Diller Glacier.

**Transitional between basaltic andesite/andesite.*

***Transitional between andesite/dacite.*

2.2.1 Applicability to Planetary Spectroscopy

This work focuses on application to Mars due to its robust spectral datasets, though this study is more broadly applicable to planetary volcanism. The geologic units sampled in this study have somewhat higher silica content (largely basaltic andesite, 52-55% SiO₂; Hildreth et al., 2012) compared to the typical crust of Mars (largely basaltic, 45-52% SiO₂; McSween et al., 2009), lower iron and magnesium (Taylor et al., 2006), and were derived from relatively hydrous magmas (2-3%; Hildreth et al., 2012; Ruscitto et al., 2010). Thus, Three Sisters volcanic materials are adequate

but not perfect geochemical analogs for the average martian crust. However, as previously discussed, recent remote sensing and rover investigations have observed an increasing diversity of elemental chemistry and magmatic processes on Mars, including alkaline and felsic rocks (e.g., Christensen et al., 2005; Cousin et al., 2017; Sautter et al., 2016; Udry et al., 2018). In addition, the basaltic andesite rocks in this study have mineralogy very similar to martian basalts (e.g., olivine, pyroxene, plagioclase feldspar) with solid solution chemical ranges comparable to those observed on Mars (Kanner et al., 2007; Koeppen and Hamilton, 2008; McSween et al., 2001; Milam 2010; Mustard et al. 2005). The glass content and composition of the Three Sisters are also acceptable analogs for drawing spectroscopic comparison. Finally, many eruptive units at the Three Sisters exhibit large plagioclase phenocrysts formed from fractional crystallization at depth, similar to plagioclase phenocryst formation scenarios proposed by Rogers and Nekvasil (2015) to explain VNIR plagioclase detections in the Noachian highlands on Mars (Carter and Poulet, 2013; Wray et al., 2013) and to plagioclase found at Gale crater (Payré et al., 2020). Therefore, these rocks constitute a useful suite of complex mixtures of Mars-relevant and more evolved mineral suites applicable for understanding spectral variability in natural volcanic systems.

2.2.2 Sample Suite

The edifices of North and Middle Sisters primarily expose basaltic andesite, with smaller exposures of andesite, dacite, and rhyolite (Hildreth et al., 2012; Figure 2.1a-d). Representative rocks from 11 major edifice-forming units of North and Middle Sister and several smaller units were collected in 2016 and 2017. Samples were collected directly from mapped outcrops where possible, and samples collected as float in the glacial valleys were identified and assigned to geologic units in the field using a hand lens, and were later confirmed using laboratory X-ray diffraction analyses. From 145 samples, 42 were chosen based on their physical character, spectral properties, and XRD-derived mineralogy as type examples of each unit for further analysis (Figure 2.1e; Table S1). Several of the mapped units at North and Middle Sister consist of a few to tens of individual lava flows with similar physical and chemical characteristics, so the chosen sample suite includes several samples from each of these units to capture in-unit mineralogical variability. Samples are named according to their respective geologic unit defined by Hildreth et al. (2012). The sample suite includes a wide range of states of magma evolution, crystallinity, oxidation, and alteration: 32 samples are classified based on the analyses discussed in detail below as unaltered

lava flow or scoria; 8 samples have undergone bulk oxidation and are hematite-bearing; and 4 samples experienced bulk aqueous hydrothermal alteration upon or soon after eruption, including 1 that experienced both oxidation and alteration. General descriptions of the samples from each unit are listed in Table 1, and detailed individual sample information is included in the Table S1.

2.3 Methods

Physical sample preparation was performed in order to focus on primary rock characteristics rather than surface properties. Rock coatings and surficial alteration were first removed with a rock hammer or tile saw when necessary, then fresh interiors were crushed using jaw and rotary crushers to acquire powdered sample for XRD, spectral, and XRF measurements.

2.3.1 Thermal-Infrared Emission Spectroscopy

TIR emission spectra were acquired at the Arizona State University (ASU) Mars Space Flight Facility using a Nicolet iS50R FT-IR spectrometer modified to measure emitted energy, the setup and calibration of which is similar to that described by Ruff et al. (1997). The sample chamber was purged with scrubbed air to avoid spectral contributions from water vapor and CO₂ (Lane, 2007). TIR spectra are sensitive to transparency effects from small particles that can be generated during crushing and grinding, so we applied two different methods to remove these fine particles. Crushed rock samples were prepared by wet-sieving to 125-250 μm to remove clinging fines; however, this process may preferentially remove fine-grained alteration products. To retain the fine-grained component, a separate set of pressed pellets were also prepared for 6 samples, using a hydraulic hand press to increase spectral contrast and reduce fine particulate features (Johnson et al., 1998; Salisbury and Wald, 1992). Both loose and pelletized samples were heated in black sample cups to 80 °C for at least 2 hours prior to measurement to increase signal to noise ratio, and were actively heated at 80°C during measurements to help maintain constant temperature. Spectra were measured over 200-2000 cm^{-1} at a spectral sampling of 2 cm^{-1} as an average of 512 scans recorded over ~10 minutes. This is comparable to TES data (~1650-200 cm^{-1} , 5-10 cm^{-1} sampling; Christensen et al., 1992). Raw data were calibrated to radiance using spectra of two blackbody targets at 70 and 100 °C measured in the same session, then processed to

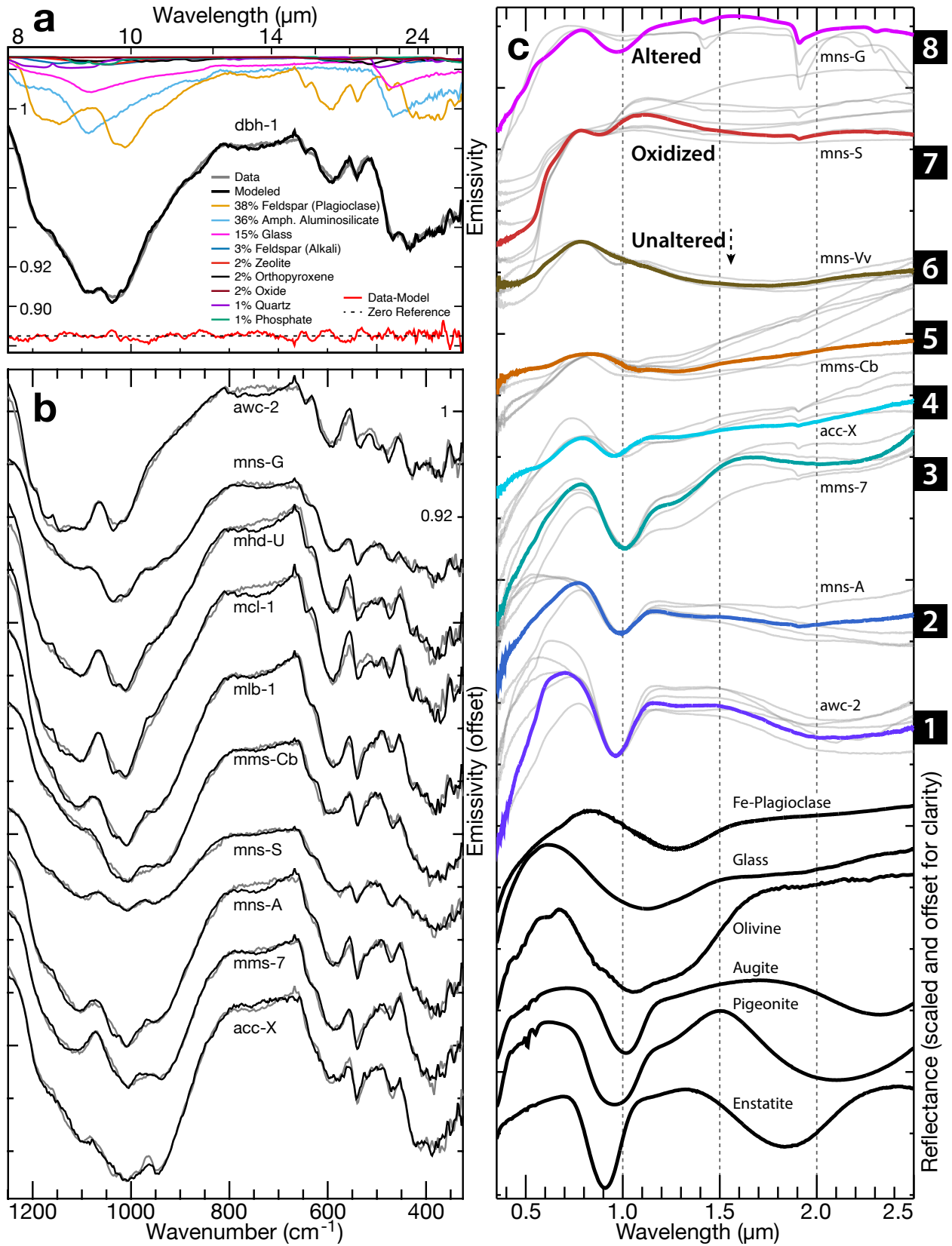
emissivity using the Planck function of the derived sample temperature (Christensen and Harrison, 1993; Ruff et al., 1997).

Individual emissivity spectra were quantitatively modeled with endmember spectra (Ramsey and Christensen, 1998) between 325-1250 cm^{-1} using a non-negative least squares minimization (Rogers and Aharonson, 2008; Figure 2.1a-b). We compiled a new “volcanic environments” endmember library from the ASU SpecLib (Christensen et al., 2000) and previously published sources to model our emissivity spectra (Table S8). This library includes all major crystalline minerals and amorphous materials likely to be present at the Three Sisters and is broadly applicable for modeling primary and secondary phases in laboratory spectra from volcanic environments. Crystalline mineral endmembers in the library include feldspar, pyroxene, olivine, iron and titanium oxides, amphibole, phyllosilicates, zeolites, carbonates, sulfates, and phosphates. The primary minerals chosen cover a large range of solid solution chemistry suitable for the Three Sisters and other mafic volcanic environments. Additionally, this library greatly improves on the number and chemical variability of amorphous and glassy endmembers compared to previous studies. Wyatt et al. (2001) used 4 glass endmembers in their deconvolutions of subalkaline volcanic rocks, which we update to 17 individual secondary amorphous materials and volcanic glasses in our library, including basaltic to rhyolitic glass, allophane, opal, and aluminosilicate gel. We also include a blackbody endmember to account for spectral contrast differences between sample and endmember spectra (Hamilton et al., 1997) and a slope endmember to account for small changes in sample temperature throughout the measurements (Ruff et al., 2006), both of which are normalized out of the reported endmember abundances.

TIR analysis was performed on 36 of the samples as indicated in Table S1. We first used the full endmember library in preliminary modeling efforts, but final models exclude endmembers that did not influence the modeled fit. While TIR deconvolutions initially provide volumetric abundances, we also calculated weight percent abundances using ideal endmember densities for more direct comparison to refinements of bulk X-ray diffraction patterns. Solid solution chemistries were derived as the weighted average of each modeled endmember for feldspars, olivine, and pyroxene. Bulk chemistry for each sample were estimated by summing weighted oxide chemistries of all endmembers (Tables S2-S7).

Figure 2.2. TIR and VNIR sample spectra. (a) Example thermal infrared emission spectrum and deconvolution model of sample dbh-1 (a dark, glassy dacite) with derived wt.% abundances listed by mineral group. Residual is shown in red in the same scale, with deviations from a perfect fit highlighted using a zero reference line. (b) Emission spectra (gray) and modeled fits (black) for a variety of geologic units in this study. In general, the models are very good matches to the measured spectra (rms <0.003). (c) All visible/near infrared sample spectra, grouped into Spectral Groups 1-8. Groups 1-6 are unaltered, Group 7 is oxidized, and Group 8 is altered. Colored bold spectra are representative of their respective group. Laboratory spectra shown in black for reference: Fe-plagioclase: Keck/NASA ReLab spectrum LR-CMP-183. Glass: University of Winnipeg PSF spectrum TEK004 (Horgan et al., 2014). Olivine: USGS spectrum KI3054 Fo66 (Kokaly et al., 2017). Augite, pigeonite, and enstatite: ReLab DL-CMP-073, -011, and -065 (Klima et al., 2007).

Figure 2.2 continued



2.3.2 Visible/Near-Infrared Spectroscopy

VNIR reflectance spectra of <125 μm crushed powders were collected at Purdue University using an Analytical Spectral Devices QualitySpec Trek spectrometer in the Planetary Spectroscopy Lab (Figure 2.2c). The Trek measures reflectance between 0.35-2.5 μm at standard incidence/emission angles of $0^\circ/30^\circ$ with a spectral resolution between 3-10 nm, resampled to 1 nm. This instrument has a similar spectral range and resolution to CRISM (0.4-3.9 μm , 6.55 nm sampling; Murchie et al., 2007). Each spectrum is the average of 100 scans collected over a $\sim 1\text{ cm}^2$ area.

We calculated Fe-bearing mineral spectral parameters for each of the loose crushed samples using the methods of Horgan et al. (2014) (Table S12). These parameters quantify the centers, depths, and asymmetries of the 1 and 2 μm absorption bands due to iron in common rock-forming minerals and can broadly discriminate between the spectral signatures of most Fe-bearing minerals as well as two-component ferrous mixtures. This method calculates a convex hull piecewise linear continuum between the shoulders of the absorption bands at both 1 and 2 μm , chosen to maximize the band areas, and then divides the original spectrum by the composite continuum to produce a continuum-removed spectrum. No smoothing is applied. The band centers are calculated as the minima of Gaussian fits to the continuum-removed absorption bands, and the asymmetries are calculated as the percent areal difference between the areas right and left of each band center below the continuum (Horgan et al., 2014).

2.3.3 Quantitative X-Ray Diffraction

Aliquots of all <125 μm crushed samples were reserved for bulk powder XRD. Each sample was spiked with 20 wt.% 1 μm crystalline corundum (Al_2O_3) as an internal standard, then spiked samples were ground in an agate McCrone micronizing mill with ethanol for 5 minutes to achieve a grain size <10 μm . After drying, each sample was back-loaded into a random powder mount (Bish and Reynolds, 1989). A diffraction pattern of each sample was collected using a PANalytical X'Pert PRO MPD X-ray diffractometer equipped with a spinner stage and Co-target X-ray tube operated at 45 kV and 40 mA at either the Center for Agronomy Science at Purdue University or at the NASA Johnson Space Center. Incident beam optics included a 0.02 radian Soller slit, 15-mm mask, fixed 0.5° divergence slit, and 1° anti-scatter slit, and diffracted beam optics included

a 0.02 radian Soller slit and fixed 0.5° anti-scatter slit. Powder mounts were scanned from 2 to 80° 2 θ at 0.017° steps with 125 sec measurement time per step.

We employed the X'Pert High Score Plus (PANalytical) software package and the PDF-4 Minerals 2018 diffraction database to derive quantitative mineral and X-ray amorphous abundances via Rietveld refinement (e.g., Bish and Howard, 1988; Rietveld, 1969). The scale factor, specimen displacement, unit-cell parameters, Caglioti peak width parameters, peak shape, and preferred orientation were allowed to vary during refinement to provide an acceptable fit (e.g., Bish and Howard, 1988; Rietveld, 1969). Once each model was produced, the calculated internal standard mass fraction was scaled alongside the other crystalline minerals to match the actual internal standard mass fraction, the remaining difference from 100 wt.% representing the abundance of X-ray amorphous material (Smith et al., 2018). Full-pattern Rietveld refinement of synthetic mixtures incurs absolute errors of about 1% or less (Bish and Howard, 1988); in multicomponent natural igneous mixtures, absolute errors are <3% (Bish and Post, 1993; Hill et al., 1993) with a detection limit of about 1% (Hill et al., 1993) that increases with increased peak overlap.

The crystal chemistry of solid solution phases can be derived from unit-cell parameters as refined in the Rietveld method (e.g., Bish and Post, 1993), and we performed this calculation for plagioclase and olivine using the equations by Morrison et al. (2018), which assume Ca-Na composition for plagioclase and Mg-Fe for olivine (Table S9). Although this assumption excludes minor elements that can substitute into the crystal structure of these minerals, we consider these equations valid for our samples, as other elements constitute <2 wt.% of plagioclase and <1 wt.% of olivine in our samples based on microprobe analysis. The residual standard error in solid solution chemistry calculations is 2.2 for plagioclase An# and 3.4 for olivine Mg# (Morrison et al., 2018). Pyroxene chemistries were not calculated in this manner, but rather differentiated as orthopyroxene (OPX) and clinopyroxene (CPX). The XRD-derived plagioclase and olivine chemistry should be considered an average, as the An# and Fo# in individual samples varies from core to edge in phenocrysts and between phenocrysts and microphenocrysts/groundmass. Since multiple plagioclase and olivine crystallographic structures were used in the refinements to allow these multiple chemistries, peak overlap prevented good separation of compositionally distinct endmembers. However, this did not inhibit average estimates.

2.3.4 Chemistry and Textural Analysis

Mineral Chemistry and Rock Texture

Mineral chemistries for 10 samples were measured using electron microprobe analysis (EMPA) at NASA Johnson Space Center (Table S10). These rocks are from 6 geologic units and were chosen to represent the variability in mineral chemistry present in the sample suite while being representative of their source units. Spot analysis of all major phases and glass in each sample were performed using a Cameca SX100 microprobe. Beam conditions of 1 μm spot size, 15 kV, and 10 nA were used for most mineral groups except for feldspar and glass, where a defocused beam was used for feldspar phenocrysts (20 μm) and matrix feldspar and glass (10 μm). For each phase, spot analysis was performed on at least three occurrences per crystal size (phenocryst or groundmass), with additional measurements on chosen phenocrysts to capture compositional zoning. Mineral chemistry was acquired by targeted measurements rather than gridded points. This option avoids potential mixing contamination along grain edges, but results should be considered a sampling rather than full range of mineral chemistries. In particular, minor phases (e.g., alkali feldspars) or solid solutions with a wide range of chemistries present (e.g., pyroxenes) may not be fully represented in this dataset, nor are representative average chemistries possible to calculate. Both microprobe electron backscatter images and petrographic thin sections were made for textural analysis; however, the backscatter images were found to be better indicators of rock microtexture, so here we discuss only the microprobe data. Thin section images can be found in Figures S3-S11.

Bulk Chemistry

We sent 11 samples to Activation Laboratories for quantitative bulk fusion XRF (Table S11). 5-10 grams of crushed, homogenized material for each sample was used to ensure representative composition. XRF reports wt.% oxides of 15 major and minor oxide species and was chosen for its direct comparability to TIR-derived bulk chemistry. These samples were chosen from four geologic units (mms, mns, mhd, and awc) as representative of the chemical and oxidation variability present within and across units for comparison with TIR-derived bulk chemistry and VNIR spectral parameters. Measurement errors are small compared to measured values for all major oxides.

2.4 Baseline Mineralogy, Chemistry, and Texture

2.4.1 XRF Bulk Chemistry

XRF bulk oxide measurements generally agree with chemical data reported for each unit by Hildreth et al. (2012). Most units represented in our samples are subalkaline (Le Bas et al., 1986). None of the samples in our suite can be considered primitive; all samples are low basaltic andesite or more evolved, with less than 6.0 wt.% MgO. However, the basaltic andesite samples contain minerals present in primitive compositions (e.g., olivine, pigeonite, augite; see sections below) applicable to spectral interpretations of more primitive rocks on other planetary bodies. Three oxidized, hematite-bearing rocks (mms-Cr, mns-Vm, and awc-3) were included in this analysis and appear otherwise unaltered compared to their reduced counterparts both in mineralogy and bulk chemistry.

2.4.2 XRD Mineralogy and Crystal Chemistry

Quantitative mineralogies derived from XRD measurements for all samples are shown in Table S9, and compared to TIR model results in Figure 2.3. Plagioclase feldspar occurs in all samples. Pyroxene occurs in all samples except the rhyolitic pumice, and olivine occurs in the basaltic andesites. Most samples also exhibit a peak best matched by alkali feldspar. In basaltic andesite samples, this peak is weak and matched by minor late-forming K-bearing albite or disordered anorthoclase; in more silicic samples, sanidine becomes the dominant alkali feldspar identified. Where oxide minerals were detected, weak and overlapping peaks made identification ambiguous, but refinements typically preferred magnetite over ilmenite. Hematite was detected in all but one of the samples identified by VNIR as hematite-bearing, indicating that at least some fraction of hematite in these samples is well crystalline.

Rietveld refinements indicate significant amorphous material is present in many samples. Amorphous-rich samples display a broad “hump” in diffraction patterns, indicative of material lacking long-range crystal structure (Klug and Alexander, 1974). Inclusion of the internal standard allows calculation of the wt.% fraction of this X-ray amorphous component without modeling the hump, which can be difficult to separate from the background at low abundances. This technique allows us to calculate amorphous abundances even at low wt.% in our samples, which we find range from 2-55 wt.% in lava flows and 22-57 wt.% in tephtras. Identifying amorphous materials

in diffraction data is challenging and can often lead to non-unique solutions because different X-ray amorphous materials can have similarly shaped humps, but EMPA and thin sections of unaltered samples confirm the presence of volcanic glass. In the most glass-poor flows, cristobalite, a common devitrification product of silicic volcanic glass, is present in abundances up to 11 wt.%.

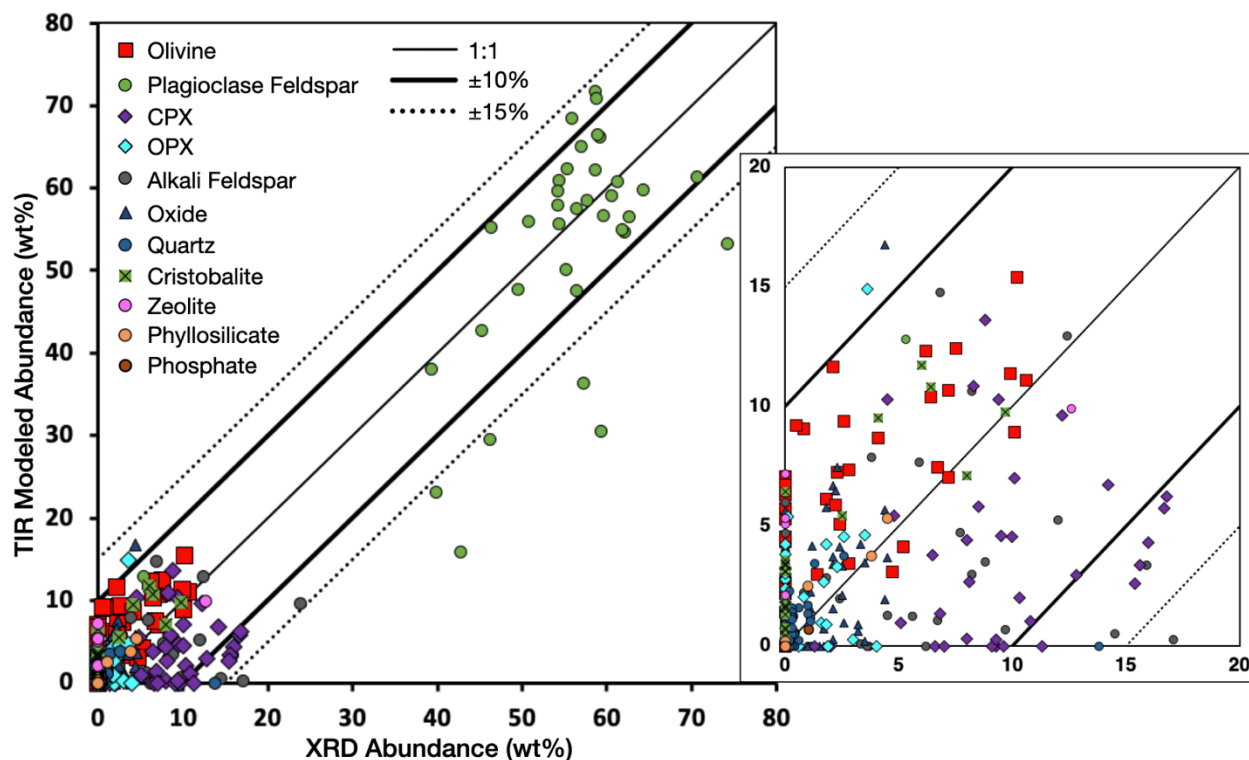


Figure 2.3. TIR deconvolved wt.% mineral abundances by group compared to abundances calculated from XRD refinements. Inset shows an enlargement of the lower-left corner of the larger plot. Amorphous abundances are shown in Figure 2.8a.

Plagioclase feldspar varies between 5 and 75 wt.% in our measured rock samples. In the crystalline fraction alone, plagioclase abundance exhibits no trends with volcanic rock type and is primarily anticorrelated with amorphous abundance. However, calculated average An# does exhibit an expected decrease (An₅₇ to An₂₈) with increasing magmatic evolution from basaltic andesite to dacite. Alkali feldspars vary significantly with rock type, from between 0-15 wt.% of albitic composition in the basaltic andesites, to up to 30 wt.% sanidine-like compositions in the more evolved units. The other major crystalline components are olivine and pyroxene. Olivine occurs in the basaltic andesite units between 0.5-11 wt.%, and is absent in the more evolved units.

Pyroxene primarily occurs as CPX as augite and pigeonite at the 2-20 wt.% level, but up to 4 wt.% enstatitic OPX is present in all rock types, including in the more evolved samples.

Minor and trace phases vary significantly between samples. Total oxide minerals are modeled at up to 4.5 wt.%; however, specific oxides are not always well constrained. Refinements typically identified ~2 wt.% magnetite or ilmenite, but the major peaks of these minerals were largely obscured by peaks from other phases (e.g., pyroxene), preventing confident estimates of the exact abundance or composition of reduced oxide minerals. However, unique hematite diffraction peaks were detectable, and hematite is present in some samples below 1 wt.%. The few altered samples in our suite, defined by their visibly altered appearance and VNIR spectra, contained phyllosilicate clay minerals and zeolites at <5 wt.% and <13 wt.% respectively. We did not identify the clay minerals. Unlike the other mineral groups and amorphous material, for which we consider abundances to be fully quantitative, the clay mineral abundances should be regarded as semi-quantitative here due to the complexities in clay mineral structure and the absence of suitable reference patterns for Rietveld refinements (Moore and Reynolds, 1997). This applies to only 3 samples having <5 wt.% clay abundance, so the XRD data as a whole can be considered quantitative. Trace quartz occurs in nearly all samples, typically between 0.1-1.3 wt.%, which is consistent with normative calculations. Trace phosphate (<0.4 wt.% fluorapatite) is modeled in 3 samples. XRD results broadly agree with CIPW normative mineralogy calculated from XRF data.

2.4.3 EMPA Chemistry and Texture

At both hand sample and microscopy scales, the effusive units at the Three Sisters exhibit large phenocrysts amid a fine-grained groundmass (Figure 2.4a-c). This porphyritic texture occurs when large, slowly cooled crystals formed during fractional crystallization in a subsurface magma chamber are carried rapidly to the surface by volcanic eruptions, during which the lava cools relatively rapidly to form a partly crystalline, partly glassy matrix. In our samples, the composition and abundance of phenocrysts, groundmass crystals, and glass varies within and across rock units due to rock chemistry and eruptive history.

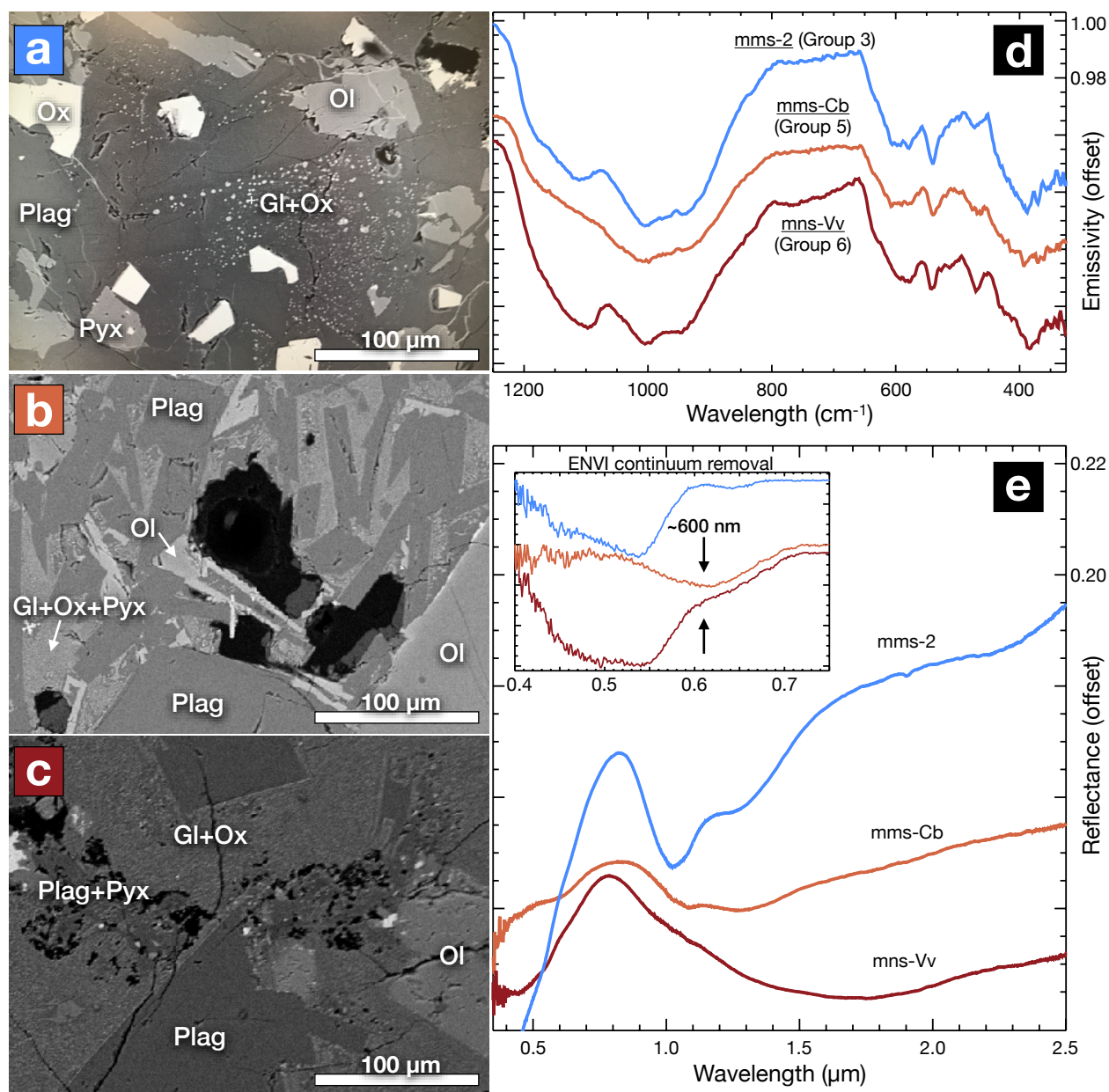
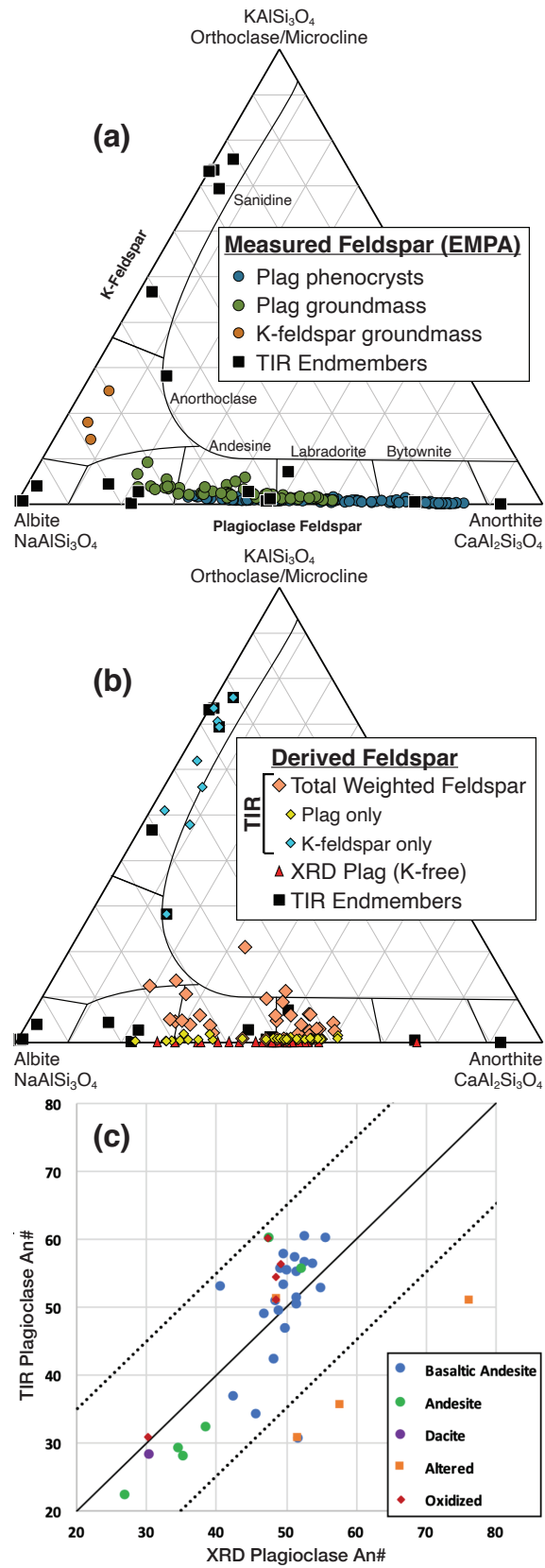


Figure 2.4. Effects of microtexture on spectral properties. (a-c) Electron backscatter images of basaltic andesite samples with similar crystalline mineralogies (a) mms-2, (b) mms-Cb, and (c) mns-Vv, exhibiting a range of microtextures. Ol=Olivine, Pyx=Pyroxene, Plag=Plagioclase, Ox=Oxide, Gl=Glass. Pyroxene often occurs as discrete microphenocrysts like in (a), but in some samples is limited to intimately mixed microphases as in (b) and (c). Similarly, oxide minerals typically occur as discrete microphenocrysts or as blebs in the interstitial glass, but are sub-micron scale in (b) and (c). (d) Thermal emission spectra of the samples. mms-Cb has more muted, rounder features due to higher glass and lower feldspar content. (e) Visible/near-infrared spectra showing suppressed 1- μm features in mms-Cb and mns-Vv alongside the appearance of a small 0.6 μm absorption (inset) likely due to oxides.

Plagioclase feldspar occurs as phenocrysts, microphenocrysts, and identifiable groundmass crystals in all samples. Plagioclase chemistry measured by EMPA varies widely as a consequence of magmatic evolution, compositional zoning, and differences between phenocryst and groundmass plagioclase. Overall An# decreases in increasingly evolved samples, in agreement with XRD results. An# of phenocrysts ranges from An49 at the edges to An92 in the cores. Small groundmass plagioclase crystals are more albitic on average than the phenocrysts (An35-An75; Figure 2.5a). Although plagioclase is the major feldspar phase within the groundmass, Rietveld refinements indicate potassium-bearing albite or anorthoclase occurs as a minor phase in most samples, likely forming as microphases in (and anticorrelated with) glass in the last stage of rock cooling and crystallization. Although targeted identification of these phases was difficult due to similarity to plagioclase in electron backscatter images, line scans confirmed the presence of anorthoclase in the groundmass of these rocks that is compositionally similar to XRD predictions. We note that plagioclase phenocrysts and groundmass in analyzed samples contain ~0.3-1.1 wt.% FeO based on EMPA, sufficient to theoretically produce a VNIR absorption band near 1.25 μm in the absence of other more absorbing mafic minerals (Adams and Goullaud, 1978; Bell and Mao, 1973; Cheek et al., 2013; Cheek and Pieters, 2014).

Figure 2.5. Comparison of EMPA measured and XRD/TIR derived feldspar compositions. (a) Solid solution composition of feldspar phases in all 10 rocks measured by EMPA. TIR library endmembers are included for comparison with (b). (b) Composition of feldspar phases for all 36 rocks with TIR and XRD derivations. The XRD-derived compositions (red triangles) only consider K-free albite-anorthite solid solution and plot along the bottom axis. The weighted average of all TIR-derived feldspar in each rock (orange diamonds) is broken out into average K-feldspar composition (teal diamonds) and average plagioclase composition (yellow diamonds) for each rock. (c) Mol% anorthite (An#) derived from TIR and XRD methods. Symbols indicate rock type in unaltered rocks, or alteration and oxidation in altered or oxidized rocks.

Figure 2.5 continued



Pyroxene occurs as microphenocrysts and groundmass crystals of augite, pigeonite, and OPX, and together with plagioclase comprises the identifiable groundmass crystals in most samples. We find augite in all measured samples within a limited chemical range of $\text{En}_{40-50}\text{Fs}_{15-25}\text{Wo}_{30-40}$ (Figure 2.6), with groundmass augite slightly more enriched in iron than in the microphenocrysts. Pigeonite was identified less frequently as $\text{En}_{40-55}\text{Fs}_{30-50}\text{Wo}_{7-18}$, occurring as rims on augite microphenocrysts or in the groundmass. We did not observe exsolution lamellae. OPX ($\text{En}_{55-75}\text{Fs}_{25-40}\text{Wo}_{2-5}$) was observed as microphenocrysts and groundmass crystals in dacite, as well as in small vesicles or rimming olivine in basaltic andesite.

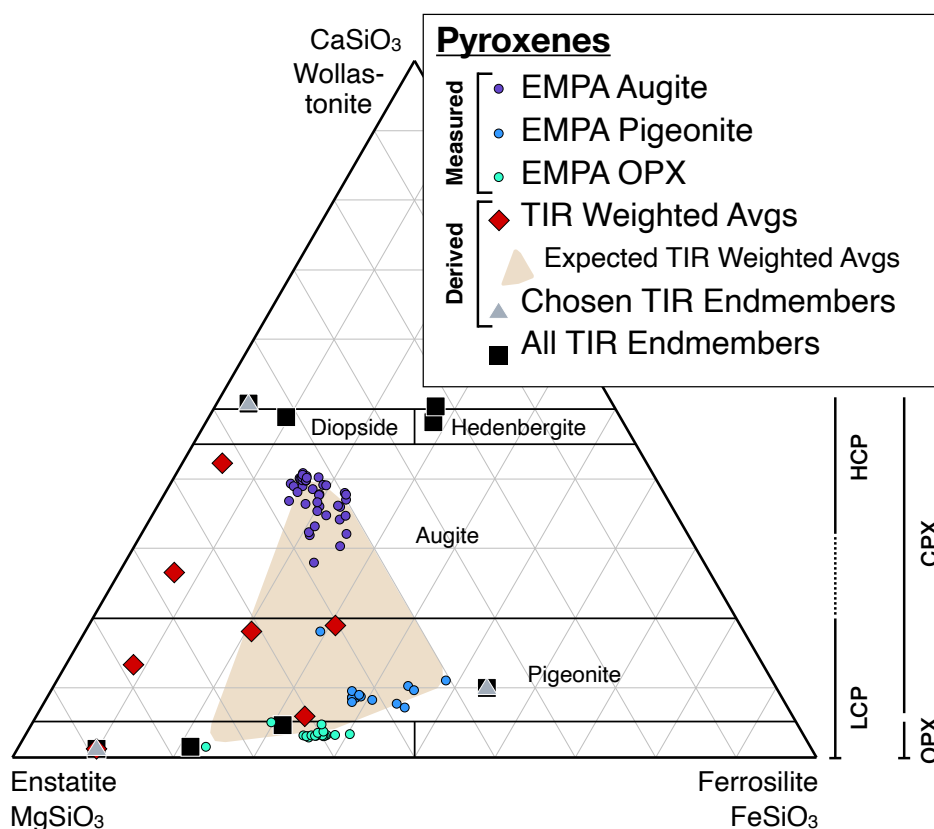


Figure 2.6. Pyroxene ternary diagram showing EMPA-measured (circles) and TIR-derived (diamonds) pyroxenes for EMPA-measured samples. TIR results are displayed as the abundance-weighted average of all modeled pyroxene chemistries for each rock. TIR results are acceptable if they plot within the shaded area describing the compositional mixing range allowable by EMPA.

Olivine occurs as phenocrysts and sometimes microphenocrysts in the basaltic andesites. Olivine phenocrysts exhibit either no compositional zoning or a thin rim of relatively Fe-rich

olivine. Similar to plagioclase, olivine phenocrysts (Fo₆₁-Fo₈₃) are less evolved than olivine groundmass (Fo₄₈-Fo₇₅), though groundmass olivine is rare.

Oxide minerals occur as microphenocrysts and groundmass crystals as well as microphases within glass (Figure 2.4a-c). Measured oxide microphenocrysts were recalculated to obtain both FeO and Fe₂O₃ using the methods of Droop (1987) and plot near the ilmenite-hematite solid solution series between about Il₁₅-Il₉₅ (Figure 2.7). Titanomagnetite was not observed directly, but offset from the titanohematite line was observed, which could indicate fine intergrowth with titanomagnetite.

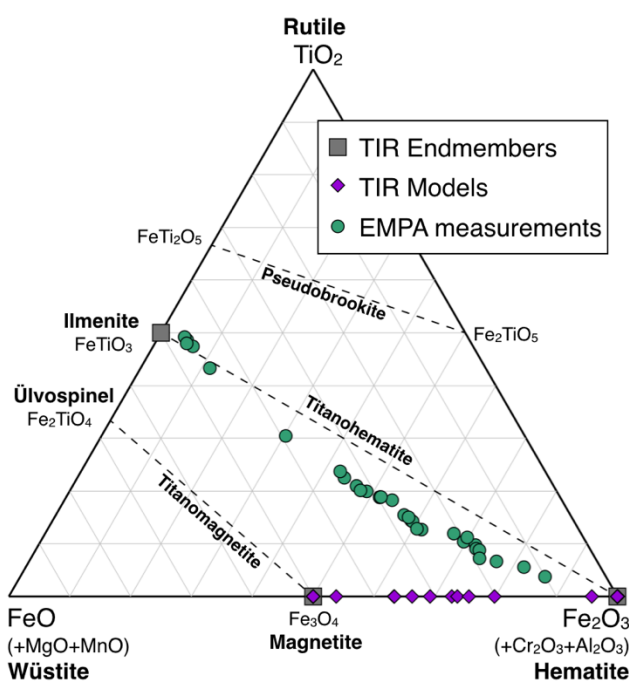


Figure 2.7. Fe-Ti oxide ternary showing EMPA-derived chemistries (circles) compared to TIR endmembers (squares) and TIR modeled average oxide mineral chemistry (diamonds).

Interstitial glass was difficult to measure within the analyzed samples, often owing to chemical and electron backscatter similarity to feldspar as well as the presence of exsolved microphase oxide minerals and pyroxene, so reported glass chemistries may have some error from contamination by these components. Measured glass chemistry was typically feldspar-like with higher abundances of Mg, Fe, Ti, and/or Si than in crystalline feldspar. Additionally, glass chemistries often varied significantly between measurements within a sample. Generally, higher-Si glass was observed in more evolved samples and in more crystalline samples.

2.5 Petrologic Properties Derived from TIR Spectral Models

In this section, we use TIR spectral models to derive key petrologic parameters (mineral abundances, mineral chemistries, and bulk chemistry), and compare the results to those same parameters as derived from the traditional laboratory methods described above.

2.5.1 TIR Spectral Properties

In these samples, the Si-O fundamental stretching mode is the dominant spectral feature and occurs between 900-1100 cm^{-1} , with weaker Si-O bending modes occurring near 500 cm^{-1} . We observe a general shift in the Si-O fundamental band center from ~ 950 to ~ 1075 cm^{-1} with increasing SiO_2 content, which is commonly attributed to shortened Si-O bonds with increasing silica polymerization (Michalski et al., 2003; Figure 2.2b). Below 650 cm^{-1} , absorptions due to Si(Al)-O bending and deformation and M-O-Si(Al) deformation (M = e.g., Mg^{2+} , Fe^{2+} , Al^{3+}) are present in spectra of all samples. An asymmetric absorption near 460-470 cm^{-1} indicative of Si-O bending in glass and other high-silica materials (Minitti and Hamilton, 2010; Ruff and Christensen, 2007) appears in relatively glass-rich samples.

Some systematic misfits are observed in the TIR models, which can be seen in Figure 2.2b by regions of the spectra with more separation between the model fit and original spectrum. Absorptions near 540 cm^{-1} attributable to feldspar are sometimes under- or over-modeled in strength, which we attribute to minor chemical differences between available library feldspar endmembers and feldspar in the samples. Many modeled spectra also exhibit a small emissivity peak near 1160 cm^{-1} , not present in most sample spectra, due to quartz that is over-modeled to fit the left edge of the Si-O stretching reststrahlen band. The right edge of the reststrahlen band near 800-900 cm^{-1} also exhibits small model misfits for most spectra, which is related to overestimation of Fe-rich olivine. Nevertheless, overall differences between sample spectra and model fits are small (rms error < 0.003).

2.5.2 TIR Mineral Abundances

Plagioclase feldspar is the most abundant modeled mineral group, ranging from 13-71 wt.%. In more evolved samples, alkali feldspars are modeled at up to 15 wt.%. Amorphous materials (grouped as amorphous aluminosilicates, secondary amorphous silicates, and primary glass) are

modeled at 4-61 wt.%, and abundances are not correlated with magmatic evolution, but are inversely correlated with plagioclase abundance. Cristobalite is modeled in some samples, but only in significant quantities (5-15 wt.%) in samples with < 15 wt.% modeled amorphous material, consistent with an origin as a devitrification product of glass. Olivine is modeled in most samples, including the evolved rock types, at up to 15 wt.%, with highest abundance in the basaltic andesites. CPX (including pigeonite) is the dominant modeled pyroxene type and is predicted in most samples at up to 14 wt.%, while OPX is typically modeled at < 5 wt.%. Iron oxides are modeled at up to 8 wt.%, although hematite and goethite often erroneously occur in models of unoxidized samples. Quartz and apatite are modeled in the 0 to 2 wt.% range for most samples. Phyllosilicates and zeolites are typically absent in models of unaltered samples, or occur rarely at < 3 wt.% abundance, but occur at up to 5 wt.% and 10 wt.%, respectively, in models of altered samples.

TIR-derived wt.% mineral abundances are directly compared to XRD-derived quantitative mineralogy in Figure 2.3. We find that all mineral groups are largely modeled to within +/-10 wt.% of corresponding XRD refinements (Figure 2.3), similar to previous studies using petrographic or microprobe baseline techniques (Feely and Christensen, 1999; Hamilton and Christensen, 2000; Wyatt et al., 2001). In addition, most mineral groups do not exhibit strong underestimations or overestimations in TIR modeling, though some systematic effects are observed. Plagioclase feldspar is typically well-modeled for unaltered samples, but abundances were modeled with more than 15 wt.% error for five of the six altered or oxidized samples. Olivine is systematically overestimated by 4 wt.% on average, due to overestimation of low Fo# ($\text{Fo}_{<50}$) olivine. The overestimation of olivine propagates to systematic errors in modeled abundances of other minerals because modeled abundances are normalized to 100% (Wyatt et al., 2001). For example, CPX exhibits reststrahlen bands similar to olivine in the 900 cm^{-1} region and is the only major mineral group to exhibit systematic underestimation (by 5 wt.% on average), consistent with erroneous replacement by low-Fo# olivine that affects even the andesite and dacite rocks. However, CPX exhibits another strong band near 1100 cm^{-1} that does not occur in olivine. A likely substitute for this band would be a silicic endmember such as quartz or a high-silica glass that has high wavenumber absorptions. Quartz likely contributes at least partially to replacing this band, and both quartz and cristobalite are slightly overestimated by 0.5-2 wt.%. This misfit is apparent in the

1160 cm^{-1} quartz emissivity peak weakly present in model outputs but not clearly identifiable in measured spectra.

Orthopyroxene, phosphate, zeolite, oxide, and phyllosilicate groups are mostly identified at the <5 wt.% level in Rietveld refinements of XRD data and are thus below the 5-10% TIR detection limit (Feely and Christensen, 1999). In addition, refinements may also struggle to detect minor phases below a few wt.% when peaks overlap with those from major phases. In TIR models, endmembers with low modeled abundances often serve to slightly improve overall fits and effectively constitute “noise” in the final result (Feely and Christensen, 1999). So, the observed lack of tight 1:1 modeled abundances in this detection threshold region is expected. However, we note that TIR models also never predict >10 wt.% abundance of these groups when not corroborated by XRD. Furthermore, the phyllosilicate group exhibits a surprisingly tight fit between TIR and XRD abundances below 5 wt.% and is never falsely modeled above 0 wt.% in unaltered samples, although the XRD phyllosilicate abundances are semi-quantitative as previously stated.

TIR models of amorphous material abundance are largely accurate to within 10% of XRD-derived values (Figure 2.8a). This is true across the entire range (2-57 wt.%) of XRD-derived amorphous abundances. The only exceptions are oxidized/altered samples with relatively high XRD-derived amorphous abundances, which exhibit overestimated amorphous abundances in TIR at the expense of underestimated plagioclase feldspar mentioned above. This general success of our models in estimating amorphous components contrasts with the results of Wyatt et al. (2001), who observed consistent underestimation of their glass endmembers in TIR deconvolutions of volcanic rocks. They attributed this mismatch to a lack of glass endmembers with the correct compositions and/or crystallinities. The success of our models in estimating amorphous abundance is most likely due to incorporation of a wider variety of glass and X-ray amorphous compositional and textural endmembers into our models.

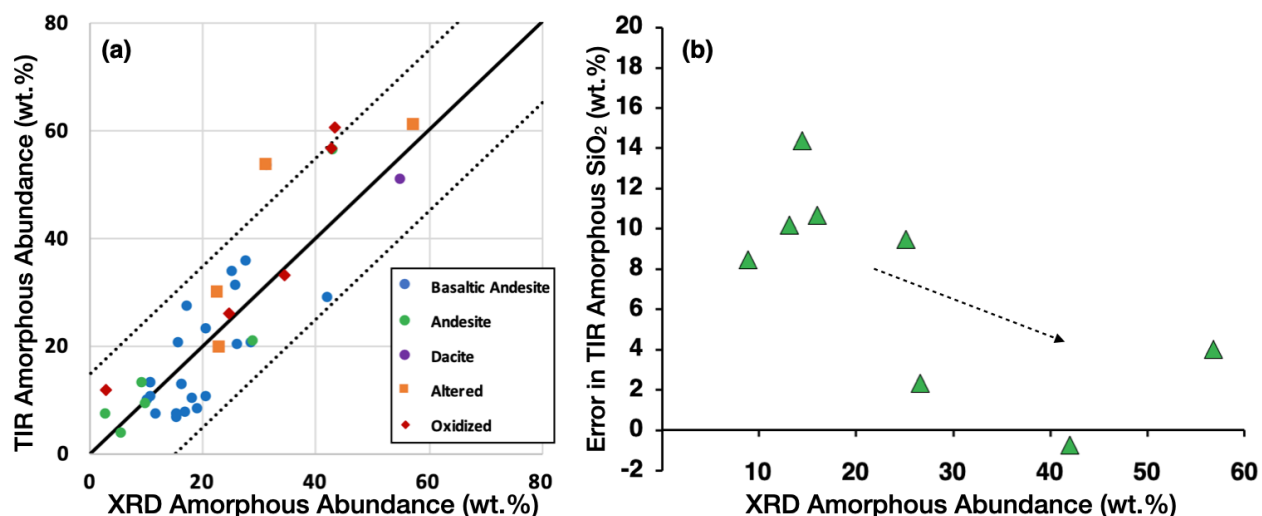


Figure 2.8. TIR model results for amorphous material. (a) TIR-derived amorphous abundance plotted against XRD-derived amorphous abundance. Symbols indicate rock type in unaltered rocks, or alteration and oxidation in altered or oxidized rocks. (b) Trend in the error in wt.% SiO₂ of TIR-derived amorphous material, calculated as the difference between the TIR-derived wt.% SiO₂ of the amorphous component and the EMPA-estimated wt.% SiO₂ of glass for the same sample, as compared to total XRD wt.% amorphous.

2.5.3 TIR Mineral Compositions

Volcanic rocks typically exhibit chemical zoning within minerals as well as variability between phenocrysts and groundmass crystals, usually addressed by including multiple endmembers in the fit (Hamilton and Christensen, 2000). Here, TIR mineral chemistries are calculated as weighted averages of each modeled endmember, and compared to compositions calculated from XRD-derived unit-cell parameters and measured directly by EMPA.

Feldspar

Figure 2.5 shows feldspar solid solution compositions from EMPA measurements, XRD data, and TIR modeled averages. Plagioclase feldspar chemistry is modeled in TIR between An₆₁ to An₂₂ and matches XRD results largely to within 10 An#, similar to previous studies of igneous rocks (Hamilton and Christensen, 2000; Wyatt et al., 2001). Additionally, the observed decrease in An# in increasingly evolved rock types is accurately reproduced in TIR models. Both XRD and TIR An# exhibit a “sodic bias” compared to the range detected in EMPA, which occurs due to a greater volumetric proportion of albitic groundmass over anorthitic phenocrysts (Milam et al.,

2004). However, the plagioclase compositions of two of three altered rocks are poorly modeled, as the An# is significantly underestimated.

TIR feldspar results generally overestimate potassium content compared to EMPA measurements (Figure 2.5a-b). Since alkali feldspar abundance is correctly modeled on average (± 10 wt.%), the discrepancy arises due to library endmember chemistries. This is in contrast to Hamilton and Christensen (2000) who observed overestimated alkali feldspar abundance, and attributed their result to a lack of available glass and pigeonite library endmembers. Rietveld refinements and EMPA measurements indicate that most of the alkali feldspar in our samples is anorthoclase, but only one anorthoclase endmember was available in source spectral libraries at the time of this study, whereas the rest of the alkali feldspar endmembers used were compositionally sanidine. It is likely that the feldspar spectral endmembers are not spectrally similar enough to those in our rocks to allow accurate chemical interpolation. This finding is similar to results for higher alkali feldspar abundances in alkaline rocks (Dunn et al., 2007).

Olivine

Modeled olivine chemistry varies widely from Fo₇₂ to Fo₁ for all samples, but mostly falls between Fo₇₀ and Fo₄₀ for samples with > 8 wt.% modeled olivine. Figure 2.9 compares XRD- and TIR-derived Fo#. TIR models tend to underestimate average Fo# due to overestimated abundances of low-Fo# olivine, which is modeled in minor abundance even in olivine-free andesite and dacite samples and discussed in Section 8.1.

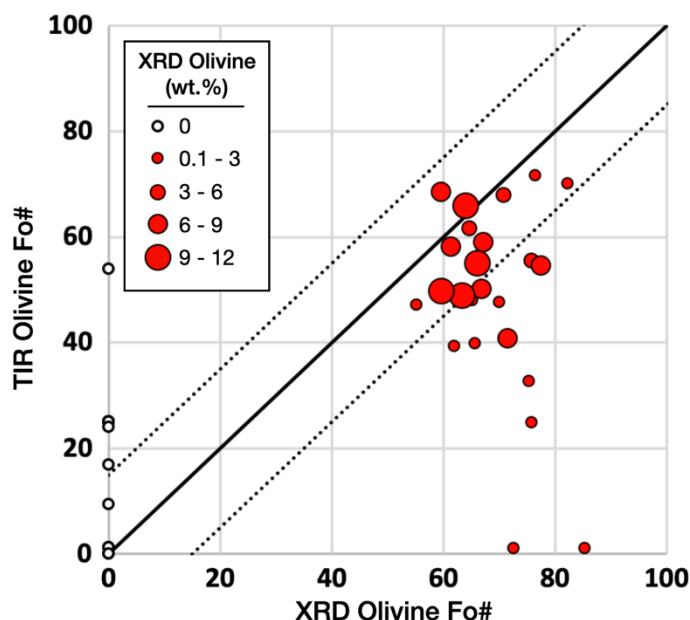


Figure 2.9. Mol% forsterite (Fo#) of olivine derived from TIR models and XRD results, showing overestimation of Fe-rich olivine in some TIR models, most likely due to transparency effects. Point size corresponds to XRD-derived olivine abundance. Rocks where olivine was not detected by XRD but was falsely modeled by TIR plot along the y-axis.

Pyroxene

EMPA indicates that the pyroxenes in our sample suite form compositional clusters of augite, pigeonite, and OPX (Figure 2.6). TIR models of these samples tend to predict more Fe-poor compositions than expected and fail to reliably plot in the compositional space described by EMPA. Previous studies have also encountered difficulty in achieving more than moderate success in estimating pyroxene compositions of extrusive rocks using TIR (e.g., Dunn et al., 2007; Hamilton and Christensen, 2000; Hamilton et al., 1997; Wyatt et al., 2001).

Iron oxides

Figure 2.10 shows the effect of differing oxide minerals on TIR and VNIR spectra. Due to low abundances, oxide minerals do not strongly affect the shape of TIR spectra for our sample suite and are accordingly not strongly constrained in abundance or composition. For this reason, past TIR studies have sometimes excluded oxide minerals from unmixing models altogether (e.g., Wyatt et al., 2001). All EMPA measurements fall along the ilmenite-hematite solid solution series (Figure 2.7), yet ilmenite is not selected in any TIR models. Instead, TIR models primarily select

hematite and magnetite as the predominant oxides. Furthermore, modeled compositions in this two-component mixing space appear to have very little correlation with EMPA chemistry, indicating that Fe-Ti oxide composition is relatively unconstrained by TIR for these samples.

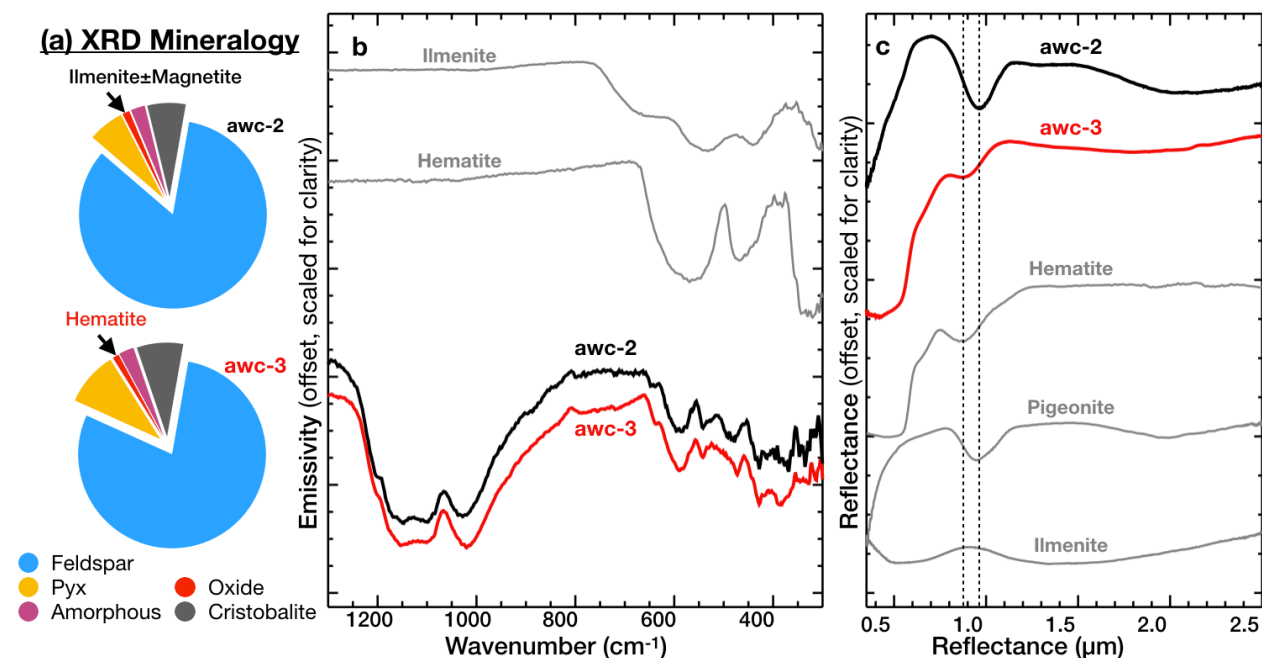


Figure 2.10. Effects of oxidation on spectral properties. (a) XRD-derived mineralogy for samples awc-2 and awc-3. Their mineralogy is nearly identical, except for the identity of their oxide minerals. (b) TIR spectra of rocks awc-2 and awc-3. awc-2 is ilmenite-bearing, whereas awc-3 contains fine-grained hematite. (c) VNIR spectra of rocks awc-2 and awc-3. The spectrum of awc-2 is dominated by pyroxene, whereas awc-3 is spectrally dominated by hematite. TIR ilmenite and hematite: ASU SpecLib (Christensen et al., 2000). VNIR Ilmenite: ILM102-lt45um-071201b, University of Winnipeg PSF. Hematite, pigeonite: USGS GDS76, HS199.1B (Kokaly et al., 2017). The lab hematite includes a significant spectrally neutral component to achieve the same spectral contrast.

X-ray amorphous material

EMPA of the glass in our samples indicates feldspar-like or more silicic compositions, often intimately mixed with oxide microphases (e.g., Figure 2.4a-c). TIR-derived amorphous chemistries for the same samples are more SiO₂-rich than EMPA estimates by 8 wt.% on average (Figure 2.8b). Conversely, models consistently underestimate wt.% CaO, Na₂O, FeO, and TiO₂ in amorphous material. These differences are likely due to both oxide/pyroxene microphase contamination in the EMPA glass measurements and mismatches with TIR library amorphous

material chemistry. Unlike igneous minerals, in which endmembers can usually be chosen along one or two-dimensional solid solution series, the large chemical and devitrification parameter space for glass is difficult to fill with a handful of endmembers. So despite using a wider range of X-ray amorphous endmembers that are able to more accurately model glass abundance than past studies, chemistry and degree of devitrification of chosen endmembers are still limiting factors in correctly estimating amorphous composition.

2.5.4 TIR Bulk Chemistry

TIR-derived bulk chemistries for most unaltered and oxidized samples are well-modeled. Figure 2.11a shows the XRF-measured versus TIR-modeled bulk rock oxide data for all XRF-measured samples. Overall, TIR model results show excellent agreement with XRF values, with individual errors < 5 wt.% and average errors ≤ 1.5 wt.%. TiO_2 is consistently underestimated by about 1 wt.%, due to the lack of modeled Ti-bearing oxide minerals discussed above, but errors induced by oxide minerals are small. Wt.% oxide error is not significantly different in the hematite-bearing samples.

Figure 2.11. Accuracy of TIR-derived bulk petrology. (a) TIR-derived major wt.% oxides compared to XRF chemistry. (b) Total alkali vs. silica diagram (LeBas et al., 1986) of all TIR models (symbol positions) compared to expected unit petrology (symbol colors) from Hildreth et al. (2012). Symbol colors that match their background are accurate models. Units intermediate between fields have mixed colors. Symbol shapes correspond to unaltered (circles), oxidized (triangles), or hydrothermally altered (squares) samples. Models notably underestimate wt.% SiO_2 in the four altered samples. (c) The subset of TIR models with corresponding XRF measurements compared to those XRF measurements. TIR models results are colored as in (b), and XRF measurements are in black.

Figure 2.11 continued

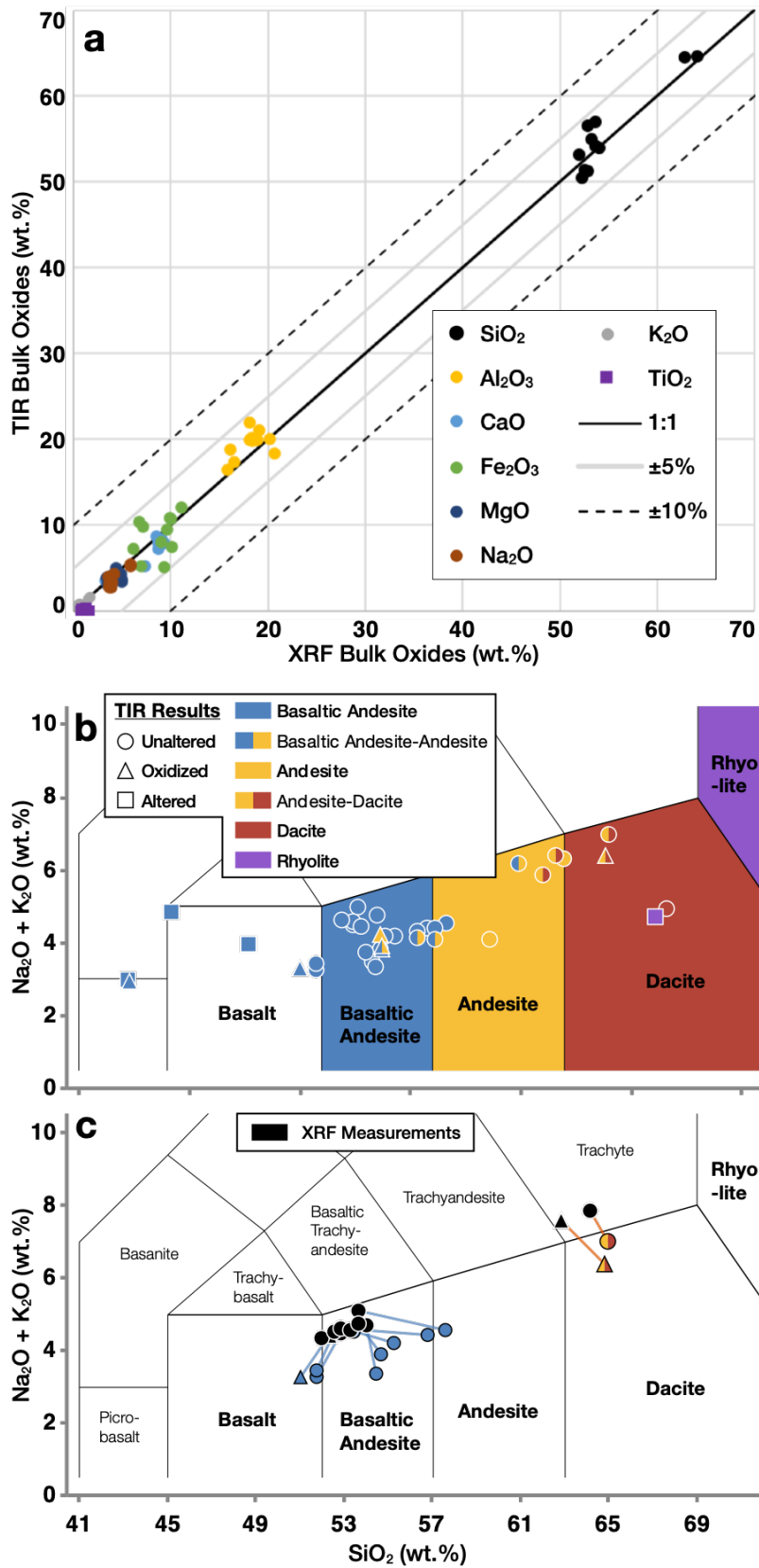


Figure 2.11b compares the TIR model chemistry for all rocks to the expected petrology of their respective geologic units on a total alkali versus silica diagram (Le Bas et al 1986; Hildreth et al., 2012). Units acc and mcl occupy the transition area between basaltic andesite and andesite, and unit awc occupies the transition area between andesite and dacite. These transitional classes are accurately reflected in the TIR-derived wt.% SiO₂. Hydrothermally altered samples tend to have lower modeled silica content than the corresponding unaltered rocks from the same unit due to higher modeled amounts of iron oxides, phyllosilicates, and low-Si glass, which is corroborated by XRD. Therefore, the plotted difference between these rocks probably reflects the precipitation of secondary phases, but could be consistent with less accurate modeling of altered vs. pristine igneous rocks (e.g., Rampe et al., 2013). The above results in rock classification from TIR spectral analyses are comparable to those of Hamilton and Christensen (2000) and Wyatt et al. (2001), are a slight improvement on their bulk oxide results (from <10 wt.% error to <5 wt.% error here), and span a wider range of iron oxide and glass content. These results indicate that by using our revised library, bulk chemistry can be accurately estimated using TIR spectral measurements to first order in glass-rich or oxidized volcanic samples.

Figure 2.11c shows TIR model chemistry compared to XRF chemistry for the subset of XRF-measured samples. Samples are always modeled within or adjacent to the appropriate field, and are modeled to within ± 5 wt.% for SiO₂. Na₂O+K₂O are underestimated in 10 of 11 samples by 0.8 wt.% on average. Compared to the glass in EMPA-measured samples, modeled amorphous Na₂O+K₂O is underestimated by about 4 wt.% on average, predominantly in Na₂O. As these samples consist of about 25 wt.% amorphous material on average, the underestimation of total alkalis in modeled amorphous material can fully explain the overall bulk difference.

2.6 VNIR Spectral Properties and Analysis

In this section, we first make mineralogical/petrological interpretations of our samples based on VNIR analysis alone (7.1), then compare to bulk mineralogy (7.2) and chemistry (7.3) to identify the origin of various spectral properties and the accuracy of standalone VNIR interpretations.

2.6.1 Mineralogy Interpreted from VNIR Spectra

Previous laboratory studies have shown that physical mixtures of Fe-bearing minerals result in systematic changes in absorption band shape and position in the VNIR (e.g., Cloutis et al., 1990a, Horgan et al., 2014; Singer 1981). Here, we employ the method of Horgan et al. (2014) for characterizing ferrous and ferric minerals and mineral mixtures (Section 4.2). The VNIR spectra were categorized into eight groups: six unaltered groups based on spectral shapes and the position of the 1 and 2 μm absorption bands (Groups 1-6), a group for oxidized spectra exhibiting strong ferric oxide signatures (Group 7), and a group for altered spectra based on strong hydration signatures (Group 8) (Figure 2.2c).

Unaltered Three Sisters VNIR spectra are consistent with complex mixtures of pyroxene, olivine, glass, plagioclase, and oxide minerals (Figure 2.2c). The most prominent feature in most unaltered spectra is a pyroxene absorption centered between ~ 0.9 - 1.0 μm . A broad second pyroxene absorption centered at ~ 2 μm is present in some of these samples (e.g., mms-7), but is weak to absent in others (e.g., acc-X; Figure 2.2c). Samples also exhibit a variable flattening, shoulder, or minimum centered around 1.3 μm that serves to modify the 1 μm pyroxene absorption (where present) by increasing the 1 μm band asymmetry and sometimes shifting the band center to slightly longer wavelengths. This behavior is caused by materials with absorptions at longer wavelengths than 1 μm such as olivine, Fe-bearing glass, and Fe-bearing plagioclase. Fe^{3+} absorptions and strong red slopes from ferric oxides between 0.2 - 0.9 μm occur in several spectra. Ferrous oxide minerals are present but not clearly detectable in the rest of the spectra, serving primarily to darken the spectra overall, and charge transfer absorptions cause a decrease in reflectance at <0.75 μm in most spectra.

Groups 1-4 all exhibit clear absorption bands near 1 μm , with variable 2 μm band strengths. These groups are differentiated based on the 1 μm band center position, strength, and asymmetry, the presence or lack of a corresponding broad band at 2 μm , and overall spectral slope. Figure 2.12a shows the calculated 1 μm band center and asymmetry for all spectral groups, and Figure 2.12b shows the calculated 1 and 2 μm band centers. Group 4 rocks are similar to Groups 1-3 but exhibit lower overall spectral contrast and reflectance, potentially due to opaque minerals like iron oxides, grain size effects, or textural effects.

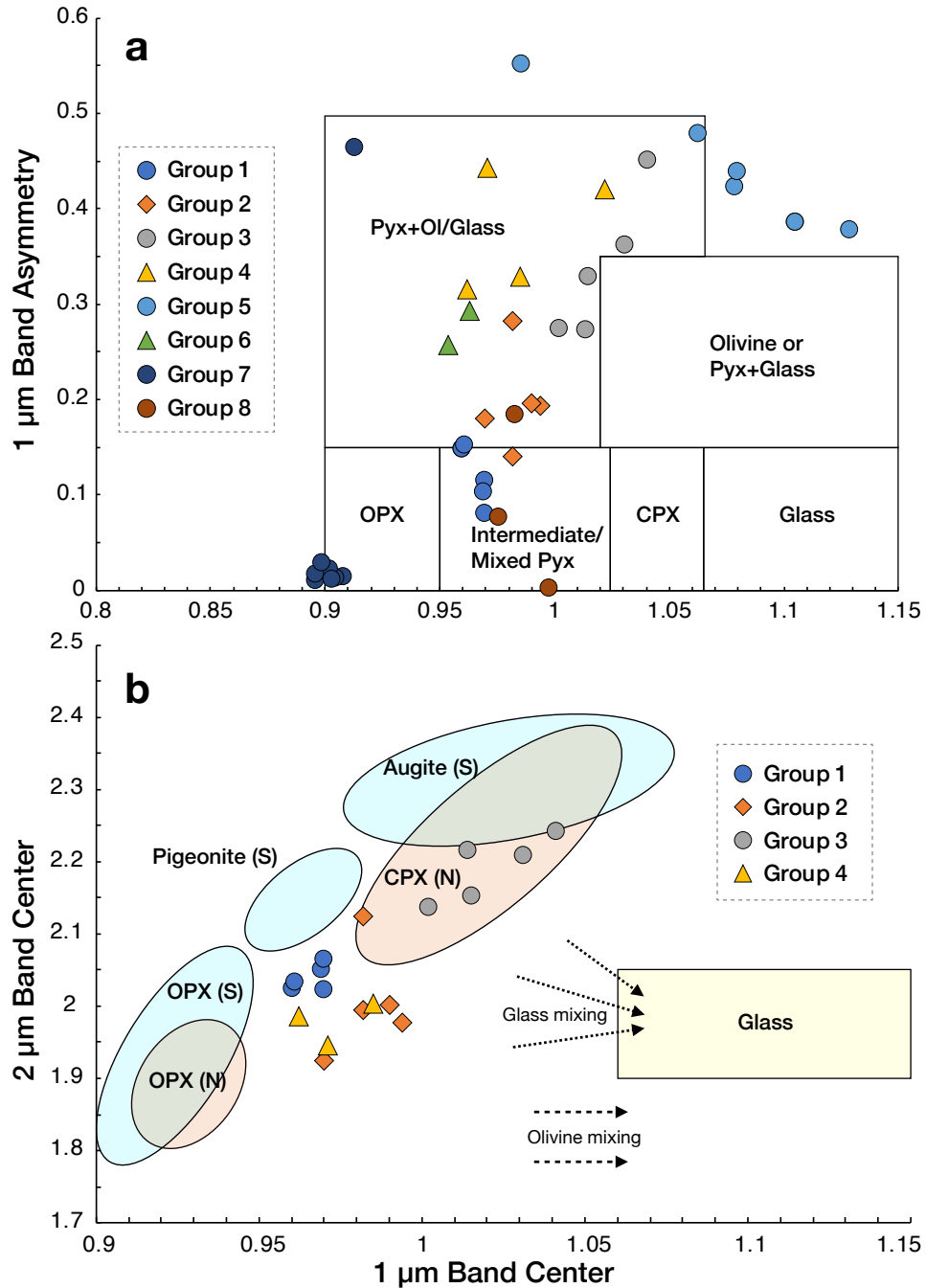


Figure 2.12. VNIR spectral parameters. (a) 1 μm band center vs. 1 μm asymmetry for all spectra from groups defined in Figure 2c, excluding two Group 6 spectra with no clear 1 μm absorption.

Plotted classification fields are characteristic parameter spaces for materials or 2-component mixtures modified from Horgan et al. (2014). (b) 1 μm vs. 2 μm band centers for all spectra that have clear 2 μm bands of over 2% depth. Orange (N) and yellow fields are for natural samples from Horgan et al. (2014), and blue fields (S) are for synthetic pyroxenes from Klima et al. (2011a). Adding olivine in mixture will draw points to the right on this plot, while adding glass will draw points towards the glass field. Group 7 hematite band centers were skewed to longer wavelengths by the continuum removal process.

Overall, Groups 1-4 are spectrally dominated by pyroxene based on the presence and position of both 1 and 2 μm bands, but the 1 μm band is modified by a shoulder of varying strengths that could be due to variable olivine, glass, or possibly plagioclase. Group 1 rocks consist of basaltic andesites and andesites (based on XRF/XRD) and exhibit strong band centers at 0.96-0.97 μm and 2.02-2.08 μm , as well as a flattening or local minimum between these bands centered at $\sim 1.29 \mu\text{m}$. Group 2 rocks are basaltic andesites that show 0.97-0.99 μm band centers, a weak 2 μm band centered between 1.93-2.11 μm , a local minimum near 1.33 μm , and are typically somewhat blue-sloped. Groups 1 and 2 plot in or close to the intermediate/mixed pyroxene field in Figure 2.12a and are consistent with pyroxene-dominated spectra. Group 3 rocks are also basaltic andesites, but with strong 1.00-1.04 and 2.00-2.25 μm band centers as well as a strong shoulder near 1.3 μm and an overall red slope. This group plots in the pyroxene + olivine/glass field due to higher 1 μm band asymmetry related to the strong 1 μm shoulder, which suggests more contribution from olivine, glass, and/or Fe-bearing plagioclase than in Groups 1-2. Group 4 rocks span basaltic andesite through dacite and exhibit weak 0.96-1.02 μm band centers, a weak or absent 2 μm band center near 1.93 μm , and a weak to intermediate shoulder near 1.3 μm with an overall spectral red slope.

Groups 1-4 exhibit 1 and 2 μm bands that together can be used to estimate pyroxene composition. Previous studies of OPX-CPX and OPX-olivine mixtures have shown that 1 μm band centers remain spectrally dominated by OPX even when it makes up only 25-40% of the Fe-bearing minerals, maintaining a band center at $< 0.95 \mu\text{m}$ (Cloutis and Gaffey, 1991b; Horgan et al., 2014). All of our unaltered spectra have 1 μm band centers consistently $> 0.95 \mu\text{m}$, suggesting that OPX is not the volumetrically dominant pyroxene in our rocks. The clear increase in the 1 μm band center between Group 1 and Group 3 also corresponds to a general increase in 2 μm band center, which together can be attributed to increasing Ca-content in pyroxene (Figure 2.12b). Group 1 plots between OPX and augite fields and is most spectrally similar to pigeonite (Klima et al., 2011a) or OPX/high-Ca CPX mixtures (Cloutis and Gaffey, 1991b; Horgan et al., 2014). Group 3 is more variable, but mostly consistent with CPX.

Groups 2 and 4 have 1 μm band centers that are longer wavelength than expected and diverge from the OPX and CPX fields in Figure 2.12b. This divergence is consistent with mixing with either glass or olivine. Glass is distinguishable from other Fe-bearing minerals by its long-wavelength 1 μm band and its short-wavelength 2 μm band. If glass is causing the shift in bands

in Groups 2 and 4, this would imply a glass-rich composition, as pyroxene-glass mixtures have been shown to plot near the OPX/CPX fields until > 50-70% glass abundance, and only exhibit glass-like band centers and asymmetries at > 80-95% glass (Horgan et al., 2014). Olivine could also shift the 1 μm band center to longer wavelengths without modifying the 2 μm position (Cloutis and Gaffey, 1991a; Horgan et al., 2014). Based on the spectra alone, it is unclear whether glass or olivine is shifting the band centers in Groups 2 and 4.

The shoulder on the 1 μm band at 1.3 μm observed in Groups 1-4 is also consistent with glass, olivine, or possible Fe-rich plagioclase, and is responsible for their elevated 1 μm band asymmetries. The elevated 1 μm band asymmetry is associated with longer wavelength 1 μm band centers (Figure 2.12a). This effect is consistent with olivine or glass mixing (Figure 2.12b) but not consistent with Fe-bearing plagioclase, because feldspar mixing does not typically affect the position of the 1 μm band (Cheek and Pieters, 2014). A 1.2 μm absorption in pyroxene due to excess iron in the M1 crystallographic site (Klima et al., 2008) is also a possible contributor; however, its effect on mixture spectra is understudied (Cheek and Pieters, 2014). Because olivine and glass are the most likely significant contributors, and the strength of the shoulder is typically correlated with the amount of olivine/glass (Horgan et al., 2014), samples with high asymmetry in Groups 3 and 4 are predicted to include significant olivine or glass. Although Groups 1 and 2 plot with relatively low asymmetries within the range defined by OPX-CPX mixtures, their non-zero asymmetry is caused by a flattening or minimum near 1.3 μm and is still likely indicative of additional phases such as high abundances of Fe-bearing plagioclase (Cheek et al., 2013; Serventi et al., 2013; Serventi et al., 2016).

Group 5 rocks are predominantly basaltic andesite and exhibit more red-sloped, somewhat concave-up spectra and a shoulder or weak square-shaped band centered at $\sim 0.97\text{-}1.06$ μm with a nearly equally strong and broad 1.3 μm absorption, and no apparent 2 μm absorption. Based on the typically longer wavelength ~ 1 μm band centers, strong 1.3 μm shoulder, and total lack of 2 μm band, this group is unusual but more consistent with olivine-rich spectra. However, most of this group plots outside the typical fields in Figure 2.12a.

Group 6 rocks are fine-grained basaltic andesite to andesite and exhibit spectra that are strongly concave-up, blue-sloped, and nearly spectrally featureless, apart from a weak 0.95-0.96 μm pyroxene absorption in the andesitic members. Specific mafic minerals cannot be identified in the featureless spectra. The overall characteristics of these spectra (e.g., strong blue slope, concave

up shape, and lack of absorption bands) are similar to those of spectra of aphanitic or microcrystalline basalts due to small grain sizes of individual crystals (Carli and Sgavetti, 2011; Carli et al., 2015; Henderson et al., 2020).

Each of the unaltered groups also exhibit continuum slopes: Groups 1, 2, and 6 have blue slopes, and Groups 3, 4, and 5 have red slopes. Fine particles on the order of the wavelength of the light can cause spectral bluing depending on the grain size distribution and optical properties of the material (Brown, 2014). As our spectra are of crushed $< 125\ \mu\text{m}$ grains, that effect is likely at work here. Conversely, Fe-bearing glasses tend to exhibit a red slope, which is stronger in more oxidized or Fe-rich samples (Bell et al., 1976; Cannon et al., 2017, Carli et al., 2016).

Group 7 spectra are visibly oxidized basaltic andesite and andesite dominated by red crystalline fine-grained hematite, based on a strong absorption centered at $0.87\text{--}0.90\ \mu\text{m}$ and a characteristic shoulder near $0.6\ \mu\text{m}$ (Morris et al., 1985). Some Group 7 spectra also exhibit weak 1.41 and $1.91\ \mu\text{m}$ OH/H₂O hydration bands, and $2.31\ \mu\text{m}$ absorptions possibly due to minor Fe-Mg smectites.

Group 8 rocks are altered basaltic andesite and rhyolitic pumice, and display a broad absorption centered at $0.97\text{--}1.00\ \mu\text{m}$ attributable to pyroxene or iron in alteration phases, as well as hydration bands at $1.41\text{--}1.42$, 1.46 , and $1.91\ \mu\text{m}$. The samples mns-Ash and mns-G display an additional band at $2.30\ \mu\text{m}$ and a very weak band at $2.39\ \mu\text{m}$ indicative of Fe/Mg smectite clay minerals (Bishop et al., 2008). Sample roc-1 displays a broad, rounded, asymmetric absorption at $2.21\ \mu\text{m}$ consistent with hydrated silica or hydrated volcanic glass (Rice et al., 2013; Swayze et al., 2007).

2.6.2 Comparison of VNIR with Quantitative Mineralogy

Overall, we observe only modest correlation between VNIR spectra and the corresponding modal mineralogy derived with XRD. While plagioclase is by far the most volumetrically abundant mineral in our samples, it is not detectable in our VNIR spectra. Compared to mafic silicates and Fe-oxides, plagioclase is a weak absorber in the VNIR (Cheek et al., 2014; Crown and Pieters, 1987; Serventi et al., 2016). Glass more strongly modifies spectra than plagioclase, but its absorptions may still be overwhelmed by mafic silicates (Horgan et al., 2014). Correspondingly, pyroxene and (to a lesser extent) olivine are the dominant phases in most of our

spectra despite their collective abundance at <21 wt.% in all rocks, while plagioclase, and glass (together at >53 wt.%) primarily serve as secondary modifiers to the pyroxene/olivine absorptions.

Percent band depth does not always strongly correlate with corresponding mineral abundance. For example, Figure 2.13a-b shows 1 and 2 μm band depths versus XRD-derived total pyroxene abundance in unaltered samples. Although the 1 μm band depth shows a weak possible positive correlation ($R^2=0.13$) with pyroxene abundance, bands of similar depths span an order of magnitude in pyroxene abundance and are therefore not precise enough to be a useful indicator of pyroxene content. 1 μm absorptions in Groups 5 and 6 are absent or far weaker than in Group 3, despite similar pyroxene contents of 5-10 wt.%. There is no apparent correlation between the 2 μm band depth and pyroxene abundance in any group, and several pyroxene-bearing samples (up to 10 wt.%) lack 2 μm bands altogether.

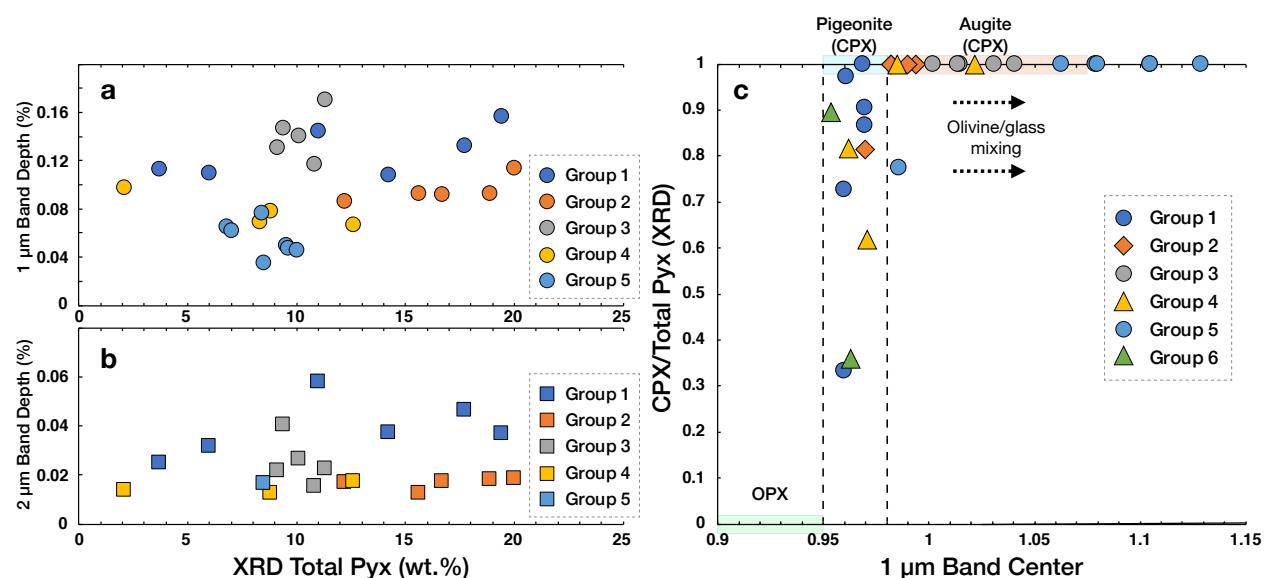


Figure 2.13. Relationship between pyroxene content and 1 and 2 μm absorptions. (a) 1 μm band depth and (b) 2 μm band depth versus XRD pyroxene abundance for Groups 1-5. Little useful correlation occurs between band depth and pyroxene abundance. Even less correlation is observed if band depth or band area are plotted against XRD pyroxene + olivine abundance. (c) 1 μm band center versus XRD-derived CPX/(Total Pyx) ratio for unaltered spectra (Groups 1-6). Band centers between 0.95-0.98 μm can be indicative of a wide range of OPX-CPX mixtures, from majority OPX to 100% CPX. Mixing with olivine and/or glass further complicate interpretation by drawing points to the right.

In a given spectrum, the relative contributions of olivine and glass to the 1.3 μm shoulder are difficult to differentiate. Figure 2.14 shows that this feature can be spectrally similar in two

mineralogically distinct rocks. XRD shows this shoulder is likely due to glass in the dacite dbh-1 (Group 4), whereas the shoulder is more likely due to olivine in the relatively glass-poor and olivine-rich basaltic andesite mms-2 (Group 3). The dbh-1 dacite is the most glass-rich (55 wt.% from XRD) unaltered sample, and while the glass absorption is visible, it cannot be confidently differentiated from olivine based on band center and asymmetry alone. The cause of the 1.3 μm shoulder is even more difficult to distinguish in spectra where the shoulder is weak, such as in olivine-free Group 1 spectra and weakly olivine-bearing Group 2 spectra. This is in agreement with our 1 and 2 μm band parameter results and past studies showing that glass is only consistently uniquely detectable at higher abundances (Horgan et al., 2014). Instead, our spectrally red-sloped samples are generally more glass-rich, suggesting glass content affects spectral slope in igneous glass-mineral mixtures.

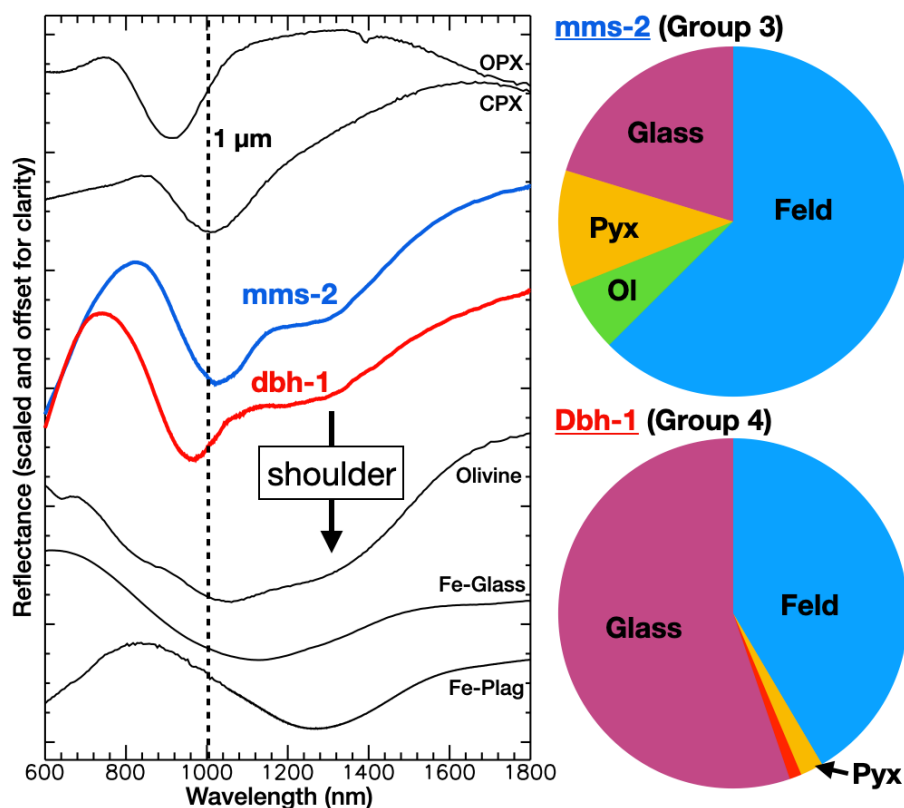


Figure 2.14. Spectral similarity between a basaltic andesite and dacite with highly dissimilar bulk and mafic mineralogy. VNIR spectra of a basaltic andesite (mms-2) and dacite (dbh-1) compared with laboratory mineral spectra and bulk mineralogy. Despite distinct mineralogy, the main observable difference is 1 μm band center corresponding to CPX in mms-2 and OPX in dbh-1. mms-2 also has a weak 2 μm band not shown. OPX, CPX, Olivine: USGS NMNH128288, NMNH120049, NMNH137044 (Kokaly et al., 2017). Fe-Glass, Fe-Plagioclase: See Figure 2.2.

A very long wavelength 1 μm band center ($>1.08 \mu\text{m}$) is a more unique indicator of glass. However, while previous studies have shown that these long wavelength band centers can indicate high glass abundances ($>60\text{-}80 \text{ wt. } \%$) (Cannon et al., 2017; Horgan et al., 2014), our results show that it can also indicate moderate glass abundances ($>25 \text{ wt. } \%$) mixed with olivine. The effects of olivine, Fe-bearing plagioclase, glass, and pyroxene on 1 μm band center and asymmetry in our unaltered rocks are shown in Figure 2.15. Both band center and asymmetry are positively correlated with olivine and glass abundance, and band centers beyond $\sim 1.08 \mu\text{m}$ can likely be attributed to the influence of high abundances of Fe-bearing glass relative to olivine/pyroxene in those samples. However, we also confirm that moderate abundances of glass ($<40\text{-}60\%$) cannot alone overcome the influence of pyroxene on band center. 1 μm band centers $>1 \mu\text{m}$ only occur in rocks that also contain olivine, even in samples with glass abundances of $40\text{-}60 \text{ wt. } \%$. The glass in our samples does cause a significant increase in asymmetry, but does not strongly change the 1 μm band center at such abundances, consistent with previous studies of glass/pyroxene mixtures (Horgan et al., 2014). Olivine-poor rocks exhibit band centers $<1 \mu\text{m}$ consistent with OPX-CPX mixtures, so pyroxene composition rather than abundance of pyroxene, plagioclase, or glass is controlling the 1 μm band center in olivine-poor rocks.

Neither pyroxene nor plagioclase appears to have a major effect on the asymmetry of the 1 μm band (Figure 2.15). Plagioclase abundance does not show a clear trend with either band center or asymmetry, and pyroxene abundance is weakly anticorrelated with asymmetry. However, olivine-free, glass-poor rocks still exhibit asymmetries of $>\sim 0.1$, suggesting that either iron in plagioclase or in the M1 crystallographic site in rapidly cooled pyroxene (Klima et al., 2008) provides a relatively constant, small increase in asymmetry.

Natural mixtures of varying abundances of olivine, pyroxene, and glass can create highly similar spectra that are not easily differentiated by standard spectral analysis techniques. For example, samples in Groups 2 and 4 exhibit similar 1 and 2 μm absorption band depths and centers consistent with a mixture of OPX, CPX, and either glass or olivine (Figure 2.12). In fact, XRD indicates that these samples are variable mixtures of OPX, CPX, glass, and minor olivine, with OPX present in only three of seven samples and olivine in six of seven. Thus, even though all of these samples exhibit relatively short 2 μm band centers that would typically be interpreted as due to OPX, the majority of samples do not contain OPX. Instead, the lower 2 μm band center in the

OPX-free samples is likely due to glass. However, this would be difficult to determine based on the spectra alone.

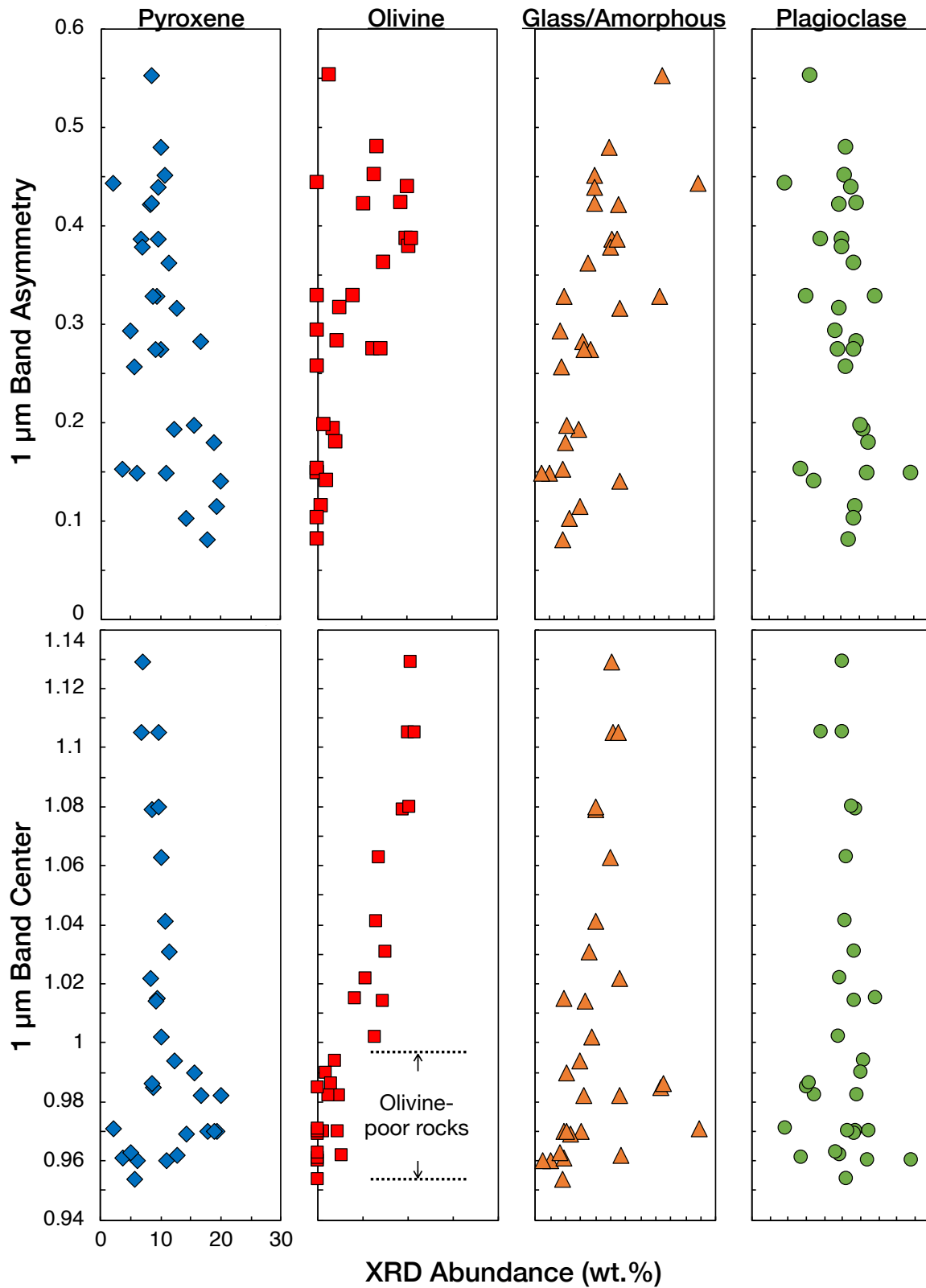


Figure 2.15. Trends of XRD abundances of pyroxene (blue diamonds), olivine (red squares), amorphous (orange triangles), and plagioclase (green circles) compared to 1 μm band asymmetry and band center.

Group 7 rocks have XRD modal mineralogy comparable to unaltered rocks from the same unit with the addition of trace (<2 wt.%) hematite. Despite the presence of pyroxene and glass +/- olivine in these samples, Group 7 spectra are spectrally dominated by this small amount of hematite in VNIR (Figure 2.10). EMPA indicates that there is not additional hematite present in oxide grains >5 μm in size in Group 7 samples compared to other samples lacking VNIR hematite absorptions. Therefore, Group 7 VNIR hematite absorptions are likely due to minor micro- or nanophase hematite present as grains <1 μm , the smallest spot size used in our EMPA analyses, and were not detected. Because a well-defined 0.86 μm hematite absorption only occurs for particles >10 nm (Morris et al., 1989), we can constrain the hematite particle size to between 10 nm and 1 μm . This minor hematite is volumetrically distributed and serves to obscure the mafic minerals as a strong absorber (e.g., Straub et al., 1991). So, the bulk iron mineralogy of Group 7 rocks is not predictable by their VNIR spectra, and may be misinterpreted altogether as hematite-rich rocks.

Some spectra, especially in Groups 5 and 6, exhibit a minor absorption centered near 0.5-0.6 μm (Figure 2.4e). This absorption is similar to the 0.6 μm absorption found in lunar melt breccias and impact melt glass (Adams et al., 1974; Tompkins and Pieters, 2010), which was attributed to microcrystalline ilmenite in a transparent matrix. This is a special case where normally opaque ilmenite is fine-grained enough to allow selective absorption, creating a 0.6 μm feature and strongly lowering the overall reflectance. Although all of our samples are ilmenite-bearing to some degree, it mostly occurs as larger opaque groundmass crystals and microphenocrysts that lower the overall reflectance without introducing a 0.6 μm band. Samples from Groups 5 and 6 have a more fine-grained matrix than other samples, where microcrystalline ilmenite is more likely to occur. This absorption is discussed in Section 8.3.

Similar to the hematite-bearing samples, altered rocks (Group 8) are spectrally dominated by minor phases. Fe-Mg smectites dominate two of the sample spectra at 4-5 wt.%, and hydrated silica and/or glass dominates the third. XRD modal mineralogies of the smectite-bearing samples are otherwise similar to unaltered rocks from the same unit, but risk misinterpretation as smectite-rich rocks based on the spectra alone.

2.6.3 Comparison of VNIR with Mineral Chemistry

In our rocks, absorption band overlap prevents confident interpretation of plagioclase, olivine, or glass chemistry. The 1 and 2 μm pyroxene absorptions, on the other hand, are spectrally distinct and shift towards longer wavelengths with increasing calcium content (Cloutis and Gaffey, 1991b; Klima et al., 2011a). Past work on natural and synthetic pyroxenes suggests that 1 μm band centers typically range between about 0.90-0.95 μm for OPX, 0.95-0.98 for pigeonite CPX, and 0.98-1.06 for augite CPX, with mixtures falling in between these endmembers (Horgan et al., 2014; Klima et al., 2011a). Figure 2.13c shows the effect of the ratio of XRD-derived CPX/(Total Pyx) versus 1 μm band center in our samples. For our samples with band centers above ~ 0.98 μm , pyroxene occurs exclusively as a CPX (augite \pm pigeonite) as expected. Band centers between 0.95-0.98 μm should indicate either pigeonite or a mixture of OPX and CPX. Indeed, XRD results indicate that this subset of samples includes both CPX-dominated rocks (~ 80 -100% CPX; most likely pigeonite-bearing) and rocks with significant OPX (Figure 2.13c). So, the 0.95-0.98 μm band centers in these samples are variously due to pigeonite and/or some OPX-CPX mixture. Without the additional chemistry and proportions imposed by EMPA and XRD, distinguishing an OPX-CPX mixture from pure pigeonite is challenging based on band centers alone. Olivine and glass in each sample further complicate pyroxene identification by serving to shift the 1 μm band center to longer wavelengths by an unknown amount.

One potential spectroscopic indicator of an OPX/CPX mixture would be spectral broadening of the 1 and 2 μm bands, which can occur in physical mixtures, exsolution lamellae, or zoning of CPX and OPX (Cloutis and Gaffey 1991b; Sunshine and Pieters, 1993). However, in our samples, pyroxene absorptions do not appear to be obviously broadened or contain two components. Any possible broadening is also not necessarily attributable to pyroxene, as broadening can also occur in the 1 μm band due to olivine, plagioclase, and glass, and in the 2 μm band due to glass. Although more sophisticated deconvolution techniques such as the Modified Gaussian Model (Sunshine et al., 1990) yield accurate identification and abundance estimates of pyroxenes in two-component mixtures (Kanner et al., 2007; Sunshine and Pieters, 1993), it is yet unclear whether these techniques are feasible in ternary or more complicated natural igneous mixtures (Clenet et al., 2011).

2.7 Discussion

2.7.1 Interpretability of Petrologic Information from TIR Spectra

Our results confirm previous studies that demonstrated TIR models can accurately reproduce bulk mineralogical and chemical composition. With our samples and an improved endmember spectral library, we successfully reproduce modal mineralogy to within 10-15 wt.% for all mineral groups (Figure 2.3). These results are similar to successful models of crystalline mineralogy reported in previous studies (Feely and Christensen, 1999; Hamilton and Christensen, 2000; Wyatt et al., 2001), but we are also able to reproduce amorphous abundances within this tolerance. We slightly improve on bulk oxide chemistry relative to the 10% reported in previous studies (Wyatt et al., 2001), successfully estimating all wt.% oxides to within 5% for our 11 XRF-measured samples, perhaps due to improved models of the amorphous component (Figure 2.11a).

TIR models also have some success identifying minor phases. Several minor mineral groups (OPX, phosphate, zeolite, oxides, and phyllosilicates) were identified at around the < 5-10 wt.% level in XRD results, placing their abundances at or below the typical 5-10% TIR detection limit (Feely and Christensen, 1999). In general, TIR-derived abundances that are lower than the detection limit are not considered confirmed detections. For our samples, minerals modeled at minor abundances (< ~5 vol.%) in our TIR spectra are typically not detected by XRD. However, it is rare for minor minerals identified by XRD to be absent in corresponding TIR models. Therefore, even below the detection limit, it appears that if a mineral is present both in the rock and in the spectral library, it is likely to be included in TIR models. Furthermore, TIR models never predict > 10 vol.% abundance of endmember groups that are not corroborated by XRD.

The phyllosilicate group in particular is never falsely modeled where it does not occur, exhibiting a tight fit with XRD results below 5 wt.%. This is surprising as some previous studies have found that phyllosilicates are overestimated in weathered rocks and sediment (e.g., Rampe et al., 2013). Lack of accurate glass endmembers can lead to phyllosilicate overestimation because glass and phyllosilicates have similar spectral shapes and Si-O band positions (Koeppen and Hamilton, 2005; Michalski et al., 2005), so the relative success here could be due to the inclusion of more diverse glass endmembers. Our improved models of phyllosilicates could also be due to good compositional and structural matches between library and sample phyllosilicates. The phyllosilicates occur in the rock matrix of our samples rather than as coatings or rinds and undergo

grinding and pellet sample preparation, both of which would lead to more even volume distribution and more ideal measurement conditions compared to surficially weathered rock samples. Under such conditions, it may be possible for phyllosilicates to be more accurately modeled at low abundances in TIR.

Our models of amorphous materials in our samples are significantly improved compared to previous studies because our TIR endmember library greatly broadens the number, textural variability, and chemical variability of amorphous and glassy compositional endmembers. Using this library, we are able to accurately derive amorphous abundances at up to 55 wt.% with approximately the same level of error as other major mineral groups (\pm 10-15 wt.%; Feely and Christensen, 1999). This result was confirmed in a related study by Henderson et al. (2020), who performed laboratory TIR models of a variety of natural volcanic tephra samples and synthetic glass-mineral mixtures containing 20-100 wt.% glass using a similar spectral endmember library. Their study found that glass estimates largely agreed with XRD models to within 15 wt.% throughout the range. So, future studies that use an appropriate number and variety of amorphous endmembers (both in chemistry and devitrification state) in deconvolutions of unaltered volcanic rocks and sediments should produce reasonable abundance estimates for glassy samples.

It remains challenging to determine the exact nature of the amorphous material in a sample using TIR spectroscopy. Our TIR models typically selected both primary volcanic glass and secondary amorphous (e.g., allophane, opal) endmembers. On average, 55% of the total amorphous material in each sample is modeled as volcanic glass, and 45% is modeled as amorphous aluminosilicates, including allophane, aluminosilicate gel, and aluminous opal. However, our unaltered samples should contain only volcanic glass and no high-silica alteration-related phases. We interpret this result as indicating that amorphous aluminosilicates are substituting for glass in the models. The Si-O absorptions of both classes of amorphous material exhibit similar broad, U- to V-shaped absorption bands that shift based on silica content (Michalski et al., 2006; Ruff and Christensen, 2007), and so we hypothesize that the model chooses the best match in terms of band center and shape from these two groups. Nevertheless, error in TIR-derived amorphous wt.% SiO₂ appears to decrease with increasing XRD amorphous abundance, to less than 5 wt.% error at 40 wt.% XRD amorphous abundance (Figure 2.8b). This trend most likely occurs because the position of the Si-O absorption in amorphous material is related to wt.% SiO₂, and more strongly influences the overall spectrum with increasing abundance.

The inclusion of improbable secondary amorphous materials in our TIR models may occur either because TIR models are not able to accurately distinguish between glass and other amorphous phases (e.g., Minitti and Hamilton, 2010), or because our library is still missing appropriate glass endmembers. Given that the substituted endmembers for our samples are high-silica amorphous materials, the missing endmembers probably include high-silica aluminosilicate glasses, perhaps of variable crystallinity. In support of this hypothesis, EMPA measurements suggest that high-silica (e.g., feldspar composition) glasses are common in our samples, and this type of glass is not appropriately represented in existing TIR endmembers. Spectral measurements of new, compositionally distinct glass endmembers is necessary, not only to fill out a successful endmember library, but also to fill in current knowledge gaps on the relationship between spectral properties and the wide chemical and devitrification parameter space possible in glasses.

We find that TIR models are more successful at reproducing the details of mineral chemistry for some materials than for others. We have been able to more accurately assess TIR mineral chemistries for a wider range of minerals than previous studies, as chemistries of all major mineral phenocrysts and groundmass crystals were measured directly using EMPA, and average mineral chemistries were calculated from Rietveld refinements. This allows confidence in our average plagioclase chemistry results of <10-15 An# error, similar to previous studies (Wyatt et al., 2001). We also directly confirm a “sodic bias” of the average toward groundmass compositions that was first investigated in Milam et al. (2004). Olivine is significantly overestimated both in abundance and iron content in our samples, especially the andesites and dacites that do not contain olivine. Notably, no significant difference in mineral composition error arose between the unaltered and oxidized (hematite-bearing) rocks. However, plagioclase chemistry estimates and rock classifications were not as successful for samples that were both altered and glassy, consistent with past studies noting difficulties in TIR modeling of weathered basalt (Rampe et al., 2013).

The TIR endmember library does not accurately model alkali feldspar chemistry in our samples (Figure 2.5). Alkali feldspar undergoes changes in crystal symmetry with changing chemistry (e.g., triclinic anorthoclase to monoclinic sanidine at Or₃₇), and changes in unit-cell volume with temperature (e.g., high vs. low albite), which are likely to change the shape and position of TIR absorption bands. Unlike olivine (Hamilton, 2010) and plagioclase (Milam et al., 2004), it is likely that a sample’s alkali feldspar chemistry may not be easily interpolated between endmembers of differing structure due to these additional effects.

Similarly, pyroxene chemistry is not well-modeled (Figure 2.6). One possible reason for this discrepancy is that the TIR library pyroxenes are largely compositionally distinct from those found by EMPA, especially for augite, in part because those pyroxene endmembers are sourced from plutonic rocks that equilibrated at lower temperatures and thus different chemistries (Lindsley, 1983; Wyatt et al., 2001), as well as from differences arising in crystal symmetry in OPX and CPX. This problem has been known for some time (e.g., Hamilton and Christensen, 2000; Hamilton et al., 1997; Dunn et al., 2007; Wyatt et al., 2001). In our rocks, it may have also contributed to the observed 4 wt.% CPX abundance underestimation.

One potential mitigation strategy for the above would be to measure a wider compositional and temperature range of alkali feldspar, augite, pigeonite, and orthopyroxene endmembers. In particular, it is clear that more publicly available high-T, intermediate composition CPX endmember spectra (e.g., Glotch et al., 2019) are critically required for accurate modeling of extrusive igneous rocks, which are abundant on extraterrestrial bodies. For example, ChemCam data from MSL indicate anorthoclase and pigeonite grains at Gale Crater (Payré et al., 2020), which would likely be poorly modeled if measured by a TIR instrument. A step-wise modeling procedure could initially use a full range of endmembers in a compositionally broad library, then constrain the library to only include the most likely feldspar and pyroxene phases based on the output of the model.

We hypothesize that overestimation of Fe-rich olivine in our TIR models is due to overlap between fayalite absorption bands and well-known transparency features due to fine grains in our samples. At particle sizes below about 60-80 μm , substantial volume scattering in the TIR wavelength region introduces a “transparency” feature that usually occurs on the long-wavelength side of the Si-O fundamental absorption in silicates (e.g., Hamilton, 1999; Salisbury and Wald, 1992). Before wet-sieving to 125-250 μm , all sample spectra showed a broad transparency feature between 700-1100 cm^{-1} (Hamilton, 1999; Ruff and Christensen, 2002) that shifted to longer wavenumbers in more silicic samples (Shirley and Glotch, 2019). Overwhelmingly, the effect of this transparency feature on model results is to produce significant overestimation of fayalitic olivine abundance (Figure 2.9). Compared to other minerals and glasses in the endmember library, the Si-O complex in fayalitic olivine is located closest to the $\sim 900 \text{ cm}^{-1}$ transparency feature center and is therefore chosen by the model, resulting in consistent underestimation of olivine Fo# and erroneously predicting olivine in the andesites and dacites. After wet-sieving, this absorption

largely disappeared, but continued Fe-rich olivine overestimation suggests some minor clinging fines were still present.

2.7.2 Interpretability of Petrologic Information from VNIR Spectra

The results from this study confirm that petrologic interpretations from common VNIR spectral analyses of natural igneous rocks are often unreliable. In monomineralic or two-component mixtures of common igneous minerals and glass, VNIR spectra exhibit characteristic and interpretable absorption band mixing trends that can be used to infer bulk mineralogy (e.g., Cheek and Pieters, 2014; Cheek et al., 2013; Crown and Pieters, 1987; Horgan et al., 2014; Serventi et al., 2013; Singer, 1981). However, we find that spectral ambiguity is much greater in natural volcanic rocks, which are multi-component mixtures of ferrous and non-ferrous minerals and glass with additional textural effects. This ambiguity has the potential to seriously confuse petrologic interpretations based on VNIR spectra alone.

Olivine can be a key indicator of mafic rock compositions, but can potentially be misidentified from VNIR spectra of pyroxene mixed with Fe-bearing glass (and in the extreme case, Fe-bearing plagioclase). We find that moderate amounts of weakly absorbing volcanic glass are spectrally similar to low amounts of olivine, as both impart a 1.3 μm shoulder in the presence of a 1 μm pyroxene absorption. In mafic mineral-poor rocks such as anorthosite, abundant plagioclase mixed with minor pyroxene (e.g., 85%/15%; Cheek et al., 2013) can also produce asymmetric spectral shoulders highly similar to those formed by olivine and/or glass in our Group 3 spectra. This potential for ambiguity and corresponding misidentification of olivine has only been occasionally cautioned in the literature (e.g., Horgan et al., 2014), yet greatly reduces the utility of VNIR as a petrologic tool in rocks with pyroxene-dominated spectra, which include large portions of the martian and lunar surfaces (Klima et al., 2011b; Mustard et al. 2005).

More generally, VNIR spectral properties often only have a loose relationship with bulk mineral abundances in our volcanic rocks. Pyroxene, especially OPX, often dominates VNIR spectra even at very low abundances (e.g., Figure 2.14), so simple spectral analyses like changes in relative band depth should not be relied upon as indicators of pyroxene abundance. This is in part because glass and plagioclase, and to a lesser extent olivine, are easily overwhelmed by pyroxene absorptions. Despite high abundance and iron content great enough to exhibit a minor 1.25 μm absorption in the absence of other minerals, the plagioclase in our samples is not

identifiable through either manual spectral interpretation or common spectral parameters. Glass is identifiable in some samples at moderate abundances (>30%), but only where olivine is also present to help dilute the pyroxene signal. However, this difficulty in detecting glass and plagioclase in particular means that when they are clearly detected on a planetary surface, this has major implications for the nature of the rocks. Clear VNIR detections of glass imply abundances (>60-80% of mafic minerals) consistent with explosive volcanic processes (Horgan and Bell, 2012) or impact melt (Cannon et al., 2015), and clear plagioclase signatures may imply abundances typical of cumulates or plutons (Cheek and Pieters, 2014).

VNIR spectral interpretation for petrologic applications may only be partially improved by more advanced modeling techniques. Available methods meant to circumvent difficulties in manual or parameter-based spectral interpretation include the Modified Gaussian Model (MGM; Sunshine et al., 1990) and linear or nonlinear VNIR spectral unmixing (e.g., Poulet et al., 2009; Liu et al., 2016; Riu et al., 2019). The MGM uses modified Gaussian curves to fit and model absorption bands of geologic materials based on an understanding of the underlying processes that cause band shapes (Sunshine et al., 1990). This method has had success in recovering pyroxene composition and modal abundances in 2-component mixtures (Sunshine et al., 1993) and martian surface spectra (Kanner et al., 2007) and in the future could be applied to mixtures containing pyroxenes with 1.2 μm M1 bands. More recently, the MGM was applied to olivine-pyroxene mixtures successfully in the lab and in OMEGA spectra over Syrtis Major on Mars (Clenet et al., 2011; 2013). However, Clenet et al. (2011, 2013) found that increasing mixture complexity, including ternary mixtures and mixtures containing plagioclase, presented decreased success in accurate modeling. MGM modeling of natural igneous mixtures that contain glass and oxide minerals has not been successfully demonstrated to date. VNIR spectral unmixing typically relies on the radiative transfer theories of Hapke (1981) or Shkuratov et al. (1999) by converting reflectance data into linearly unmixable variables (e.g., single-scattering albedo), then applying a deconvolution method such as the spectral mixture analysis (*sma*) code used in this study along with a library of endmember spectra in the form of wavelength-dependent optical constants. VNIR spectral unmixing has been successfully applied to both local studies (e.g., Liu et al., 2016) and ambitious regional to global studies on Mars (e.g., Poulet et al., 2009; Riu et al., 2019). However, accurate abundance estimates can be degraded by common spectrally bland phases (e.g., plagioclase, quartz). Because the wavelength-dependent optical constants required for library

endmembers are not trivial to derive (e.g., Sklute et al., 2015), a robust and appropriate library can be difficult to build. Results from these models are also inherently limited by the assumptions of the theory and model (e.g., particulate surface, shadowing constraints, scattering assumptions; Hapke, 1981; Skhuratov et al., 1999). Despite these drawbacks, it is possible that this modeling approach could perform better than the spectral parameters used here at differentiating the source(s) of the 1.3 μm absorption in our samples due to its minimization approach that uses the full spectrum rather than specific derived parameters. However, this kind of automated, numerical approach is also highly susceptible to microtextural effects discussed below, which can cause major spectral variability independent of mineral abundances.

2.7.3 Effects of Rock Microtexture on VNIR Spectra

We hypothesize that rock microtexture is the root cause of concavity and reduced spectral contrast observed in many of our VNIR spectra. Our VNIR Groups 5 and 6 exhibited suppressed mafic mineral absorptions and concave-up spectra (Figure 2.2c; Figure 2.13a-b), and similarly suppressed absorption features are common in fine-grained basalts. Three previously proposed explanations for suppressed features include: (1) abundant opaque oxide minerals, (2) an optical coupling mechanism wherein particles larger than the grain size of individual minerals (i.e., multimineralic grains) exhibit reduced band depths, and (3) a large number of Fe-bearing minerals in a rock (Carli and Sgavetti, 2011; Carli et al., 2015). In our samples, overall oxide mineral abundance is relatively low, and grain size distribution and number of Fe-bearing minerals are not highly variable, yet we still observe major differences in spectral contrast and suppression of absorption bands. Clearly, other factors like microtexture must be at play. Carli et al. (2015) recognized the importance of groundmass texture in modifying albedo and band depth independently of composition. In particular, fine-grained groundmass and dark, oxide-bearing glass were suspected of reducing spectral features. Nearly all of our samples exhibit a fine-grained groundmass, but the texture and glass content of the groundmass varies between samples.

EMPA allowed fine-scale examination of the groundmass texture in samples with (e.g., mms-2) and without (e.g., mms-Cb, mns-Vv) clear absorption features (Figure 2.4a-c). These three samples are basaltic andesite with similar TIR spectra (Figure 2.4d), glass content, mineral chemistry, and bulk mineralogy. However, they fall into different VNIR spectral groups due to their overall spectral contrast. mms-2 is in Group 3 and exhibits clear absorptions attributable to

CPX (11 wt.%) and olivine/glass (6/20 wt.%), mms-Cb is in Group 5 and exhibits suppressed but weakly observable absorptions due to CPX (10 wt.%) and olivine/glass (11/28 wt.%), whereas mns-Vv is in Group 6 and exhibits no 1 or 2 μm absorptions despite containing CPX (8 wt.%) and olivine/glass (2/16 wt.%) (Figure 2.4e). All three samples contained small oxide minerals embedded within the glass, but at different crystal sizes. Samples that did not exhibit clear absorption features (mms-Cb and mns-Vv) contained sub-micron-scale oxides, while the sample that did exhibit clear absorption features (mms-2) contained larger micron-scale oxides.

Notably, both mms-Cb and mns-Vv also display a 0.6 μm absorption band absent in mms-2 (Figure 2.4e). Indeed, most spectra in Groups 5 and 6 are dark and exhibit $\sim 0.6 \mu\text{m}$ absorptions that are weak or absent in non-suppressed spectral groups. We hypothesize that sub-micron oxides exsolved in glass (e.g., tachylitic glass) are the primary cause for suppressed VNIR absorptions in these samples. As previously discussed, at sufficiently fine grain sizes, ilmenite becomes selectively absorbing and displays a characteristic 0.6 μm absorption (Tompkins and Pieters, 2010), most strongly in a weakly absorbing matrix such as glass or plagioclase (Pieters and Taylor, 1989; Weitz et al., 1999). It may also mask absorptions depending on the microtexture (Adams et al., 1974). This is somewhat analogous to the suppression of mafic absorptions by fine-grained ferric oxides as observed in our oxidized, red hematite-bearing samples, except in that case the spectrum is entirely overprinted by the characteristic hematite spectrum. Nevertheless, in the most extreme case, ferrous 1 μm absorptions from e.g. olivine and pyroxene can be completely suppressed to leave a smooth continuum as in Group 6.

Due to spot size/resolution limitations, we could not directly assess the chemistry of any sub-micron oxides in glass within our samples. However, larger oxide crystals in the same rocks display ilmenite-hematite compositions (Figure 2.7), and magnetite-ulvospinel oxides are also common in such rock types. Both could be responsible for the overall darkening and slope effects. Different oxides can display other absorptions (e.g., fine-grained magnetite at 0.5 μm ; Izawa et al., 2019) or spectral shapes that are more difficult to distinguish from the continuum slope in this wavelength range. This may explain why a few spectra show suppressed 1 μm spectral features without apparent 0.6 μm bands. We note that this absorption does not correlate with olivine abundance and so is likely not related to the 0.64 μm absorption in olivine (Orofino et al., 2006).

Mafic mineral absorption band suppression in volcanic rocks by submicron oxides may be somewhat analogous to the spectral effects of space weathering. On the lunar surface, nanophase

iron particles dispersed among relatively transparent grains is a key textural characteristic that causes reddened, darkened, and absorption-suppressed spectra characteristic of space weathering on mafic airless bodies (e.g., Chapman, 2004; Pieters et al., 1993). A similar microtextural configuration in our samples, with sub-micron glass-hosted oxides optically “coating” other groundmass grains, could explain the observed darkening and band suppression in our samples.

In the unaltered rocks, this process is not dependent on bulk mineralogy, but rather is a consequence of rock cooling history. As a rock cools, the interstitial liquid solidifies to form some combination of glass and crystalline minerals. Fast cooling provides less opportunity for crystal growth and results in fine-grained, glassy matrix material, but slower cooling allows more and larger crystals (e.g., plagioclase) to grow at the expense of glass. Iron oxides are one such mineral group that can grow from glass at a late stage, resulting in oxides scattered throughout the interstitial glass; for example, magnetite is likely to form in relatively oxidized impact-related glasses on Mars (Cannon et al., 2017). Extrusive, fine-grained, quickly cooled rocks are more likely to form submicroscopic oxide minerals sufficiently fine-grained as to be selectively absorbing and display (in the case of ilmenite) a 0.6 μm absorption, due to higher glass abundances and less opportunity for crystal growth.

Band suppression occurs because minerals that occur as small groundmass crystals alongside glass and oxide minerals are optically “coated” by the oxides to block absorption and reflection. This is less likely to occur when the exsolved oxides are larger and more discrete rather than volumetrically distributed or mantling the mineral in question, when there is less glass, or when the mineral is present as larger phenocrysts or microphenocrysts (e.g., mms-2, Figure 2.4). In our samples, pyroxene occurs primarily as groundmass crystals with very few phenocrysts, whereas olivine occurs almost exclusively as phenocrysts. As a result, pyroxene absorptions are more strongly suppressed by groundmass glass and oxides than olivine in Group 5 spectra despite similar abundances. This behavior is highly dependent on the abundance and distribution of glass and oxides within the sample, as well as the size and distribution of the mineral crystals. In cases where individual crystals, including phenocrysts, are suspended in an abundance of glass and oxides, absorptions from both phenocrysts and groundmass minerals can be fully suppressed (e.g., mns-Vv, Figure 2.4). Based on the mns-Vv sample, at least 2 wt.% of olivine as phenocrysts can be completely suppressed in this scenario, and at least 10 wt.% of pyroxene groundmass. Complete suppression of mafic absorptions alongside a 0.6 μm ilmenite band has also been observed in

ferrobasalts from Craters of the Moon, Idaho, in which fine-grained ilmenite occurs in the glassy groundmass and mantles other microphenocrysts (Haberle, 2018).

In addition to lower overall reflectance and lower spectral contrast, Spectral Groups 5 and 6 also exhibit noticeably concave-up spectral slopes, which we hypothesize may also be related to properties of glass and/or iron oxides in these samples. Concave-up spectra may occur by superimposing a shorter-wavelength blue slope caused by fine grains on the otherwise red-sloped spectra of glass-rich samples (e.g., Group 5). Concave-up spectra can arise from silica-enriched leached rinds on basaltic glass (Chemtob et al., 2010; Minitti et al., 2007), hypothesized to occur through wavelength-dependent scattering off sub-micron scale structures (Horgan et al., 2017; Smith et al., 2017). If so, perhaps glass-hosted oxide phases can cause this scattering characteristic if sufficiently fine-grained, although we note that past studies involving fine-grained ilmenite in lunar glass observed no associated concavity (e.g., Adams et al., 1974; Pieters and Taylor, 1989; Tompkins and Pieters, 2010). Iron oxides such as ilmenite and magnetite also exhibit broad reflectance minima (Izawa et al., 2019) that can exacerbate concavity. VNIR concave-up blue spectral slopes are observed in large areas across the martian surface previously classified as TES Surface Type 2 (e.g., Bandfield et al., 2000; Horgan and Bell, 2012). TIR analysis suggests these surfaces are silica-enriched (Bandfield, 2002; Ruff and Christensen, 2007) and thus more likely related to rinds. However, our results show that VNIR blue slopes and concavity are not unique to silicic rinds and must be interpreted with care, ideally with multiple techniques.

2.7.4 Examples of the Advantages of Combined VNIR and TIR Spectroscopy

Despite the difficulties outlined above, VNIR and TIR are complementary techniques that provide a more comprehensive petrologic picture together than individually. In particular, VNIR provides highly useful information on the distribution and composition of oxide and alteration minerals that can be critical environmental and process indicators, even when they are present at low abundances that would not be captured by the petrologic workhorse that is TIR spectroscopy. For example, TIR spectra of samples awc-2 and awc-3 (Figure 2.10b) provide major mineralogy but no constraints on the oxide mineralogy. Conversely, the VNIR spectrum of awc-3 indicates no mafic mineralogy but is dominated by hematite absorptions. Alone, either spectrum would miss critical petrologic information and lead to misinterpretation in a remote sensing setting, but together they convincingly demonstrate that awc-3 is an oxidized basaltic andesite containing fine-

grained hematite. Similarly, comparing the highly similar TIR spectra of mms-2 and mms-Cb with their markedly different VNIR spectra provides the ability to infer that textural and grain size characteristics are causing differentially suppressed VNIR absorptions (Figure 2).

Used in concert, VNIR and TIR spectra may also be able to accurately predict both pyroxene abundance and composition. Ours is the latest in a series of studies noting difficulties in correctly estimating pyroxene composition in TIR (e.g., Dunn et al., 2007; Hamilton and Christensen, 2000; Hamilton et al., 1997; Wyatt et al., 2001), likely due to insufficient spectral endmembers, so model-based TIR estimates of pyroxene composition in TIR data should be carefully evaluated. However, VNIR may be useful in constraining pyroxene compositions, as relative abundance estimates of OPX and CPX are possible based on 1 and 2 μm band properties (Sunshine and Pieters, 1993).

VNIR and TIR together could also serve as an alternative to XRD on landed missions. XRD is a definitive and quantitative mineralogical technique that has been employed in situ on the martian surface (Blake et al., 2012), and prototypes have been designed for the Moon and other planetary bodies (e.g., Blake et al., 2018). However, XRD on planetary surfaces currently requires a relatively complex drill, sample delivery system, and robotic arm. Although TIR and VNIR spectroscopy have larger errors on bulk mineralogy than XRD, the combination of the two on future rovers or landers would provide both quantitative mineralogy and detection of important environmental indicator minerals that would enable detailed petrologic interpretations of both altered and unaltered rocks. Furthermore, this combination precludes the need for a complex drill or robotic arm and is therefore suitable for missions within low cost categories.

2.7.5 Implications for Planetary Spectroscopy

On Mars, hyperspectral orbital TIR and VNIR data are abundant and generally comparable to laboratory spectra. Much work has been done to characterize the poorly crystalline, high-silica component in Surface Type 2 terrains. In particular, distinguishing between proposed high-silica secondary weathering products such as allophane and aluminosilicate gel (Rampe et al., 2012) and evolved andesite or other material containing primary volcanic glass (e.g., Bandfield et al., 2000) has major implications for crustal evolution and surface weathering. In this work, we have found that total amorphous abundances can be accurately estimated in TIR; however, correct differentiation of primary glass and secondary amorphous silicates is still problematic in laboratory

data, so it is unsurprising that ambiguities exist in the martian data. Both in our study and on Mars, it is likely that we are missing spectral endmembers for some amorphous materials.

We find that TIR does not correctly identify oxide minerals in our samples, where they are not abundant enough to occur above the TIR detection limit. However, accurate modeling of oxide minerals is a greater concern when they are more abundant; for example, martian and lunar surface rocks can contain >10-20 wt.% oxide minerals (e.g., Neal and Taylor, 1992; Rampe et al., 2017). Although bulk oxidation state is not easily derived from VNIR spectra in general, ferric oxides that act as a proxy for oxidation state are detectable, and ferrous oxides such as ilmenite can also be detected under certain circumstances.

We have also found that weak TIR transparency features tend to be modeled by low-Fo# olivine, which may be a more common problem in TIR spectral modeling than previously appreciated. Koeppen and Hamilton (2008) produced global maps of olivine abundance and composition on Mars using TES spectra, and in particular found widespread, spatially incoherent Fo₁₈ in higher abundance than Fo₁ or Fo₃₉. However, they were not able to validate the presence of Fo₁₈ through manual inspection, and concluded these were false detections resulting from noise or atmospheric effects. Our results show that minor transparency effects from fine particulates, which are abundant on the surface of Mars (e.g., Ruff and Christensen, 2002), can also produce erroneous Fe-rich olivine detections.

On the Moon, TIR spectroscopy is limited by lower spectral resolution instruments and thermal gradient effects (Shirley and Glotch, 2019), and VNIR spectroscopy is complicated by spectral changes due to fine grain sizes and space weathering. In VNIR, such spectral effects have been studied extensively in laboratory settings thanks to returned samples and meteorites, allowing for more detailed remote analysis such as quantitative estimates of FeO and TiO₂ content of the surface (Elphic et al., 1998; Lucey et al., 1995). These studies demonstrate that where ground truthing is possible, spectral ambiguities that hamper VNIR spectra can be narrowed down or eliminated. For example, spectra of highlands material known to be anorthositic may have a 1 μ m pyroxene absorption and a 1.3 μ m shoulder that can be assigned to abundant Fe-bearing plagioclase rather than olivine/glass (e.g., Cheek et al., 2013). Without prior knowledge, however, VNIR spectra of igneous rocks exhibiting a shoulder on the long-wavelength side of the 1 μ m pyroxene absorption are prone to ambiguity. For example, VNIR spectra of South Pole-Aitken basin material measured by the Chang'E-4 lander were initially interpreted to contain abundant

olivine indicative of lunar mantle material (Li et al., 2019), but later studies argued that the observed 1 μm asymmetry was more consistent with a pyroxene and feldspar-dominated assemblage involving little to no olivine (Huang et al., 2020). The difference in interpretation resulted from a complex assemblage with multiple non-unique solutions. Additionally, microtextures with the potential to partially mask mafic absorptions have been identified in returned lunar rocks. Microphase ilmenite inclusions have been identified in lunar impact melts (Tompkins and Pieters, 2010), and dark, potentially oxide-bearing glass has been found in lunar breccias and pyroclastic deposits (e.g., Apollo, 1973; Neal and Taylor, 1992; Ryder and Marvin, 1978). More work remains to be done on whether such textures play a significant role in modifying lunar VNIR spectra.

On Venus, spectroscopy of the surface is limited to a handful of near-infrared atmospheric windows between 0.75-1.18 μm , which includes most of the 1 μm mafic absorptions. Measurements of this key wavelength region have been used to infer magmatic evolution, including interpretation of evolved felsic rocks (e.g., Gilmore et al., 2015, 2017; Hashimoto et al., 2008; Mueller et al., 2008). However, the results of this study indicate that the shape and band depth of absorptions in the 1 μm region are not necessarily strongly related to the absolute or relative abundances of common igneous minerals in volcanic rocks, and are not unique indicators of magma evolution. Such spectra may be dominated by microtextural and grain size differences, as well as variable ferric oxides such as those identified by surface landers (Pieters et al., 1986). Due to the paucity of direct mineralogical measurements and the ambiguity inherent in the 1 μm wavelength region of volcanic rocks, future spectroscopic studies of the surface of Venus should consider multiple hypotheses where they exist and avoid over-interpretation.

2.8 Conclusions

This study used a comprehensive combination of IR spectroscopy supported by quantitative XRD, EMPA, and XRF to find that magmatic evolution, crystallinity, and oxidation are largely quantifiable, with caveats, for volcanic rocks using combined VNIR and TIR remote sensing. We have created a new TIR spectral endmember library for use modeling glass-bearing volcanic rocks named ‘volc_env_v5’ that is publicly available in the ASU Spectral Library.

With our new TIR endmember library and sample suite, we reproduce the success of previous studies in determining bulk composition, mineralogy, and rock type (Feely and

Christensen, 1999; Hamilton and Christensen, 2000; Wyatt et al., 2001). New contributions from this study include:

1. Linear deconvolution of TIR emission spectra successfully with our new endmember library estimates the abundance of X-ray amorphous phases in subalkaline volcanic rocks at the same level of error as other major mineral groups. This comes at no detriment to accuracy in estimates of modal mineralogy, bulk wt.% oxides, rock classification, or solid solution chemistry, and highlights the improvements a robust subset of amorphous library endmembers can provide over few or no amorphous endmembers.
2. Appropriate endmembers are essential for accurate estimations of solid solution mineral chemistry, especially for groups that are complicated by crystal symmetry changes, such as alkali feldspars and pyroxenes.
3. Additional high-silica glass endmembers with variable crystallinity are likely still needed to accurately model the composition of volcanic glasses, but with the current library, substitution for these phases by secondary high-silica amorphous phases still accurately estimates wt.% SiO₂ of volcanic glass (taken as the total of all modeled amorphous material), particularly at high glass abundances.
4. TIR spectral deconvolutions of oxidized (hematite-bearing) lava flows and scoria are no less accurate than those of unaltered material. However, the minor oxide minerals do not greatly affect the spectral shape and remain mostly unconstrained in abundance and composition. The mineralogy and chemistry of material that is both glassy and hydrothermally altered is less accurately modeled.
5. Minor amounts of clinging fines introduce a small, known transparency feature near 900 cm⁻¹ that results in the overestimation of Fe-rich olivine. This problem might be relevant to published estimates of olivine abundance and chemistry on Mars.

By applying XRD and EMPA insights to VNIR spectra of our samples, we find that VNIR can be useful for basic mineral identification, but is too susceptible to non-unique band overlap and microtextural effects to be a reliable petrologic tool. Specifically:

1. Glass absorptions in VNIR spectra of natural volcanic samples are sometimes detectable in moderately glass-rich samples, but never uniquely so, even in our most glassy (~55 wt.%)

samples. This is consistent with previous studies that showed that glass is only uniquely detectable in the VNIR at higher abundances.

2. In rocks with pyroxene-dominated spectra, olivine and glass (and sometimes plagioclase feldspar; e.g., Huang et al., 2020) can induce highly similar 1 μm shoulders that can result in non-unique manual or parameter-based interpretations.
3. Sub-micron oxide minerals like ilmenite hosted in volcanic glass can lower albedo, partially to completely suppress mafic absorption bands, and preferentially suppress absorptions of groundmass minerals compared to phenocrysts (Haberle, 2018). This microtextural effect is most common in fine-grained, extrusive rocks due to increased likelihood of abundant glass and small crystals. In a similar fashion, samples containing a few wt.% of fine-grained hematite are spectrally dominated by hematite and exhibit no other identifiable absorptions.
4. VNIR interpretations can be confounded both by degeneracies in multicomponent mixing as well as spectral effects caused by rock microtexture. We have shown that igneous rocks with very different mineralogy can produce highly similar spectra, but also that rocks with similar mineralogy can produce differing spectra due to oxide microphases.
5. Any attempts to perform rock identification and make petrologic interpretations using VNIR spectroscopy alone must acknowledge and understand the scope of these limitations. While sophisticated modeling techniques such as Hapke- or Shkuratov-based unmixing may alleviate mixture degeneracies, they are highly susceptible to both complications from microtexture and weak absorbers like glass, plagioclase, and quartz, and cannot be regarded as perfect models. For manual interpretations, in the extreme case these effects make it difficult to impossible to predict a spectrum based on mineralogy alone (without knowledge of rock fabric), or to predict a complex mineralogy based on a spectrum alone.

Overall, we find that:

1. TIR is a highly useful petrologic tool that can accurately derive glass and major mineral abundances and sometimes chemistry, but is susceptible to inadequate or missing endmember and transparency features.
2. We do not recommend VNIR as a stand-alone technique for remote petrology or rock identification. This conclusion has been demonstrated by previous efforts at VNIR-based petrology that resulted in different interpretations (e.g., Carter and Poulet, 2013; Huang et al.,

2020; Li et al., 2019; Rogers and Nekvasil, 2015; Wray et al., 2013). The results of this study indicate caution is necessary in extending VNIR mineral detections to rock identification. VNIR spectral interpretations are more reliable if they are supported by other methods, landed missions, or returned samples/meteorites.

3. Combined application of VNIR and TIR techniques for remote planetary petrology is advisable because the techniques are highly complementary.

APPENDIX

SUPPLEMENTARY DATA

Figures S1-S11. Accessible through the publicly available Mendeley Data repository: <https://doi.org/10.17632/2vkdbfjptn> (Scudder et al., 2020).

Tables S1-S12. Accessible through the publicly available Mendeley Data repository: <https://doi.org/10.17632/2vkdbfjptn> (Scudder et al., 2020).

The data repository linked above also includes all sample information, raw VNIR and TIR spectra and XRD patterns, TIR and VNIR derived data, XRF and EMPA data, and thin section photomicrographs.

Supplementary data may also be accessed through the Supplementary Data section of the published article, found here: <https://doi.org/10.1016/j.icarus.2021.114344>.

The TIR endmember library used in this work is publicly available as “volc_env_v5” in the ASU Speclib (speclib.asu.edu), as a list in the Supplementary Data section of the published article, and in the linked Mendeley Data repository.

REFERENCES

- Adams, J.B., 1968. Lunar and Martian Surfaces: Petrologic Significance of Absorption Bands in the Near-Infrared. *Science* 159, 1453–1455. <https://doi.org/10.1126/science.159.3822.1453>
- Adams, J.B., Goullaud, L.H., 1978. Plagioclase feldspars-Visible and near infrared diffuse reflectance spectra as applied to remote sensing. *Proc. Lunar Planet. Sci. Conf.* 9th, 2091–2909.
- Adams, J.B., Pieters, C., McCord, T.B., 1974. Orange glass-Evidence for regional deposits of pyroclastic origin on the moon. *Geochimica et Cosmochimica Acta* 1, 171–186.
- Apollo 17 Preliminary Examination Team, 1973. Apollo 17 Lunar Samples: Chemical and Petrographic Description. *Science* 182, 659–672. <https://doi.org/10.1126/science.182.4113.659>
- Bandfield, J.L., 2002. Global mineral distributions on Mars. *J. Geophys. Res. Planets* 1991-2012 107, 5042. <https://doi.org/10.1029/2001je001510>
- Bandfield, J.L., Hamilton, V.E., Christensen, P.R., 2000. A Global View of Martian Surface Compositions from MGS-TES. *Science* 287, 1626–1630. <https://doi.org/10.1126/science.287.5458.1626>
- Basilevsky, A.T., Nikolaeva, O.V., Weitz, C.M., 1992. Geology of the Venera 8 landing site region from Magellan data: Morphological and geochemical considerations. *J. Geophys. Res. Planets* 97, 16315–16335. <https://doi.org/10.1029/92je01557>
- Bell, P.M., Mao, H.K., 1973. Optical and chemical analysis of iron in Luna 20 plagioclase. *Geochim. Cosmochim. Ac.* 37, 755–759. [https://doi.org/10.1016/0016-7037\(73\)90172-5](https://doi.org/10.1016/0016-7037(73)90172-5)
- Bell, P.M., Mao, H.K., Weeks, R.A., 1976. Optical spectra and electron paramagnetic resonance of lunar and synthetic glasses-A study of the effects of controlled atmosphere, composition, and temperature. *Proc. Lunar Sci. Conf.* 7th, 2543–2559.
- Bennett, K.A., Horgan, B.H.N., Gaddis, L.R., Greenhagen, B.T., Allen, C.C., Hayne, P.O., Bell, J.F., Paige, D.A., 2016. Complex explosive volcanic activity on the Moon within Oppenheimer crater. *Icarus* 273, 296–314. <https://doi.org/10.1016/j.icarus.2016.02.007>
- Besse, S., Sunshine, J.M., Gaddis, L.R., 2014. Volcanic glass signatures in spectroscopic survey of newly proposed lunar pyroclastic deposits. *J. Geophys. Res. Planets* 119, 355–372. <https://doi.org/10.1002/2013je004537>
- Bibring, J.-P., Langevin, Y., Gendrin, A., Gondet, B., Poulet, F., Berthé, M., Soufflot, A., Arvidson, R., Mangold, N., Mustard, J., Drossart, P., the OMEGA team, 2005. Mars Surface Diversity as Revealed by the OMEGA/Mars Express Observations. *Science* 307, 1576–1581. <https://doi.org/10.1126/science.1108806>

- Bish, D.L., Howard, S.A., 1988. Quantitative phase analysis using the Rietveld method. *J. Appl. Crystallogr.* 21, 86–91. <https://doi.org/10.1107/s0021889887009415>
- Bish, D.L., Post, J.E., 1993. Quantitative mineralogical analysis using the Rietveld full-pattern fitting method. *American Mineralogist* 78, 932–940.
- Bish, D.L., Reynolds, R.C., 1989. Sample preparation for X-ray diffraction. *Modern powder diffraction* 20, 73–99. <https://doi.org/10.1515/9781501509018>
- Bishop, J.L., Lane, M.D., Dyar, M.D., Brown, A.J., 2008. Reflectance and emission spectroscopy study of four groups of phyllosilicates: smectites, kaolinite-serpentines, chlorites and micas. *Clay Miner.* 43, 35–54. <https://doi.org/10.1180/claymin.2008.043.1.03>
- Blake, D., Sarrazin, P., Bristow, T., 2018. The CheMin X-ray Diffractometer: Results from Mars and Prospects for Next Generation XRD Instruments, in: *European Planetary Science Congress*. pp. EPSC2018-560.
- Blake, D., Vaniman, D., Achilles, C., Anderson, R., Bish, D., Bristow, T., Chen, C., Chipera, S., Crisp, J., Marais, D.D., Downs, R.T., Farmer, J., Feldman, S., Fonda, M., Gailhanou, M., Ma, H., Ming, D.W., Morris, R.V., Sarrazin, P., Stolper, E., Treiman, A., Yen, A., 2012. Characterization and Calibration of the CheMin Mineralogical Instrument on Mars Science Laboratory. *Space Sci. Rev.* 170, 341–399. <https://doi.org/10.1007/s11214-012-9905-1>
- Brown, A.J., 2014. Spectral bluing induced by small particles under the Mie and Rayleigh regimes. *Icarus* 239, 85–95. <https://doi.org/10.1016/j.icarus.2014.05.042>
- Brown, G.M., Peckett, A., Emeleus, C.H., Phillips, R., Pinsent, R.H., 1975. Petrology and mineralogy of Apollo 17 mare basalts. *Proc. Lunar Sci. Conf.* 6th, 1–13.
- Burns, R.G., 1993. Mineralogical Applications of Crystal Field Theory. <https://doi.org/10.1017/cbo9780511524899>
- Byrnes, J.M., Ramsey, M.S., King, P.L., Lee, R.J., 2007. Thermal infrared reflectance and emission spectroscopy of quartzofeldspathic glasses. *Geophys. Res. Lett.* 34, 1626. <https://doi.org/10.1029/2006gl027893>
- Calvert, A.T., Fierstein, J., Hildreth, W., 2018. Eruptive history of Middle Sister, Oregon Cascades, USA—Product of a late Pleistocene eruptive episode. *Geosphere* 14, 1–22. <https://doi.org/10.1130/ges01638.1>
- Cannon, K.M., Mustard, J.F., 2015. Preserved glass-rich impactites on Mars. *Geology* 43, 635–638. <https://doi.org/10.1130/g36953.1>
- Cannon, K.M., Mustard, J.F., Parman, S.W., Sklute, E.C., Dyar, M.D., Cooper, R.F., 2017. Spectral properties of Martian and other planetary glasses and their detection in remotely sensed data. *J. Geophys. Res. Planets* 122, 249–268. <https://doi.org/10.1002/2016je005219>

- Carli, C., Roush, T.L., Pedrazzi, G., Capaccioni, F., 2016. Visible and Near-Infrared (VNIR) reflectance spectroscopy of glassy igneous material: Spectral variation, retrieving optical constants and particle sizes by Hapke model. *Icarus* 266, 267–278. <https://doi.org/10.1016/j.icarus.2015.10.032>
- Carli, C., Serventi, G., Sgavetti, M., 2015. VNIR spectral characteristics of terrestrial igneous effusive rocks: mineralogical composition and the influence of texture. *Geological Soc. Lond. Special Publ.* 401, 139–158. <https://doi.org/10.1144/sp401.19>
- Carli, C., Sgavetti, M., 2011. Spectral characteristics of rocks: Effects of composition and texture and implications for the interpretation of planet surface compositions. *Icarus* 211, 1034–1048. <https://doi.org/10.1016/j.icarus.2010.11.008>
- Carr, M.H., 1973. Volcanism on Mars. *J. Geophys. Res.* 78, 4049–4062. <https://doi.org/10.1029/jb078i020p04049>
- Carter, J., Poulet, F., 2013. Ancient plutonic processes on Mars inferred from the detection of possible anorthositic terrains. *Nature Geoscience* 6, 1008–1012. <https://doi.org/10.1038/ngeo1995>
- Chapman, C.R., 2004. Space weathering of asteroid surfaces. *Ann. Rev. Earth Planet. Sci.* 32, 539–567. <https://doi.org/10.1146/annurev.earth.32.101802.120453>
- Cheek, L.C., Hanna, K.L.D., Pieters, C.M., Head, J.W., Whitten, J.L., 2013. The distribution and purity of anorthosite across the Orientale basin: New perspectives from Moon Mineralogy Mapper data. *J. Geophys. Res. Planets* 118, 1805–1820. <https://doi.org/10.1002/jgre.20126>
- Cheek, L.C., Pieters, C.M., 2014. Reflectance spectroscopy of plagioclase-dominated mineral mixtures: Implications for characterizing lunar anorthosites remotely. *American Mineralogist* 99, 1871–1892. <https://doi.org/10.2138/am-2014-4785>
- Chemtob, S.M., Jolliff, B.L., Rossman, G.R., Eiler, J.M., Arvidson, R.E., 2010. Silica coatings in the Ka'u Desert, Hawaii, a Mars analog terrain: A micromorphological, spectral, chemical, and isotopic study. *J. Geophys. Res.* 115. <https://doi.org/10.1029/2009je003473>
- Christensen, P.R., 2003. Morphology and Composition of the Surface of Mars: Mars Odyssey THEMIS Results. *Science* 300, 2056–2061. <https://doi.org/10.1126/science.1080885>
- Christensen, P.R., Anderson, D.L., Chase, S.C., Clark, R.N., Kieffer, H.H., Malin, M.C., Pearl, J.C., Carpenter, J., Bandiera, N., Brown, F.G., Silverman, S., 1992. Thermal emission spectrometer experiment: Mars Observer mission. *J. Geophys. Res. Planets* 97, 7719–7734. <https://doi.org/10.1029/92je00453>
- Christensen, P.R., Bandfield, J.L., Hamilton, V.E., Howard, D.A., Lane, M.D., Piatek, J.L., Ruff, S.W., Stefanov, W.L., 2000. A thermal emission spectral library of rock-forming minerals. *J. Geophys. Res. Planets* 105, 9735–9739. <https://doi.org/10.1029/1998je000624>

- Christensen, P.R., Harrison, S.T., 1993. Thermal infrared emission spectroscopy of natural surfaces: Application to desert varnish coatings on rocks. *J. Geophys. Res. Solid Earth* 98, 19819–19834. <https://doi.org/10.1029/93jb00135>
- Christensen, P.R., McSween Jr., H.Y., Bandfield, J.L., Ruff, S.W., Rogers, A.D., Hamilton, V.E., Gorelick, N., Wyatt, M.B., Jakosky, B.M., Kieffer, H.H., Malin, M.C., Moersch, J.E., 2005. Evidence for magmatic evolution and diversity on Mars from infrared observations. *Nature* 436, 504–509. <https://doi.org/10.1038/nature03639>
- Christensen, P.R., Morris, R.V., Lane, M.D., Bandfield, J.L., Malin, M.C., 2001. Global mapping of Martian hematite mineral deposits: Remnants of water-driven processes on early Mars. *J. Geophys. Res. Planets* 106, 23873–23885. <https://doi.org/10.1029/2000je001415>
- Christensen, P.R., Wyatt, M.B., Glotch, T.D., Rogers, A.D., Anwar, S., Arvidson, R.E., Bandfield, J.L., Blaney, D.L., Budney, C., Calvin, W.M., Fallacaro, A., Ferguson, R.L., Gorelick, N., Graff, T.G., Hamilton, V.E., Hayes, A.G., Johnson, J.R., Knudson, A.T., McSween, H.Y., Mehall, G.L., Mehall, L.K., Moersch, J.E., Morris, R.V., Smith, M.D., Squyres, S.W., Ruff, S.W., Wolff, M.J., 2004. Mineralogy at Meridiani Planum from the Mini-TES Experiment on the Opportunity Rover. *Science* 306, 1733–1739. <https://doi.org/10.1126/science.1104909>
- Clenet, H., Pinet, P., Ceuleneer, G., Daydou, Y., Heuripeau, F., Rosemberg, C., Bibring, J., Bellucci, G., Altieri, F., Gondet, B., 2013. A systematic mapping procedure based on the Modified Gaussian Model to characterize magmatic units from olivine/pyroxenes mixtures: Application to the Syrtis Major volcanic shield on Mars. *J. Geophys. Res. Planets* 118, 1632–1655. <https://doi.org/10.1002/jgre.20112>
- Clenet, H., Pinet, P., Daydou, Y., Heuripeau, F., Rosemberg, C., Baratoux, D., Chevrel, S., 2011. A new systematic approach using the Modified Gaussian Model: Insight for the characterization of chemical composition of olivines, pyroxenes and olivine–pyroxene mixtures. *Icarus* 213, 404–422. <https://doi.org/10.1016/j.icarus.2011.03.002>
- Cloutis, E.A., 2002. Pyroxene reflectance spectra: Minor absorption bands and effects of elemental substitutions. *J. Geophys. Res. Planets* 1991–2012 107. <https://doi.org/10.1029/2001je001590>
- Cloutis, E.A., Gaffey, M.J., 1991a. Spectral-compositional variations in the constituent minerals of mafic and ultramafic assemblages and remote sensing implications. *Earth Moon Planets* 53, 11–53. <https://doi.org/10.1007/bf00116217>
- Cloutis, E.A., Gaffey, M.J., 1991b. Pyroxene spectroscopy revisited: Spectral-compositional correlations and relationship to geothermometry. *J. Geophys. Res.* 96, 22809–22826. <https://doi.org/10.1029/91je02512>
- Cloutis, E.A., Gaffey, M.J., Smith, D.G.W., Lambert, R.S.J., 1990a. Reflectance spectra of glass-bearing mafic silicate mixtures and spectral deconvolution procedures. *Icarus* 86, 383–401. [https://doi.org/10.1016/0019-1035\(90\)90226-y](https://doi.org/10.1016/0019-1035(90)90226-y)

- Cloutis, E.A., Gaffey, M.J., Smith, D.G.W., Lambert, R.S.J., 1990b. Reflectance spectra of mafic silicate-opaque assemblages with applications to meteorite spectra. *Icarus* 84, 315–333. [https://doi.org/10.1016/0019-1035\(90\)90041-7](https://doi.org/10.1016/0019-1035(90)90041-7)
- Cousin, A., Sautter, V., Payré, V., Forni, O., Mangold, N., Gasnault, O., Deit, L.L., Johnson, J., Maurice, S., Salvatore, M., Wiens, R.C., Gasda, P., Rapin, W., 2017. Classification of igneous rocks analyzed by ChemCam at Gale crater, Mars. *Icarus* 288, 265–283. <https://doi.org/10.1016/j.icarus.2017.01.014>
- Crisp, J., Kahle, A.B., Abbott, E.A., 1990. Thermal infrared spectral character of Hawaiian basaltic glasses. *J. Geophys. Res.* 95, 21657–21669. <https://doi.org/10.1029/jb095ib13p21657>
- Crown, D.A., Pieters, C.M., 1987. Spectral properties of plagioclase and pyroxene mixtures and the interpretation of lunar soil spectra. *Icarus* 72, 492–506. [https://doi.org/10.1016/0019-1035\(87\)90047-9](https://doi.org/10.1016/0019-1035(87)90047-9)
- Czarnecki, S., Hardgrove, C., Gasda, P.J., Gabriel, T.S.J., Starr, M., Rice, M.S., Frydenvang, J., Wiens, R.C., Rapin, W., Nikiforov, S., Lisov, D., Litvak, M., Calef, F., Gengl, H., Newsom, H., Thompson, L., Nowicki, S., 2020. Identification and Description of a Silicic Volcaniclastic Layer in Gale Crater, Mars, Using Active Neutron Interrogation. *J. Geophys. Res. Planets* 125. <https://doi.org/10.1029/2019je006180>
- Dunn, T.L., McSween, H.Y., Christensen, P.R., 2007. Thermal emission spectra of terrestrial alkaline volcanic rocks: Applications to Martian remote sensing. *J. Geophys. Res.* 112, E05001. <https://doi.org/10.1029/2006je002766>
- Dyar, M.D., Burns, R.G., 1982. Coordination chemistry of iron glasses contributing to remote-sensed spectra of the moon, *Proc. Lunar Planet. Sci. Conf.* 12th, 695–702.
- Dyar, M.D., Sklute, E.C., Menzies, O.N., Bland, P.A., Lindsley, D., Glotch, T., Lane, M.D., Schaefer, M.W., Wopenka, B., Klima, R., Bishop, J.L., Hiroi, T., Pieters, C., Sunshine, J., 2009. Spectroscopic characteristics of synthetic olivine: An integrated multi-wavelength and multi-technique approach. *American Mineralogist* 94, 883–898. <https://doi.org/10.2138/am.2009.3115>
- Edgett, K.S., 1997. Aeolian Dunes as Evidence for Explosive Volcanism in the Tharsis Region of Mars. *Icarus* 130, 96–114. <https://doi.org/10.1006/icar.1997.5806>
- Edwards, P.H., Bridges, J.C., Wiens, R., Anderson, R., Dyar, D., Fisk, M., Thompson, L., Gasda, P., Filiberto, J., Schwenzer, S.P., Blaney, D., Hutchinson, I., 2017. Basalt-trachybasalt samples in Gale Crater, Mars. *Meteorit. Planet. Sci.* 159, 1453. <https://doi.org/10.1111/maps.12953>
- Ehlmann, B.L., Edwards, C.S., 2014. Mineralogy of the Martian Surface. *Ann. Rev. Earth Planet. Sci.* 42, 291–315. <https://doi.org/10.1146/annurev-earth-060313-055024>
- Elphic, R.C., Lawrence, D.J., Feldman, W.C., Barraclough, B.L., Maurice, S., Binder, A.B., Lucey, P.G., 1998. Lunar Fe and Ti Abundances: Comparison of Lunar Prospector and Clementine Data. *Science* 281, 1493–1496. <https://doi.org/10.1126/science.281.5382.1493>

- Farmer, V.C., 1974. The Infrared Spectra of Minerals. Mineralogical Society of Great Britain and Ireland. <https://doi.org/10.1180/mono-4>
- Farrand, W.H., Wright, S.P., Rogers, A.D., Glotch, T.D., 2016. Basaltic glass formed from hydrovolcanism and impact processes: Characterization and clues for detection of mode of origin from VNIR through MWIR reflectance and emission spectroscopy. *Icarus* 275, 16–28. <https://doi.org/10.1016/j.icarus.2016.03.027>
- Feely, K.C., Christensen, P.R., 1999. Quantitative compositional analysis using thermal emission spectroscopy: Application to igneous and metamorphic rocks. *J. Geophys. Res.* 104, 24195–24210. <https://doi.org/10.1029/1999je001034>
- Filiberto, J., Gross, J., Trela, J., Ferré, E.C., 2014. Gabbroic Shergottite Northwest Africa 6963: An intrusive sample of Mars. *American Mineralogist* 99, 601–606. <https://doi.org/10.2138/am.2014.4638>
- Fraeman, A.A., Ehlmann, B.L., Arvidson, R.E., Edwards, C.S., Grotzinger, J.P., Milliken, R.E., Quinn, D.P., Rice, M.S., 2016. The stratigraphy and evolution of lower Mount Sharp from spectral, morphological, and thermophysical orbital data sets. *J. Geophys. Res. Planets* 121, 1713–1736. <https://doi.org/10.1002/2016je005095>
- Gaddis, L.R., Pieters, C.M., Hawke, B.R., 1985. Remote sensing of lunar pyroclastic mantling deposits. *Icarus* 61, 461–489. [https://doi.org/10.1016/0019-1035\(85\)90136-8](https://doi.org/10.1016/0019-1035(85)90136-8)
- Gilmore, M., Treiman, A., Helbert, J., Smrekar, S., 2017. Venus Surface Composition Constrained by Observation and Experiment. *Space. Sci. Rev.* 212, 1511–1540. <https://doi.org/10.1007/s11214-017-0370-8>
- Gilmore, M.S., Mueller, N., Helbert, J., 2015. VIRTIS emissivity of Alpha Regio, Venus, with implications for tessera composition. *Icarus* 254, 350–361. <https://doi.org/10.1016/j.icarus.2015.04.008>
- Glotch, T.D., Lucey, P.G., Bandfield, J.L., Greenhagen, B.T., Thomas, I.R., Elphic, R.C., Bowles, N., Wyatt, M.B., Allen, C.C., Hanna, K.D., Paige, D.A., 2010. Highly Silicic Compositions on the Moon. *Science* 329, 1510–1513. <https://doi.org/10.1126/science.1192148>
- Greeley, R., Foing, B.H., McSween, H.Y., Neukum, G., Pinet, P., van Kan, M., Werner, S.C., Williams, D.A., Zegers, T.E., 2005. Fluid lava flows in Gusev crater, Mars. *J. Geophys. Res.* 110, 18. <https://doi.org/10.1029/2005je002401>
- Greeley, R., Spudis, P.D., 1981. Volcanism on Mars. *Rev Geophys* 19, 13–41. <https://doi.org/10.1029/rg019i001p00013>
- Grieve, R.A.F., Cintala, M.J., 1997. Planetary differences in impact melting. *Adv. Space. Res.* 20, 1551–1560. [https://doi.org/10.1016/s0273-1177\(97\)00877-6](https://doi.org/10.1016/s0273-1177(97)00877-6)
- Haberle, C.W., 2018. Integrating Analytical and Remote Sensing Techniques to Investigate the Petrology of Planetary Surfaces [dissertation], Arizona State University.

- Hamilton, V.E., 1999. Particle size effects in particulate rock samples: implications for Thermal Emission Spectrometer (TES) data analysis in high albedo regions on Mars. 5th Intl. Conf. Mars.
- Hamilton, V.E., Christensen, P.R., 2000. Determining the modal mineralogy of mafic and ultramafic igneous rocks using thermal emission spectroscopy. *J. Geophys. Res. Planets* 105, 9717–9733. <https://doi.org/10.1029/1999je001113>
- Hamilton, V.E., Christensen, P.R., McSween Jr., H. Y., 1997. Determination of Martian meteorite lithologies and mineralogies using vibrational spectroscopy. *J. Geophys. Res. Planets* 102, 25593–25603. <https://doi.org/10.1029/97je01874>
- Hapke, B., 1981. Bidirectional reflectance spectroscopy: 1. Theory. *J. Geophys. Res. Solid Earth* 86, 3039–3054. <https://doi.org/10.1029/jb086ib04p03039>
- Hashimoto, G.L., Roos-Serote, M., Sugita, S., Gilmore, M.S., Kamp, L.W., Carlson, R.W., Baines, K.H., 2008. Felsic highland crust on Venus suggested by Galileo Near-Infrared Mapping Spectrometer data. *J. Geophys. Res. Planets* 113. <https://doi.org/10.1029/2008je003134>
- Hauber, E., van Gasselt, S., Ivanov, B., Werner, S., Head, J.W., Neukum, G., Jaumann, R., Greeley, R., Mitchell, K.L., Muller, P., The HRSC Co-Investigator Team, 2005. Discovery of a flank caldera and very young glacial activity at Hecates Tholus, Mars. *Nature* 434, 356. <https://doi.org/10.1038/nature03423>
- Helbert, J., Dyar, D., Walter, I., Wendler, D., Widemann, T., Marcq, E., Guignan, G., Maturilli, A., Varatharajan, I., Ferrari, S., Mueller, N., Kappel, D., D’Amore, M., Boerner, A., Tsang, C., Arnold, G.E., Smrekar, S., Ghail, R., 2019. The Venus Emissivity Mapper - Obtaining Global Mineralogy of Venus from Orbit on the ESA EnVision and NASA VERITAS missions to Venus. LPSC 50, #2046.
- Henderson, M.J.B., Horgan, B.H.N., Rowe, M.C., Wall, K.T., Scudder, N.A., 2020. Determining the Volcanic Eruption Style of Tephra Deposits from Infrared Spectroscopy. *Earth Space Sci.* <https://doi.org/10.1029/2019ea001013>
- Hildreth, W., Fierstein, J., Calvert, A.T., Robinson, J.E., 2012. Geologic Map of Three Sisters Volcanic Cluster, Cascade Range, Oregon. U.S. Geological Survey Scientific Investigations Map 3186.
- Hill, R.J., Tsambourakis, G., Madsen, I.C., 1993. Improved Petrological Modal Analyses from X-ray Powder Diffraction Data by use of the Rietveld Method I. Selected Igneous, Volcanic, and Metamorphic Rocks. *J. Petrol.* 34, 867–900. <https://doi.org/10.1093/petrology/34.5.867>
- Horgan, B., Bell III, J.F., 2012. Widespread weathered glass on the surface of Mars. *Geology* 40, 391–394. <https://doi.org/10.1130/g32755.1>
- Horgan, B.H.N., Cloutis, E.A., Mann, P., Bell III, J.F., 2014. Near-infrared spectra of ferrous mineral mixtures and methods for their identification in planetary surface spectra. *Icarus* 234, 132–154. <https://doi.org/10.1016/j.icarus.2014.02.031>

- Horgan, B.H.N., Smith, R.J., Cloutis, E.A., Mann, P., Christensen, P.R., 2017. Acidic weathering of basalt and basaltic glass: 1. Near-infrared spectra, thermal infrared spectra, and implications for Mars. *J. Geophys. Res. Planets* 122, 172–202. <https://doi.org/10.1002/2016je005111>
- Huang, J., Xiao, Z., Xiao, L., Horgan, B., Hu, X., Lucey, P., Xiao, X., Zhao, S., Qian, Y., Zhang, H., Li, C., Xu, R., He, Z., Yeng, J., Xue, B., He, Q., Zhong, J., Lin, H., Huang, C., Xie, J., 2020. Diverse rock types detected in the lunar South Pole–Aitken Basin by the Chang'E-4 lunar mission. *Geology* 48, 723–727. <https://doi.org/10.1130/g47280.1>
- Hynek, B.M., Phillips, R.J., Arvidson, R.E., 2003. Explosive volcanism in the Tharsis region: Global evidence in the Martian geologic record. *J. Geophys. Res. Planets* 108. <https://doi.org/10.1029/2003je002062>
- Isaacson, P.J., Klima, R.L., Sunshine, J.M., Cheek, L.C., Pieters, C.M., Hiroi, T., Dyar, M.D., Lane, M., Bishop, J., 2014. Visible to near-infrared optical properties of pure synthetic olivine across the olivine solid solution. *American Mineralogist* 99, 467–478. <https://doi.org/10.2138/am.2014.4580>
- Izawa, M.R.M., Cloutis, E.A., Rhind, T., Mertzman, S.A., Applin, D.M., Stromberg, J.M., Sherman, D.M., 2019. Spectral reflectance properties of magnetites: Implications for remote sensing. *Icarus* 319, 525–539. <https://doi.org/10.1016/j.icarus.2018.10.002>
- Jawin, E.R., Besse, S., Gaddis, L.R., Sunshine, J.M., Head, J.W., Mazrouei, S., 2015. Examining spectral variations in localized lunar dark mantle deposits. *J. Geophys. Res. Planets* 120, 1310–1331. <https://doi.org/10.1002/2014je004759>
- Johnson, J.R., Lucey, P.G., Horton, K.A., Winter, E.M., 1998. Infrared Measurements of Pristine and Disturbed Soils 1. Spectral Contrast Differences between Field and Laboratory Data. *Remote. Sens. Environ.* 64, 34–46. [https://doi.org/10.1016/s0034-4257\(97\)00166-1](https://doi.org/10.1016/s0034-4257(97)00166-1)
- Kanner, L.C., Mustard, J.F., Gendrin, A., 2007. Assessing the limits of the Modified Gaussian Model for remote spectroscopic studies of pyroxenes on Mars. *Icarus* 187, 442–456. <https://doi.org/10.1016/j.icarus.2006.10.025>
- Kargel, J.S., Komatsu, G., Baker, V.R., Strom, R.G., 1993. The Volcanology of Venera and VEGA Landing Sites and the Geochemistry of Venus. *Icarus* 103, 253–275. <https://doi.org/10.1006/icar.1993.1069>
- King, T.V.V., Ridley, W.I., 1987. Relation of the spectroscopic reflectance of olivine to mineral chemistry and some remote sensing implications. *J. Geophys. Res. Solid Earth* 92, 11457–11469. <https://doi.org/10.1029/jb092ib11p11457>
- Klima, R.L., Dyar, M.D., Pieters, C.M., 2011a. Near-infrared spectra of clinopyroxenes: Effects of calcium content and crystal structure. *Meteorit. Planet. Sci.* 46, 379–395. <https://doi.org/10.1111/j.1945-5100.2010.01158.x>

- Klima, R.L., Pieters, C.M., Boardman, J.W., Green, R.O., Head, J.W., Isaacson, P.J., Mustard, J.F., Nettles, J.W., Petro, N.E., Staid, M.I., Sunshine, J.M., Taylor, L.A., Tompkins, S., 2011b. New insights into lunar petrology: Distribution and composition of prominent low-Ca pyroxene exposures as observed by the Moon Mineralogy Mapper (M3). *J. Geophys. Res. Planets* 116. <https://doi.org/10.1029/2010je003719>
- Klima, R.L., Pieters, C.M., Dyar, M.D., 2008. Characterization of the 1.2 μm M1 pyroxene band: Extracting cooling history from near-IR spectra of pyroxenes and pyroxene-dominated rocks. *Meteorit. Planet. Sci.* 43, 1591–1604. <https://doi.org/10.1111/j.1945-5100.2008.tb00631.x>
- Klima, R.L., Pieters, C.M., Dyar, M.D., 2007. Spectroscopy of synthetic Mg-Fe pyroxenes I: Spin-allowed and spin-forbidden crystal field bands in the visible and near-infrared. *Meteorit. Planet. Sci.* 42, 235–253. <https://doi.org/10.1111/j.1945-5100.2007.tb00230.x>
- Klug, H.P., Alexander, L.E., 1974. *X-Ray Diffraction Procedures: For Polycrystalline and Amorphous Materials*, 2nd Edition.
- Koeppen, W.C., Hamilton, V.E., 2008. Global distribution, composition, and abundance of olivine on the surface of Mars from thermal infrared data. *J. Geophys. Res. Planets* 113, 57. <https://doi.org/10.1029/2007je002984>
- Koeppen, W.C., Hamilton, V.E., 2005. Discrimination of glass and phyllosilicate minerals in thermal infrared data. *J. Geophys. Res. Planets* 110. <https://doi.org/10.1029/2005je002474>
- Kokaly, R.F., Clark, R.N., Swayze, G.A., Livo, K.E., Hoefen, T.M., Pearson, N.C., Wise, R.A., Benz, W.M., Lowers, H.A., Driscoll, R.L., Klein, A.J., 2017. USGS Spectral Library Version 7, U.S. Geological Survey Data Series 1035.
- Le Bas, M.J., LeMaitre, R.W., Streckeisen, A., Zanettin, B., 1986. A Chemical Classification of Volcanic Rocks Based on the Total Alkali-Silica Diagram. *J. Petrol.* 27, 745–750. <https://doi.org/10.1093/petrology/27.3.745>
- Lee, R.J., King, P.L., Ramsey, M.S., 2010. Spectral analysis of synthetic quartzofeldspathic glasses using laboratory thermal infrared spectroscopy. *J. Geophys. Res. Solid Earth* 115, 166. <https://doi.org/10.1029/2009jb006672>
- Li, C., Liu, D., Liu, B., Ren, X., Liu, J., He, Z., Zuo, W., Zeng, X., Xu, R., Tan, X., Zhang, X., Chen, W., Shu, R., Wen, W., Su, Y., Zhang, H., Ouyang, Z., 2019. Chang'E-4 initial spectroscopic identification of lunar far-side mantle-derived materials. *Nature* 569, 378–382. <https://doi.org/10.1038/s41586-019-1189-0>
- Lindsley, D.H., Andersen, D.J., 1983. A two-pyroxene thermometer. *J. Geophys. Res.* 88, A887. <https://doi.org/10.1029/jb088is02p0a887>
- Liu, Y., Glotch, T.D., Scudler, N.A., Kraner, M.L., Condit, T., Arvidson, R.E., Guinness, E.A., Wolff, M., Smith, M.D., 2016. End-member identification and spectral mixture analysis of CRISM hyperspectral data: A case study on southwest Melas Chasma, Mars. *J. Geophys. Res. Planets* 121, 2004–2036. <https://doi.org/10.1002/2016je005028>

- Lorenz, R.D., 2000. Microtektites on Mars: Volume and Texture of Distal Impact Ejecta Deposits. *Icarus* 144, 353–366. <https://doi.org/10.1006/icar.1999.6303>
- Lucey, P.G., Taylor, G.J., Malaret, E., 1995. Abundance and distribution of iron on the Moon. *Science* 268, 1150–1153. <https://doi.org/10.1126/science.268.5214.1150>
- Mangold, N., Loizeau, D., Poulet, F., Ansan, V., Baratoux, D., LeMouélic, S., Bardintzeff, J.M., Platevoet, B., Toplis, M., Pinet, P., Masson, Ph., Bibring, J.P., Gondet, B., Langevin, Y., Neukum, G., 2010. Mineralogy of recent volcanic plains in the Tharsis region, Mars, and implications for platy-ridged flow composition. *Earth Planet. Sci. Lett.* 294, 440–450. <https://doi.org/10.1016/j.epsl.2009.07.036>
- Mangold, N., Thompson, L.M., Forni, O., Williams, A.J., Fabre, C., Deit, L.L., Wiens, R.C., Williams, R., Anderson, R.B., Blaney, D.L., Calef, F., Cousin, A., Clegg, S.M., Dromart, G., Dietrich, W.E., Edgett, K.S., Fisk, M.R., Gasnault, O., Gellert, R., Grotzinger, J.P., Kah, L., Mouélic, S.L., McLennan, S.M., Maurice, S., Meslin, P. -Y., Newsom, H.E., Palucis, M.C., Rapin, W., Sautter, V., Siebach, K.L., Stack, K., Sumner, D., Yingst, A., 2016. Composition of conglomerates analyzed by the Curiosity rover: Implications for Gale Crater crust and sediment sources. *J. Geophys. Res. Planets* 121, 353–387. <https://doi.org/10.1002/2015je004977>
- Martinot, M., Flahaut, J., Besse, S., Quantin-Nataf, C., Westrenen, W., 2018. Compositional Variations in the Vicinity of the Lunar Crust-Mantle Interface From Moon Mineralogy Mapper Data. *J. Geophys. Res. Planets* 123, 3220–3237. <https://doi.org/10.1029/2018je005744>
- McCubbin, F.M., Boyce, J.W., Novák-Szabó, T., Santos, A.R., Tartèse, R., Muttik, N., Domokos, G., Vazquez, J., Keller, L.P., Moser, D.E., Jerolmack, D.J., Shearer, C.K., Steele, A., Elardo, S.M., Rahman, Z., Anand, M., Delhaye, T., Agee, C.B., 2016. Geologic history of Martian regolith breccia Northwest Africa 7034: Evidence for hydrothermal activity and lithologic diversity in the Martian crust. *J. Geophys. Res. Planets* 121, 2120–2149. <https://doi.org/10.1002/2016je005143>
- McSween, H.Y., Grove, T.L., Lentz, R.C.F., Dann, J.C., Holzheid, A.H., Riciputi, L.R., Ryan, J.G., 2001. Geochemical evidence for magmatic water within Mars from pyroxenes in the Shergotty meteorite. *Nature* 409, 487–490. <https://doi.org/10.1038/35054011>
- McSween, H.Y., Murchie, S.L., Crisp, J.A., Bridges, N.T., Anderson, R.C., Bell, J.F., Britt, D.T., Brückner, J., Dreibus, G., Economou, T., Ghosh, A., Golombek, M.P., Greenwood, J.P., Johnson, J.R., Moore, H.J., Morris, R.V., Parker, T.J., Rieder, R., Singer, R., Wänke, H., 1999. Chemical, multispectral, and textural constraints on the composition and origin of rocks at the Mars Pathfinder landing site. *J. Geophys. Res. Planets* 104, 8679–8715. <https://doi.org/10.1029/98je02551>
- McSween, H.Y., Ruff, S.W., Morris, R.V., Bell, J.F., Herkenhoff, K., Gellert, R., Stockstill, K.R., Tornabene, L.L., Squyres, S.W., Crisp, J.A., Christensen, P.R., McCoy, T.J., Mittlefehldt, D.W., Schmidt, M., 2006. Alkaline volcanic rocks from the Columbia Hills, Gusev crater, Mars. *J. Geophys. Res. Planets* 111, 4829. <https://doi.org/10.1029/2006je002698>

- McSween, H.Y., Taylor, G.J., Wyatt, M.B., 2009. Elemental Composition of the Martian Crust. *Science* 324, 736–739. <https://doi.org/10.1126/science.1165871>
- Michalski, J.R., 2003. Thermal emission spectroscopy of the silica polymorphs and considerations for remote sensing of Mars. *Geophys. Res. Lett.* 30, 31. <https://doi.org/10.1029/2003gl018354>
- Michalski, J.R., Kraft, M.D., Sharp, T.G., Williams, L.B., Christensen, P.R., 2005. Mineralogical constraints on the high-silica martian surface component observed by TES. *Icarus* 174, 161–177. <https://doi.org/10.1016/j.icarus.2004.10.022>
- Mikouchi, T., Koizumi, E., McKay, G., Monkawa, A., Ueda, Y., Chokai, J., Miyamoto, M., 2004. Yamato 980459: Mineralogy and petrology of a new shergottite-related rock from Antarctica. *Antarctic Meteorite Research* 17, 13–34.
- Milam, K.A., McSween Jr., H. Y., Hamilton, V.E., Moersch, J.M., Christensen, P.R., 2004. Accuracy of plagioclase compositions from laboratory and Mars spacecraft thermal emission spectra. *J. Geophys. Res. Planets* 109, 249. <https://doi.org/10.1029/2003je002097>
- Milam, K.A., McSween Jr., H. Y., Moersch, J., Christensen, P.R., 2010. Distribution and variation of plagioclase compositions on Mars. *J. Geophys. Res. Planets* 115, 249. <https://doi.org/10.1029/2009je003495>
- Minitti, M.E., Hamilton, V.E., 2010. A search for basaltic-to-intermediate glasses on Mars: Assessing martian crustal mineralogy. *Icarus* 210, 135–149. <https://doi.org/10.1016/j.icarus.2010.06.028>
- Minitti, M.E., Kah, L.C., Yingst, R.A., Edgett, K.S., Anderson, R.C., Beegle, L.W., Carsten, J.L., Deen, R.G., Goetz, W., Hardgrove, C., Harker, D.E., Herkenhoff, K.E., Hurowitz, J.A., Jandura, L., Kennedy, M.R., Kocurek, G., Krezoski, G.M., Kuhn, S.R., Limonadi, D., Lipkaman, L., Madsen, M.B., Olson, T.S., Robinson, M.L., Rowland, S.K., Rubin, D.M., Seybold, C., Schieber, J., Schmidt, M., Sumner, D.Y., Tompkins, V.V., Beek, J.K.V., Beek, T.V., 2013. MAHLI at the Rocknest sand shadow: Science and science-enabling activities. *J. Geophys. Res. Planets* 118, 2338–2360. <https://doi.org/10.1002/2013je004426>
- Minitti, M.E., Mustard, J.F., Rutherford, M.J., 2002. Effects of glass content and oxidation on the spectra of SNC-like basalts: Applications to Mars remote sensing. *J. Geophys. Res. Planets* 107, 4851. <https://doi.org/10.1029/2001je001518>
- Minitti, M.E., Weitz, C.M., Lane, M.D., Bishop, J.L., 2007. Morphology, chemistry, and spectral properties of Hawaiian rock coatings and implications for Mars. *J. Geophys. Res. Planets* 112, E05015. <https://doi.org/10.1029/2006je002839>
- Moore, D.M., Reynolds, R.C., 1997. *X-Ray Diffraction and the Identification and Analysis of Clay Minerals*, 2nd ed. Oxford University Press.
- Morlok, A., Hamann, C., Martin, D., Weber, I., Joy, K.H., Hiesinger, H., Wogelius, R., Stojic, A., Helbert, J., 2020. Mid-infrared spectroscopy of laser-produced basalt melts for remote sensing application. *Icarus* 335, 113410. <https://doi.org/10.1016/j.icarus.2019.113410>

- Morlok, A., Klemme, S., Weber, I., Stojic, A., Sohn, M., Hiesinger, H., 2017. IR spectroscopy of synthetic glasses with Mercury surface composition: Analogs for remote sensing. *Icarus* 296, 123–138. <https://doi.org/10.1016/j.icarus.2017.05.024>
- Morlok, A., Stojic, A., Weber, I., Hiesinger, H., Zanetti, M., Helbert, J., 2016. Mid-infrared bi-directional reflectance spectroscopy of impact melt glasses and tektites. *Icarus* 278, 162–179. <https://doi.org/10.1016/j.icarus.2016.06.013>
- Morris, R.V., Agresti, D.G., Lauer, H.V., Newcomb, J.A., Shelfer, T.D., Murali, A.V., 1989. Evidence for pigmentary hematite on Mars based on optical, magnetic, and Mossbauer studies of superparamagnetic (nanocrystalline) hematite. *J. Geophys. Res. Solid Earth* 94, 2760–2778. <https://doi.org/10.1029/jb094ib03p02760>
- Morris, R.V., Vaniman, D.T., Blake, D.F., Gellert, R., Chipera, S.J., Rampe, E.B., Ming, D.W., Morrison, S.M., Downs, R.T., Treiman, A.H., Yen, A.S., Grotzinger, J.P., Achilles, C.N., Bristow, T.F., Crisp, J.A., Marais, D.J.D., Farmer, J.D., Fendrich, K.V., Frydenvang, J., Graff, T.G., Morookian, J.-M., Stolper, E.M., Schwenzer, S.P., 2016. Silicic volcanism on Mars evidenced by tridymite in high-SiO₂ sedimentary rock at Gale crater. *P. Natl. Acad. Sci.* 113, 7071–6. <https://doi.org/10.1073/pnas.1607098113>
- Morrison, S.M., Downs, R.T., Blake, D.F., Prabhu, A., Eleish, A., Vaniman, D.T., Ming, D.W., Rampe, E.B., Hazen, R.M., Achilles, C.N., Treiman, A.H., Yen, A.S., Morris, R.V., Bristow, T.F., Chipera, S.J., Sarrazin, P.C., Fendrich, K.V., Morookian, J.M., Farmer, J.D., Marais, D.J.D., Craig, P.I., 2018. Relationships between unit-cell parameters and composition for rock-forming minerals on Earth, Mars, and other extraterrestrial bodies. *American Mineralogist* 103, 848–856. <https://doi.org/10.2138/am-2018-6123>
- Mueller, N., Helbert, J., Hashimoto, G.L., Tsang, C.C.C., Erard, S., Piccioni, G., Drossart, P., 2008. Venus surface thermal emission at 1 μ m in VIRTIS imaging observations: Evidence for variation of crust and mantle differentiation conditions. *J. Geophys. Res. Planets* 113. <https://doi.org/10.1029/2008je003118>
- Mueller, N.T., Smrekar, S., Helbert, J., Stofan, E., Piccioni, G., Drossart, P., 2017. Search for active lava flows with VIRTIS on Venus Express. *J. Geophys. Res. Planets* 122, 1021–1045. <https://doi.org/10.1002/2016je005211>
- Murchie, S., Arvidson, R., Bedini, P., Beisser, K., Bibring, J. -P., Bishop, J., Boldt, J., Cavender, P., Choo, T., Clancy, R.T., Darlington, E.H., Marais, D.D., Espiritu, R., Fort, D., Green, R., Guinness, E., Hayes, J., Hash, C., Heffernan, K., Hemmler, J., Heyler, G., Humm, D., Hutcheson, J., Izenberg, N., Lee, R., Lees, J., Lohr, D., Malaret, E., Martin, T., McGovern, J.A., McGuire, P., Morris, R., Mustard, J., Pelkey, S., Rhodes, E., Robinson, M., Roush, T., Schaefer, E., Seagrave, G., Seelos, F., Silverglate, P., Slavney, S., Smith, M., Shyong, W. -J., Strohbehn, K., Taylor, H., Thompson, P., Tossman, B., Wirzburger, M., Wolff, M., 2007. Compact Reconnaissance Imaging Spectrometer for Mars (CRISM) on Mars Reconnaissance Orbiter (MRO). *J. Geophys. Res. Planets* 112. <https://doi.org/10.1029/2006je002682>
- Mustard, J.F., 2005. Olivine and Pyroxene Diversity in the Crust of Mars. *Science* 307, 1594–1597. <https://doi.org/10.1126/science.1109098>

- Mustard, J.F., Pieters, C.M., Isaacson, P.J., Head, J.W., Besse, S., Clark, R.N., Klima, R.L., Petro, N.E., Staid, M.I., Sunshine, J.M., Runyon, C.J., Tompkins, S., 2011. Compositional diversity and geologic insights of the Aristarchus crater from Moon Mineralogy Mapper data. *J. Geophys. Res. Planets* 1991-2012 116, E00G12. <https://doi.org/10.1029/2010je003726>
- Neal, C.R., Taylor, L.A., 1992. Petrogenesis of mare basalts: A record of lunar volcanism. *Geochim. Cosmochim. Ac.* 56, 2177–2211. [https://doi.org/10.1016/0016-7037\(92\)90184-k](https://doi.org/10.1016/0016-7037(92)90184-k)
- Neukum, G., Jaumann, R., Hoffmann, H., Hauber, E., Head, J.W., Basilevsky, A.T., Ivanov, B.A., Werner, S.C., van Gasselt, S., Murray, J.B., McCord, T., The HRSC Co-Investigator Team, 2004. Recent and episodic volcanic and glacial activity on Mars revealed by the High Resolution Stereo Camera. *Nature* 432, 971–979. <https://doi.org/10.1038/nature03231>
- Nikolaeva, O.V., Ariskin, A.A., 1999. Geochemical constraints on petrogenic processes on Venus. *J. Geophys. Res. Planets* 104, 18889–18897. <https://doi.org/10.1029/1996je000337>
- Nyquist, L.E., Shih, C.Y., 1992. The isotopic record of lunar volcanism. *Geochim. Cosmochim. Ac.* 56, 2213–2234. [https://doi.org/10.1016/0016-7037\(92\)90185-l](https://doi.org/10.1016/0016-7037(92)90185-l)
- Ody, A., Poulet, F., Langevin, Y., Bibring, J. -P., Bellucci, G., Altieri, F., Gondet, B., Vincendon, M., Carter, J., Manaud, N., 2012. Global maps of anhydrous minerals at the surface of Mars from OMEGA/MEx. *J. Geophys. Res. Planets* 117. <https://doi.org/10.1029/2012je004117>
- Orofino, V., Politi, R., Blanco, A., Fonti, S., 2006. Diffuse reflectance of altered olivine grains: Remote sensing detection and implications for Mars studies. *Planet. Space. Sci.* 54, 784–793. <https://doi.org/10.1016/j.pss.2006.04.009>
- Payré, V., Siebach, K.L., Dasgupta, R., Udry, A., Rampe, E.B., Morrison, S.M., 2020. Constraining Ancient Magmatic Evolution on Mars Using Crystal Chemistry of Detrital Igneous Minerals in the Sedimentary Bradbury Group, Gale Crater, Mars. *J. Geophys. Res. Planets* 125. <https://doi.org/10.1029/2020je006467>
- Pieters, C.M., Fischer, E.M., Rode, O., Basu, A., 1993. Optical effects of space weathering: The role of the finest fraction. *J. Geophys. Res. Planets* 98, 20817–20824. <https://doi.org/10.1029/93je02467>
- Pieters, C.M., Head, J.W., Patterson, W., Pratt, S., Garvin, J., Barsukov, V.L., Basilevsky, A.T., Khodakovsky, I.L., Selivanov, A.S., Panfilov, A.S., Gektin, Yu.M., Narayeva, Y.M., 1986. The Color of the Surface of Venus. *Science* 234, 1379–1383. <https://doi.org/10.1126/science.234.4782.1379>
- Pieters, C.M., Taylor, G.J., 1989. Millimeter petrology and kilometer mineralogical exploration of the Moon. *Proc. Lunar Planet. Sci. Conf.* 19th, 115–125.
- Pisello, A., Vetere, F.P., Bisolfati, M., Maturilli, A., Morgavi, D., Pauselli, C., Iezzi, G., Lustrino, M., Perugini, D., 2019. Retrieving magma composition from TIR spectra: implications for terrestrial planets investigations. *Scientific Reports* 9, 15200. <https://doi.org/10.1038/s41598-019-51543-9>

- Pompilio, L., Sgavetti, M., Pedrazzi, G., 2007. Visible and near-infrared reflectance spectroscopy of pyroxene-bearing rocks: New constraints for understanding planetary surface compositions. *J. Geophys. Res. Planets* 112, E01004. <https://doi.org/10.1029/2006je002737>
- Poulet, F., Mangold, N., Platevoet, B., Bardintzeff, J.M., Sautter, V., Mustard, J.F., Bibring, J.P., Pinet, P., Langevin, Y., Gondet, B., Aléon-Toppani, A., 2009. Quantitative compositional analysis of martian mafic regions using the MEx/OMEGA reflectance data: 2. Petrological implications. *Icarus* 201, 84–101. <https://doi.org/10.1016/j.icarus.2008.12.042>
- Rampe, E.B., Kraft, M.D., Sharp, T.G., 2013. Deriving chemical trends from thermal infrared spectra of weathered basalt: Implications for remotely determining chemical trends on Mars. *Icarus* 225, 749–762. <https://doi.org/10.1016/j.icarus.2013.05.005>
- Rampe, E.B., Kraft, M.D., Sharp, T.G., Golden, D.C., Ming, D.W., Christensen, P.R., 2012. Allophane detection on Mars with Thermal Emission Spectrometer data and implications for regional-scale chemical weathering processes. *Geology* 40, 995–998. <https://doi.org/10.1130/g33215.1>
- Rampe, E.B., Ming, D.W., Blake, D.F., Bristow, T.F., Chipera, S.J., Grotzinger, J.P., Morris, R.V., Morrison, S.M., Vaniman, D.T., Yen, A.S., Achilles, C.N., Craig, P.I., Marais, D.J.D., Downs, R.T., Farmer, J.D., Fendrich, K.V., Gellert, R., Hazen, R.M., Kah, L.C., Morookian, J.M., Peretyazhko, T.S., Sarrazin, P., Treiman, A.H., Berger, J.A., Eigenbrode, J., Fairén, A.G., Forni, O., Gupta, S., Hurowitz, J.A., Lanza, N.L., Schmidt, M.E., Siebach, K., Sutter, B., Thompson, L.M., 2017. Mineralogy of an ancient lacustrine mudstone succession from the Murray formation, Gale crater, Mars. *Earth Planet. Sci. Lett.* 471, 172–185. <https://doi.org/10.1016/j.epsl.2017.04.021>
- Ramsey, M.S., Christensen, P.R., 1998. Mineral abundance determination: Quantitative deconvolution of thermal emission spectra. *J. Geophys. Res.* 103, 577–596.
- Rice, M.S., Cloutis, E.A., III, J.F.B., Bish, D.L., Horgan, B.H., Mertzman, S.A., Craig, M.A., Renaut, R.W., Gautason, B., Mountain, B., 2013. Reflectance spectra diversity of silica-rich materials: Sensitivity to environment and implications for detections on Mars. *Icarus* 223, 499–533. <https://doi.org/10.1016/j.icarus.2012.09.021>
- Rietveld, H.M., 1969. A profile refinement method for nuclear and magnetic structures. *J. Appl. Crystallogr.* 2, 65–71. <https://doi.org/10.1107/s0021889869006558>
- Riu, L., Poulet, F., Bibring, J.-P., Gondet, B., 2019. The M3 project: 2 - Global distributions of mafic mineral abundances on Mars. *Icarus* 322, 31–53. <https://doi.org/10.1016/j.icarus.2019.01.002>
- Robbins, S.J., Achille, G.D., Hynek, B.M., 2011. The volcanic history of Mars: High-resolution crater-based studies of the calderas of 20 volcanoes. *Icarus* 211, 1179–1203. <https://doi.org/10.1016/j.icarus.2010.11.012>

- Rogers, A.D., Aharonson, O., 2008. Mineralogical composition of sands in Meridiani Planum determined from Mars Exploration Rover data and comparison to orbital measurements. *J. Geophys. Res. Planets* 113, E06S14. <https://doi.org/10.1029/2007je002995>
- Rogers, A.D., Christensen, P.R., 2007. Surface mineralogy of Martian low-albedo regions from MGS-TES data: Implications for upper crustal evolution and surface alteration. *J. Geophys. Res. Planets* 112, E01003. <https://doi.org/10.1029/2006je002727>
- Rogers, A.D., Nekvasil, H., 2015. Feldspathic rocks on Mars: Compositional constraints from infrared spectroscopy and possible formation mechanisms. *Geophys. Res. Lett.* 42, 2619–2626. <https://doi.org/10.1002/2015gl063501>
- Rowe, M.C., Kent, A.J.R., Nielsen, R.L., 2009. Subduction Influence on Oxygen Fugacity and Trace and Volatile Elements in Basalts Across the Cascade Volcanic Arc. *J. Petrol.* 50, 61–91. <https://doi.org/10.1093/petrology/egn072>
- Ruff, S.W., Christensen, P.R., 2007. Basaltic andesite, altered basalt, and a TES-based search for smectite clay minerals on Mars. *Geophys. Res. Lett.* 34, L10204. <https://doi.org/10.1029/2007gl029602>
- Ruff, S.W., Christensen, P.R., Barbera, P.W., Anderson, D.L., 1997. Quantitative thermal emission spectroscopy of minerals: A laboratory technique for measurement and calibration. *J. Geophys. Res. Solid Earth* 102, 14899–14913. <https://doi.org/10.1029/97jb00593>
- Ruff, S.W., Christensen, P.R., Blaney, D.L., Farrand, W.H., Johnson, J.R., Michalski, J.R., Moersch, J.E., Wright, S.P., Squyres, S.W., 2006. The rocks of Gusev Crater as viewed by the Mini-TES instrument. *J. Geophys. Res. Planets* 111. <https://doi.org/10.1029/2006je002747>
- Ruscitto, D.M., Wallace, P.J., Johnson, E.R., Kent, A.J.R., Bindeman, I.N., 2010. Volatile contents of mafic magmas from cinder cones in the Central Oregon High Cascades: Implications for magma formation and mantle conditions in a hot arc. *Earth Planet. Sci. Lett.* 298, 153–161. <https://doi.org/10.1016/j.epsl.2010.07.037>
- Rutledge, A.M., Horgan, B.H.N., Havig, J.R., Rampe, E.B., Scudder, N.A., Hamilton, T.L., 2018. Silica Dissolution and Precipitation in Glaciated Volcanic Environments, and Implications for Mars. *Geophys. Res. Lett.* 45, 7371–7381. <https://doi.org/10.1029/2018gl078105>
- Ryder, G., Marvin, U.B., 1978. On the origin of Luna 24 basalts and soils. in: *Mare Crisium: The View from Luna 24* 339–355.
- Salisbury, J.W., Wald, A., 1992. The role of volume scattering in reducing spectral contrast of reststrahlen bands in spectra of powdered minerals. *Icarus* 96, 121–128. [https://doi.org/10.1016/0019-1035\(92\)90009-v](https://doi.org/10.1016/0019-1035(92)90009-v)
- Salvatore, M.R., Mustard, J.F., Head III, J.W., Rogers, A.D., Cooper, R.F., 2014. The dominance of cold and dry alteration processes on recent Mars, as revealed through pan-spectral orbital analyses. *Earth Planet. Sci. Lett.* 404, 261–272. <https://doi.org/10.1016/j.epsl.2014.08.006>

- Sautter, V., Toplis, M.J., Beck, P., Mangold, N., Wiens, R., Pinet, P., Cousin, A., Maurice, S., LeDeit, L., Hewins, R., Gasnault, O., Quantin, C., Forni, O., Newsom, H., Meslin, P.-Y., Wray, J., Bridges, N., Payré, V., Rapin, W., Mouélic, S.L., 2016. Magmatic complexity on early Mars as seen through a combination of orbital, in-situ and meteorite data. *Lithos* 254–255, 36–52. <https://doi.org/10.1016/j.lithos.2016.02.023>
- Schmidt, M.E., Grunder, A.L., 2011. Deep Mafic Roots to Arc Volcanoes: Mafic Recharge and Differentiation of Basaltic Andesite at North Sister Volcano, Oregon Cascades. *J. Petrol.* 52, 603–641. <https://doi.org/10.1093/petrology/egq094>
- Schmidt, M.E., Grunder, A.L., 2009. The evolution of North Sister: A volcano shaped by extension and ice in the central Oregon Cascade Arc. *GSA Bulletin* 121, 643–662. <https://doi.org/10.1130/b26442.1>
- Scudder, N., Horgan, B., Rampe, E., Smith, R., Rutledge, A., (2020), “Data for: The effects of magmatic evolution, crystallinity, and microtexture on the visible/near-infrared and thermal-infrared spectra of volcanic rocks”, Mendeley Data, V1. <https://doi.org/10.17632/2vkdbfjptn>
- Seelos, K.D., Seelos, F.P., Viviano-Beck, C.E., Murchie, S.L., Arvidson, R.E., Ehlmann, B.L., Fraeman, A.A., 2014. Mineralogy of the MSL Curiosity landing site in Gale crater as observed by MRO/CRISM. *Geophys. Res. Lett.* 41, 4880–4887. <https://doi.org/10.1002/2014gl060310>
- Serventi, G., Carli, C., Sgavetti, M., 2016. Deconvolution of mixtures with high plagioclase content for the remote interpretation of lunar plagioclase-rich regions. *Icarus* 272, 1–15. <https://doi.org/10.1016/j.icarus.2016.01.020>
- Serventi, G., Carli, C., Sgavetti, M., Ciarniello, M., Capaccioni, F., Pedrazzi, G., 2013. Spectral variability of plagioclase–mafic mixtures (1): Effects of chemistry and modal abundance in reflectance spectra of rocks and mineral mixtures. *Icarus* 226, 282–298. <https://doi.org/10.1016/j.icarus.2013.05.041>
- Shellnutt, J.G., 2019. The curious case of the rock at Venera 8. *Icarus* 321, 50–61. <https://doi.org/10.1016/j.icarus.2018.11.001>
- Shirley, K.A., Glotch, T.D., 2019. Particle Size Effects on Mid-Infrared Spectra of Lunar Analog Minerals in a Simulated Lunar Environment. *J. Geophys. Res. Planets* 124, 970–988. <https://doi.org/10.1029/2018je005533>
- Shkuratov, Y., Starukhina, L., Hoffmann, H., Arnold, G., 1999. A Model of Spectral Albedo of Particulate Surfaces: Implications for Optical Properties of the Moon. *Icarus* 137, 235–246. <https://doi.org/10.1006/icar.1998.6035>
- Singer, R.B., 1981. Near-infrared spectral reflectance of mineral mixtures: Systematic combinations of pyroxenes, olivine, and iron oxides. *J. Geophys. Res.* 86, 7967–7982.
- Sklute, E.C., Glotch, T.D., Piatek, J.L., Woerner, W.R., Martone, A.A., Kraner, M.L., 2015. Optical constants of synthetic potassium, sodium, and hydronium jarosite. *American Mineralogist* 100, 1110–1122. <https://doi.org/10.2138/am-2015-4824>

- Smith, R.J., Horgan, B.H.N., Mann, P., Cloutis, E.A., Christensen, P.R., 2017. Acid weathering of basalt and basaltic glass: 2. Effects of microscopic alteration textures on spectral properties. *J. Geophys. Res. Planets* 122, 203–227. <https://doi.org/10.1002/2016je005112>
- Smith, R.J., Rampe, E.B., Horgan, B.H.N., Dehouck, E., 2018. Deriving Amorphous Component Abundance and Composition of Rocks and Sediments on Earth and Mars. *J. Geophys. Res. Planets* 122, 2344. <https://doi.org/10.1029/2018je005612>
- Soare, R.J., Horgan, B., Conway, S.J., Souness, C., El-Maarry, M.R., 2015. Volcanic terrain and the possible periglacial formation of “excess ice” at the mid-latitudes of Utopia Planitia, Mars. *Earth Planet. Sci. Lett.* 423, 182–192. <https://doi.org/10.1016/j.epsl.2015.04.033>
- Squyres, S.W., Arvidson, R.E., Blaney, D.L., Clark, B.C., Crumpler, L., Farrand, W.H., Gorevan, S., Herkenhoff, K.E., Hurowitz, J., Kusack, A., McSween, H.Y., Ming, D.W., Morris, R.V., Ruff, S.W., Wang, A., Yen, A., 2006. Rocks of the Columbia Hills. *J. Geophys. Res. Planets* 111. <https://doi.org/10.1029/2005je002562>
- Straub, D.W., Burns, R.G., Pratt, S.F., 1991. Spectral signature of oxidized pyroxenes: implications to remote sensing of terrestrial planets. *J. Geophys. Res. Planets* 96, 18819–18830. <https://doi.org/10.1029/91je01893>
- Sunshine, J.M., Pieters, C.M., 1998. Determining the composition of olivine from reflectance spectroscopy. *J. Geophys. Res. Planets* 103, 13675–13688. <https://doi.org/10.1029/98je01217>
- Sunshine, J.M., Pieters, C.M., 1993. Estimating modal abundances from the spectra of natural and laboratory pyroxene mixtures using the modified Gaussian model. *J. Geophys. Res. Planets* 98, 9075–9087. <https://doi.org/10.1029/93je00677>
- Sunshine, J.M., Pieters, C.M., Pratt, S.F., 1990. Deconvolution of mineral absorption bands: An improved approach. *J. Geophys. Res. Solid Earth* 95, 6955–6966. <https://doi.org/10.1029/jb095ib05p06955>
- Surkov, Yu.A., Moskalyeva, L.P., Shcheglov, O.P., Kharyukova, V.P., Manvelyan, O.S., Kirichenko, V.S., Dudin, A.D., 1983. Determination of the elemental composition of rocks on Venus by Venera 13 and Venera 14 (preliminary results). *J. Geophys. Res. Solid Earth* 88, A481–A493. <https://doi.org/10.1029/jb088is02p0a481>
- Swayze, G.A., Milliken, R.E., Clark, R.N., Bishop, J.L., 2007. Spectral evidence for hydrated volcanic and/or impact glass on Mars with MRO CRISM. 7th Intl. Conf. Mars, #3384.
- Taylor, G.J., Boynton, W., Brückner, J., Wänke, H., Dreibus, G., Kerry, K., Keller, J., Reedy, R., Evans, L., Starr, R., Squyres, S., Karunatillake, S., Gasnault, O., Maurice, S., d’Uston, C., Englert, P., Dohm, J., Baker, V., Hamara, D., Janes, D., Sprague, A., Kim, K., Drake, D., 2006. Bulk composition and early differentiation of Mars. *J. Geophys. Res. Planets* 111. <https://doi.org/10.1029/2005je002645>
- Thomson, J.L., Salisbury, J.W., 1993. The mid-infrared reflectance of mineral mixtures (7–14 μm). *Remote. Sens. Environ.* 45, 1–13. [https://doi.org/10.1016/0034-4257\(93\)90077-b](https://doi.org/10.1016/0034-4257(93)90077-b)

- Tompkins, S., Pieters, C.M., 2010. Spectral characteristics of lunar impact melts and inferred mineralogy. *Meteorit. Planet. Sci.* 45, 1152–1169. <https://doi.org/10.1111/j.1945-5100.2010.01074.x>
- Udry, A., Gazel, E., McSween Jr., H. Y., 2018. Formation of Evolved Rocks at Gale Crater by Crystal Fractionation and Implications for Mars Crustal Composition. *J. Geophys. Res. Planets* 339. <https://doi.org/10.1029/2018je005602>
- Viviano, C.E., Murchie, S.L., Daubar, I.J., Morgan, M.F., Seelos, F.P., Plescia, J.B., 2019. Composition of Amazonian volcanic materials in Tharsis and Elysium, Mars, from MRO/CRISM reflectance spectra. *Icarus* 328, 274–286. <https://doi.org/10.1016/j.icarus.2019.03.001>
- Wall, K.T., Rowe, M.C., Ellis, B.S., Schmidt, M.E., Eccles, J.D., 2014. Determining volcanic eruption styles on Earth and Mars from crystallinity measurements. *Nat. Commun.* 5, 5090. <https://doi.org/10.1038/ncomms6090>
- Walter, L.S., Salisbury, J.W., 1989. Spectral characterization of igneous rocks in the 8- to 12- μ m region. *J. Geophys. Res. Solid Earth* 94, 9203–9213. <https://doi.org/10.1029/jb094ib07p09203>
- Weitz, C.M., Head, J.W., Pieters, C.M., 1998. Lunar regional dark mantle deposits: Geologic, multispectral, and modeling studies. *J. Geophys. Res. Planets* 103, 22725–22759. <https://doi.org/10.1029/98je02027>
- Weitz, C.M., Rutherford, M.J., Head III, J.W., McKay, D.S., 1999. Ascent and eruption of a lunar high-titanium magma as inferred from the petrology of the 74001/2 drill core. *Meteorit. Planet. Sci.* 34, 527–540. <https://doi.org/10.1111/j.1945-5100.1999.tb01361.x>
- Wilson, L., Head, J.W., 2007. Explosive volcanic eruptions on Mars: Tephra and accretionary lapilli formation, dispersal and recognition in the geologic record. *J. Volcanol. Geoth. Res.* 163, 83–97. <https://doi.org/10.1016/j.jvolgeores.2007.03.007>
- Wilson, L., Head, J.W., 1994. Mars: Review and analysis of volcanic eruption theory and relationships to observed landforms. *Rev. Geophys.* 32, 221–263. <https://doi.org/10.1029/94rg01113>
- Wray, J.J., Hansen, S.T., Dufek, J., Swayze, G.A., Murchie, S.L., Seelos, F.P., Skok, J.R., Irwin III, R.P., Ghiorso, M.S., 2013. Prolonged magmatic activity on Mars inferred from the detection of felsic rocks. *Nat. Geosci.* 6, 1013–1017. <https://doi.org/10.1038/ngeo1994>
- Wyatt, M.B., Hamilton, V.E., McSween Jr., H. Y., Christensen, P.R., Taylor, L.A., 2001. Analysis of terrestrial and Martian volcanic compositions using thermal emission spectroscopy: 1. Determination of mineralogy, chemistry, and classification strategies. *J. Geophys. Res. Planets* 106, 14711–14732. <https://doi.org/10.1029/2000je001356>
- Wyatt, M.B., McSween, H.Y., 2002. Spectral evidence for weathered basalt as an alternative to andesite in the northern lowlands of Mars. *Nature* 417, 263–266. <https://doi.org/10.1038/417263a>

PUBLICATION

Scudder, N. A., Horgan, B. H. N., Rampe, E. B., Smith, R. J., & Rutledge, A. M. (2021). The effects of magmatic evolution, crystallinity, and microtexture on the visible/near-infrared and thermal-infrared spectra of volcanic rocks. *Icarus*, 359, 114344. (<https://doi.org/10.1016/j.icarus.2021.114344>)